The Astrophysical Journal, 956:148 (36pp), 2023 October 20 https://doi.org/10.3847/1538-4357/accea2

FAST-ASKAP Synergy: Quantifying Coexistent Tidal and Ram Pressure Strippings in the NGC 4636 Group

Xuchen Lin (林旭辰)[1], Jing Wang (王菁)[2], Virginia Kilborn[3,4], Eric W. Peng[2], Luca Cortese[4,5], Alessandro Boselli[6], Ze-Zhong Liang (梁泽众)[1], Bumhyun Lee[7], Dong Yang (杨冬)[1], Barbara Catinella[4,5], N. Deg[8], H. Dénes[9], Ahmed Elagali[10,11], P. Kamphuis[12], B. S. Koribalski[13,14], K. Lee-Waddell[5,15,16], Jonghwan Rhee[4,5], Li Shao (邵立)[17], Kristine Spekkens[18], Lister Staveley-Smith[5], T. Westmeier[5], O. Ivy Wong[4,5,15], Kenji Bekki[5], Albert Bosma[6], Min Du (杜敏)[19], Luis C. Ho[2], Juan P. Madrid[20], Lourdes Verdes-Montenegro[21], Huiyuan Wang (王慧元)[22,23], and Shun Wang (王舜)[1]

[1] Department of Astronomy, School of Physics, Peking University, Beijing 100871, People's Republic of China
[2] Kavli Institute for Astronomy and Astrophysics, Peking University, Beijing 100871, People's Republic of China; jwang_astro@pku.edu.cn
[3] Centre for Astrophysics and Supercomputing, Swinburne University of Technology, P.O. Box 218, Hawthorn, VIC 3122, Australia
[4] ARC Centre of Excellence for All-Sky Astrophysics in 3 Dimensions (ASTRO 3D), Australia
[5] International Centre for Radio Astronomy Research (ICRAR), The University of Western Australia, 35 Stirling Highway, Crawley, WA 6009, Australia
[6] Aix Marseille University, CNRS, CNES, LAM, Marseille, France
[7] Korea Astronomy and Space Science Institute, 776 Daedeokdae-ro, Daejeon 34055, Republic of Korea
[8] Department of Physics, Engineering Physics, and Astronomy, Queen's University, Kingston, ON, K7L 3N6, Canada
[9] School of Physical Sciences and Nanotechnology, Yachay Tech University, Hacienda San José S/N, 100119, Urcuquí, Ecuador
[10] Minderoo Foundation, 171–173 Mounts Bay Road, Perth, WA 6000, Australia
[11] School of Biological Sciences, The University of Western Australia, 35 Stirling Highway, Crawley, WA 6009, Australia
[12] Ruhr University Bochum, Faculty of Physics and Astronomy, Astronomical Institute, D-44780 Bochum, Germany
[13] CSIRO Astronomy and Space Science, Australia Telescope National Facility, P.O. Box 76, NSW 1710, Australia
[14] School of Science, Western Sydney University, Locked Bag 1797, Penrith, NSW 2751, Australia
[15] CSIRO Space and Astronomy, P.O. Box 1130, Bentley, WA 6102, Australia
[16] International Centre for Radio Astronomy Research (ICRAR), Curtin University, GPO Box U1987, Perth, WA 6845, Australia
[17] National Astronomical Observatories, Chinese Academy of Sciences, 20A Datun Road, Chaoyang District, Beijing 100012, People's Republic of China
[18] Department of Physics and Space Science, Royal Military College of Canada, P.O. Box 17000, Station Forces, Kingston, Ontario, K7K 7B4, Canada
[19] Department of Astronomy, Xiamen University, Xiamen, Fujian 361005, People's Republic of China
[20] Department of Physics and Astronomy, The University of Texas Rio Grande Valley, Brownsville, TX 78520, USA
[21] Instituto de Astrofísica de Andalucía (CSIC), Glorieta de la Astronomía, E-18008, Granada, Spain
[22] Key Laboratory for Research in Galaxies and Cosmology, Department of Astronomy, University of Science and Technology of China, Hefei, Anhui 230026, People's Republic of China
[23] School of Astronomy and Space Science, University of Science and Technology of China, Hefei, Anhui 230026, People's Republic of China
Received 2023 January 16; revised 2023 March 30; accepted 2023 April 18; published 2023 October 19

Abstract

Combining new H I data from a synergetic survey of Australian Square Kilometre Array Pathfinder (ASKAP) Widefield ASKAP *L*-band Legacy All-sky Blind surveY and Five-hundred-meter Aperture Spherical radio Telescope with the Arecibo Legacy Fast ALFA data, we study the effect of ram pressure and tidal interactions in the NGC 4636 group. We develop two parameters to quantify and disentangle these two effects on gas stripping in H I-bearing galaxies: the strength of external forces at the optical-disk edge, and the outside-in extents of H I-disk stripping. We find that gas stripping is widespread in this group, affecting 80% of H I-detected nonmerging galaxies, and that 41% are experiencing both types of stripping. Among the galaxies experiencing both effects, the two types of strengths are independent, while two H I-stripping extents moderately anticorrelate with each other. Both strengths are correlated with H I-disk shrinkage. The tidal strength is related to a rather uniform reddening of low-mass galaxies ($M_* < 10^9\,M_\odot$) when tidal stripping is the dominating effect. In contrast, ram pressure is not clearly linked to the color-changing patterns of galaxies in the group. Combining these two stripping extents, we estimate the total stripping extent, and put forward an empirical model that can describe the decrease of H I richness as galaxies fall toward the group center. The stripping timescale we derived decreases with distance to the center, from ∼1 Gyr beyond R_{200} to $\lesssim$10 Myr near the center. Gas depletion happens ∼3 Gyr since crossing $2R_{200}$ for H I-rich galaxies, but much quicker for H I-poor ones. Our results quantify in a physically motivated way the details and processes of environmental-effects-driven galaxy evolution, and might assist in analyzing hydrodynamic simulations in an observational way.

Unified Astronomy Thesaurus concepts: Galaxies (573); Interstellar atomic gas (833); Galaxy evolution (594); Galaxy environments (2029)

Supporting material: machine-readable tables

1. Introduction

It is well established that environmental effects are an essential part of galaxy evolution (e.g., Gunn & Gott 1972; Dressler 1980; Whitmore et al. 1993; Abadi et al. 1999; Poggianti et al. 1999; Blanton & Moustakas 2009). They play a dominating role in

driving the evolution of low-mass satellite galaxies in general (Boselli & Gavazzi 2014), while they also vigorously transform high-mass galaxies under proper conditions (Chung et al. 2009). Because environmental effects work through several different physical mechanisms and each of them depends on a number of parameters (Boselli & Gavazzi 2006), it has been challenging to disentangle how they exactly work on galaxies in addition to stellar-mass-related galactic internal effects (Cortese et al. 2021).

The primary physical processes producing the environmental effects have been largely identified. They can be divided into gravitational and hydrodynamic types, with tidal interaction[24] and ram pressure stripping (RPS) being probably the most prevalent mechanism in each type (Boselli & Gavazzi 2006). With the aid of analytical models and results from controlled simulations that are designed to isolate a given mechanism, it is possible to identify unique conditions or features to select representative samples or prototypes in the real universe that are experiencing strong tidal forces (e.g., Pan et al. 2019; Thorp et al. 2019) or ram pressure (e.g., Poggianti et al. 2017; Moretti et al. 2022), but details are still uncertain due to the lack of constraints from observation (e.g., Font et al. 2008; Henriques et al. 2015). In targeted observations conducted with a similar idea, the H I gas has been a popular tracer for environmental effects, because when it is abundant it is easily perturbed by those effects (Chung et al. 2009), while when it is poor it signals the beginning of star formation quenching (Boselli et al. 2016). These previous studies found that the H I masses quickly decrease (within tens to hundreds of megayears) once the galaxies reach the "stripping zone" of ram pressure and show one-sided tails (Jaffé et al. 2015; Yoon et al. 2017), while the effect of tidal interactions may be more complex and can be conflicting (Ellison et al. 2018; Yu et al. 2022), but doubts remain whether these galaxies are representative enough.

The targeted studies enable us to explore the parameter space of each physical mechanism, but they are just the first step toward understanding the effects and roles of each mechanism in galaxy evolution in a cosmological context. The cosmological context sets the actual occupation distribution of local galaxies in the parameter space. More specifically, it determines the typical properties of galaxies when they fell into their current cluster, as well as the dynamic condition of the clusters when these galaxies travel through them. In this context, preprocessing can start far before satellites reach their current cluster (Haines et al. 2015; Murugeshan et al. 2021), and less-massive satellites tend to be satellites for a longer time (De Lucia et al. 2012). More-massive satellites deplete the H I and quench faster both since they enter the first cluster and since they enter the current cluster, because they are closer to being depleted or quiescent before becoming satellites (Jung et al. 2018; Oman et al. 2021). The cold dark matter (CDM) hierarchical assembly paradigm also produces substructures in clusters, which provide unique local environmental conditions like enhanced galaxy number densities and shocked intracluster medium (ICM; Ruggiero et al. 2019).

Despite the above, it is challenging to pinpoint the effect of each physical mechanism when we look into the general population of satellite galaxies. Indeed, the effects of different environmental processes often mix in less-prototypical galaxies (Marasco et al. 2016). Determined by their physical nature, tidal interaction and ram pressure tend to both strengthen in higher-density environments and when they act on low-mass galaxies (Boselli & Gavazzi 2006). In addition to statistical arguments (Marasco et al. 2016), there are observational examples where the two effects coexist in the same galaxy, and resolved H I images often provide the crucial supporting evidence (Vollmer 2003; Chung et al. 2007). Tidal interaction and ram pressure also interplay with each other. For example, tidal interactions can assist RPS by distributing gas to the outer stellar disk where the restoring force is weaker (McPartland et al. 2016), while ram pressure may prevent tidal stripping (TS) on the leading side of the motion of galaxies (Boselli et al. 2018). To make things more complex, the galactic internal effects, including the stellar feedback, can interfere with the two environmental processes, by pushing the gas to a location or kinematic status more prone to stripping (Kazantzidis et al. 2017; Boselli et al. 2022).

Possibly because of these difficulties, the role of the environment is much less established in groups compared to massive clusters: groups have less extreme environments and thus more complex combinations of environmental mechanisms. Although based on detailed analysis of high-resolution images of the neutral or ionized gas, individual satellite galaxies undergoing RPS or TS have been identified in the group environment (e.g., Vulcani et al. 2018b), statistically establishing the importance of these effects is still difficult. Most observational statistical studies tend to go around these complexities, use general parameters such as local densities to describe the environment, and focus on the consequence of the different effects combined together (Brown et al. 2017; Smethurst et al. 2017; Cortese et al. 2021). Motivated by the observed relatively long quenching time for star formation in satellite galaxies, it has been suggested that starvation following RPS of the hot-gas halo, as opposed to RPS of the neutral gas, is the primary mechanism for quenching in groups (e.g., Haines et al. 2015; Smethurst et al. 2017). Similar conclusions have been reached by cosmological semianalytical simulations (Font et al. 2008; Xie et al. 2020). On the other hand, many simulations also suggest that RPS of the cold gas might be necessary to reproduce the observed distribution of H I deficiency for satellites (Xie et al. 2020), particularly those in massive groups (Ayromlou et al. 2021). In cosmological simulations, the tidal interaction on gas is less discussed, which can be more complex than RPS as it can induce both the removal and accretion of gas as suggested by recent zoomed-in hydrodynamic simulations (Sparre et al. 2022). Recent theoretical studies have more clearly pointed out the degeneracy between the internal feedback and environmental effects in cosmological semianalytical models (Stevens & Brown2017) and the lasting discrepancy between the theoretical prediction and observation of H I gas in cosmological hydrodynamic simulations of group environmental effects (Stevens et al. 2019).

It is now the time when we need to disentangle the effects of different environmental processes, in order to move forward on the topic of environment-driven galaxy evolution. To solve the same problem from the theoretical side with cosmological simulations, a standard approach is to implement analytical recipes or prescriptions directly deduced from physical models or empirically summarized from controlled simulations (e.g., Di Matteo et al. 2007) to track the effects of different environmental mechanisms (Somerville & Davé 2015). These

[24] In this paper, we mainly refer to the satellite–satellite interactions, but we do not specifically distinguish between harassment, low-speed interaction, and merger.

recipes typically depict the contrast between restoring and perturbing forces on the interstellar medium. A similar approach can be applied to the observational data that deeply detect and spatially resolve the distribution of gas in galaxies for the whole clusters. Contiguous large maps that cover the infalling and virialized regions of clusters provide both a relatively cosmologically representative view (in contrast to targeted, small-field observations) and a large number of galaxies. The latter could assist in statistically reducing the observational uncertainties (of relative distance, velocity, density, etc.) due to projections. Subgalactic spatial resolution is necessary to derive the localized forces, while high sensitivity is essential for tracing the late stage of environmental processing.

The aforementioned approach of using analytical prescriptions to separate environmental effects has been tested with data from the prepilot and pilot surveys of Widefield ASKAP *L*-band Legacy All-sky Blind surveY (WALLABY; Westmeier et al. 2022), which has a field of view of 30 $\deg^2$ per pointing. As a conservative preparation, these experiments dealt with prototypical clusters and/or groups where either the tidal or ram pressure effects tend to dominate. Based on the empirical model of Elmegreen et al. (1991), Wang et al. (2022) derived the tidal strength parameter $S_{\rm tid}$ to quantify the instantaneous effect of tidal interaction on the optical disk. They showed that $S_{\rm tid}$ reasonably traced the tidally driven effects of H I-disk shrinking and optical-disk reddening for dwarf galaxies in the Eridanus supergroup. Based on a revised form of the analytical model from Gunn & Gott (1972), Wang et al. (2021) derived the amount of strippable H I due to RPS, $f_{\rm RPS}$. With $f_{\rm RPS}$, they were able to characterize the diversity of RPS effects on reducing the galactic H I mass in the Hydra cluster. The next step is to combine these two prescriptions for galaxies in less-prototypical clusters and/or groups, and to test how far one may reach in disentangling the RPS or TS effects of H I-removal.

In this work, we analyze the evolution of galaxies under the RPS and TS effects in the NGC 4636 group (N4636G). The paper is organized as follows. The main information of the group is described in Section 2 and basic statistical properties of members are reported in Section 4. The H I data, which are described in more detail in Sections 2 and 3 together with the multiwavelength data, come from a Five-hundred-meter Aperture Spherical radio Telescope (FAST) and WALLABY synergetic observational program. We are therefore able to reach a low H I-mass limit, and to spatially resolve the large H I disks and deblend close pairs at the same time. In Section 5, based on results and experience from the previous studies (Wang et al. 2021, 2022), we develop a new parameter $f_{\rm tid}$ to quantify the amount of H I strippable due to TS, and another new parameter $S_{\rm RPS}$ to quantify the instantaneous effect of RPS on the H I disk at the edge of stellar disk. In Section 6, we study how galaxy properties vary in response to changes in these parameters ($f_{\rm tid}$, $f_{\rm RPS}$, $S_{\rm tid}$, and $S_{\rm RPS}$). In Section 7, we put these results together and use a highly simplified model to describe the H I stripping history of galaxies when they fall into N4636G. We derive the H I stripping timescales, and predict the H I depleting timescales based on this model. The results are not very different from those previously obtained from hydrodynamical simulations, semianalytical models, or statistically inferred results from the H I mass or star formation rate (SFR) distribution of galaxies in clusters and/or groups.

Throughout the paper, we assume a Lambda CDM cosmology, with $\Omega_{\rm m}=0.3$, $\Omega_\Lambda=0.7$, and $h=0.7$, and use the Chabrier (2003) initial mass function when estimating the stellar mass or SFR. We only consider neutral atomic gas in this paper, since H I disks are usually much more extended than molecular gas and thus more likely to be stripped. In addition, it is probably the major component of neutral gas in low-mass galaxies (Saintonge et al. 2017). All measurements obtained in this paper can be found in Appendix J.

2. Sample and Data

2.1. The NGC 4636 Group

The N4636G is centered at $\alpha=190\overset{\circ}{.}7084$, $\delta=2\overset{\circ}{.}6880$ (Reiprich & Böhringer 2002), at a distance of 16.2 Mpc and a heliocentric velocity of 919 km s^{-1} (PGC1–42734 in Kourkchi & Tully 2017, hereafter K&T17). X-ray analysis suggests that the group has a characteristic radius of 0.61 Mpc, with an enclosed total mass of $M_{200}\sim 2.5\times10^{13}\,M_\odot$ (Reiprich & Böhringer 2002). Here the characteristic radius is taken as R_{200}, the radius within which the average density is 200 times the critical density of the universe. The 1D velocity dispersion, $\sigma_v\sim278$ km s^{-1}, is deduced from M_{200} following the relation by Evrard et al. (2008). We note that, although this relation is based on simulations of halos more massive than $10^{14}h^{-1}\,M_\odot$, it is compatible with the preliminary simulation results with a lower mass limit reported by Ferragamo et al. (2022).

We compile a catalog of galaxies around the N4636G center with redshift measurements from several H I and optical catalogs, which will be introduced later in Sections 2.2 and 2.3. We define the members of N4636G as galaxies having both a small projected distance ($d_{\rm proj}$) and a small relative radial velocity (Δv) with respect to the group's center. We require $d_{\rm proj}<2R_{200}$ and $|\Delta v|<v_{\rm esc,proj}$, where $v_{\rm esc,proj}$ is the projected escape velocity at $d_{\rm proj}$. We have removed possible interlopers and finally identified 119 galaxies potentially belonging to the group. Please refer to Appendix A for more details on escape velocity, interlopers, and possible influence of the nearby Virgo cluster.

Figure 1(a) shows the spatial distribution and redshifts of galaxies in N4636G. Figures 1(c) and (d) are the projected phase space diagrams (PSDs; e.g., Jaffé et al. 2015), which are able to qualitatively show the infalling status of galaxy members by plotting radial velocity and projected distance relative to the group center (e.g., Oman et al. 2013). The color-coding of these projected PSDs reflects gas-richness and star formation and will be discussed in Section 4.

2.2. H I Samples

Among 119 galaxies belonging to the group, 63 have H I detections. One pair of H I-detected galaxies (#110 and #111) are undergoing a merger. Their evolution is thus dominated by merging, instead of RPS or premerger tidal interaction. We thus exclude this pair from the following examination and call the remaining 61 galaxies the *H I sample*. The other 56 H I-nondetected galaxies are among the *optical-only sample*. The spatial distributions of H I and optical-only samples can be found at Figure 1(b).

Most of the H I sample is detected by either FAST, Arecibo Legacy Fast ALFA (ALFALFA; Giovanelli et al. 2005; Haynes

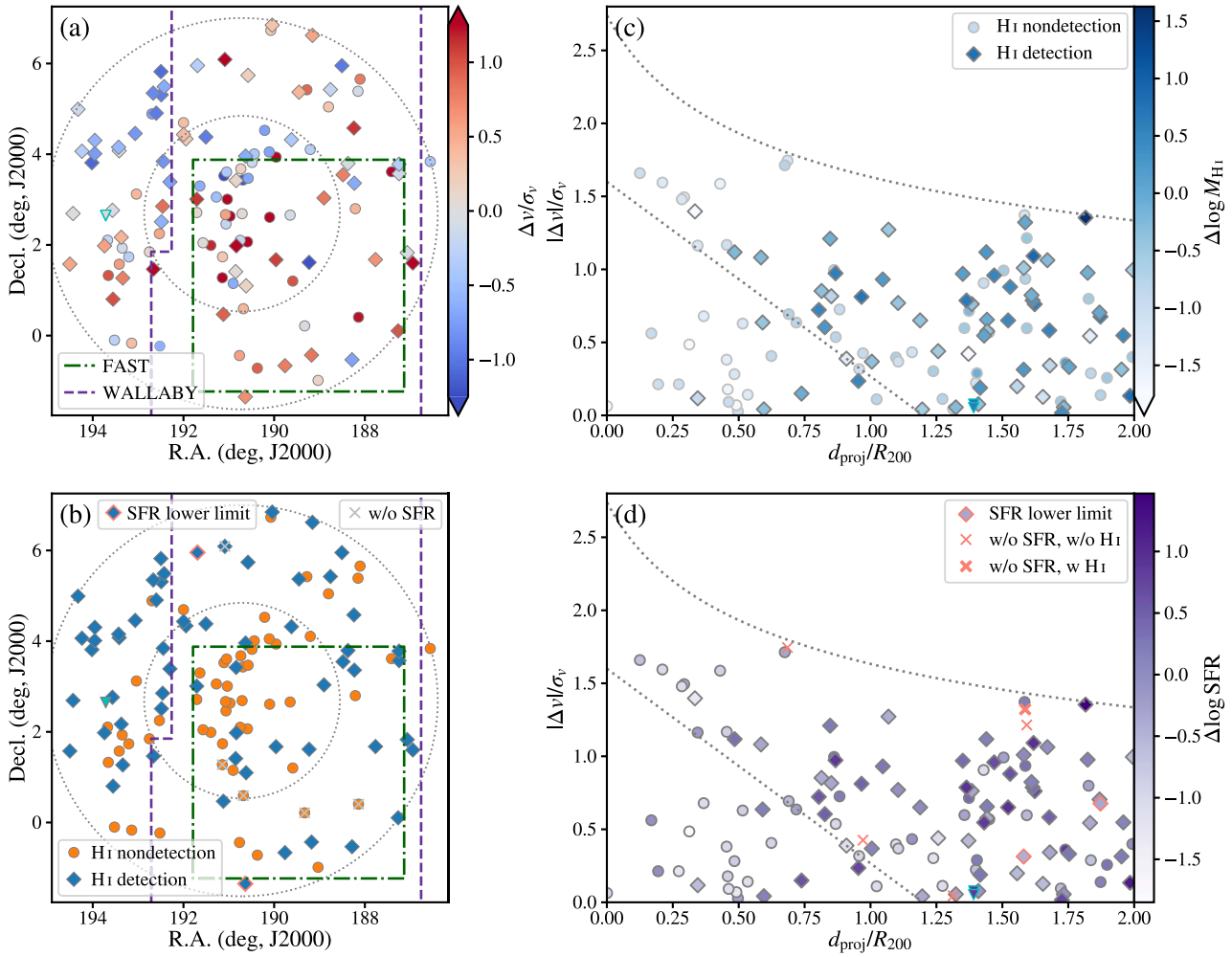

Figure 1. Overview of the galaxy samples. The galaxy pair (#110 and #111) are labeled as triangles with cyan edge. (a) The spatial distribution of galaxies, color-coded by radial velocities Δv relative to the group center. The observation fields of FAST (dashed–dotted green line) and WALLABY (dashed purple line) are drawn. Two dotted gray circles of radii one and two times R_{200} indicate the range of N4636G. (b) The spatial distribution of H I detections (blue diamonds) and nondetections (orange circles). Galaxies without SFR measurements are overlaid with gray crosses, and those with only lower-limit estimations of SFR are edged with salmon pink. (c) Galaxies plotted on projected PSD, color-coded by their deviations from the mean $M_{\rm H\,I}$ relation of local late-type galaxies (LTGs; see Figure 3). The abscissa is the projected distance $d_{\rm proj}$ from the center of N4636G normalized by R_{200}; the ordinate is $|\Delta v|$ normalized by N4636G's 1D velocity dispersion σ_v. H I nondetections (light-gray edged circles) are color-coded according to their upper limits of $M_{\rm H\,I}$ (see Section 4). The projected escape velocity $v_{\rm esc,proj}$ profile and the virialized region are plotted as dotted gray lines. (d) Projected PSD color-coded by deviations from the star-forming main sequence (SFMS; see Figure 3). H I detections and nondetections without SFR measurements are represented as bold and regular salmon crosses, respectively. Salmon-edged diamonds are galaxies with only lower limits of SFR.

et al. 2018), or WALLABY, all of which will be introduced below. Additionally, one H I-detected galaxy, #49, belongs to N4636G and is observed by H I Parkes All Sky Survey (HIPASS) only (Koribalski et al. 2004).

2.2.1. FAST Data

Using the single-dish radio telescope FAST (channel width $\sim$4 km s^{-1}, beam size $\sim$2.′9), Zuo et al. (2022) observed a $\sim 5^\circ \times 5^\circ$ square region covering N4636G, which is indicated in Figure 1(a). With the high sensitivity of FAST, they pushed the detection limit in H I mass by $\sim$0.4 dex deeper than that of the previous ALFALFA data. Specially, FAST provides four new H I-detections (#5, #24, #33, and #58). When the H I flux is measured with more than one telescope, the FAST flux is preferred, except for two galaxies near the edge of the FAST field (#4 and #77). In the end, the H I fluxes of 17 galaxies are obtained with FAST.

2.2.2. ALFALFA Data

The ALFALFA survey observed the northern sky and thus covers a large fraction of the N4636G (Haynes et al. 2018). It detects 57 H I sources belonging to the group. Zuo et al. (2022) showed the high level of consistency between the FAST and ALFALFA fluxes for overlapping sources in the N4636G. After excluding FAST-detected sources and merger systems, ALFALFA provides fluxes for 42 galaxies in the H I sample.

2.2.3. WALLABY Data

The WALLABY pilot survey (Westmeier et al. 2022) observed the NGC 4636 field, and the footprint is plotted in Figure 1(a). As an interferometric H I survey, WALLABY has a beam size of $\sim$30″ and can provide moderate-resolution H I maps (e.g., Wang et al. 2021). Among 19 galaxies detected by WALLABY belonging to this group, five galaxies have data with enough resolution to study their moment (0) maps (see also the discussion in Sections 3.5 and Appendix B). They also

enable checking of the ALFALFA and FAST fluxes for possible contamination from neighbors. One such contamination is identified (#79 detected by ALFALFA), and we adopt the H I flux measured with WALLABY. A comparison between the Australian Square Kilometre Array Pathfinder (ASKAP) and ALFALFA fluxes for galaxies in N4636G can be found in Westmeier et al. (2022).

2.3. The Super Catalog of Redshifts

We compile the super catalog of these 119 group member galaxies with redshift measurements by combining the K&T17 galaxy catalog (91 galaxies; 45 H I-detections), the Sloan Digital Sky Surveys (SDSS) Data Release (DR) 16 `SpecObj` table (79; 32, Dawson et al. 2016; Ahumada et al. 2020), and four new H I-detections by FAST. These catalogs are cross-matched with each other to remove the duplicates. The redshift values from H I surveys are preferred to those from optical catalogs, and those by the SDSS DR16 are preferred to the other optical ones. The final super catalog is presented in Appendix J.

2.4. The SDSS and DECam Images

We use *g*- and *r*-band images from SDSS DR12 (York et al. 2000; Alam et al. 2015) and the DECam Legacy Survey (DECaLS) DR9 (Dey et al. 2019) for optical photometric measurements. SDSS has typical seeings (as FWHM) of $1\farcs44$ and $1\farcs32$ in both bands, respectively, and the corresponding depths are 21.84 and 20.84 mag. For DECaLS, these parameters are $1\farcs29$, $1\farcs18$, 23.72, and 23.27 mag, respectively.

Since the resolution and depth of DECaLS are slightly better than those of SDSS, DECaLS images are preferred to study dwarf galaxies. The background removal pipeline of DECaLS, however, is not optimized for extended sources, and large galaxies suffer from flux loss on the periphery (Dey et al. 2019). Therefore, we use SDSS photometry for our *high-mass galaxies* ($M_* \geqslant 10^9\,M_\odot$) and DECaLS photometry for *low-mass galaxies* ($M_* < 10^9\,M_\odot$). Since some of our discussions below divide the sample into low- and high-mass subsets, such a choice of optical survey provides consistency. More details on combining these two types of fluxes are presented in Appendix C.

3. Measurements

3.1. Optical Photometry

We make cutouts of images centered on each galaxy. Since the sample galaxies typically have a spatial extent comparable to the field of view of SDSS, SDSS image frames are mosaicked using *SWarp*[25] (Bertin et al. 2002), with overlapping regions averaged. Because the downloaded images have gone through initial background subtraction, no additional background removal is conducted during mosaicking. A few frames have problematic background removal by the SDSS pipeline, and they are discarded. DECaLS images are processed with the same procedure if the images that we downloaded are not large enough to cover the whole galaxy.

The general procedure of the photometric pipeline is the same as that of Wang et al. (2017). The main steps are as follows:

1. *Masks.* We deblend and mask contaminating light from neighboring sources. We combined *SExtractor*[26] (Bertin & Arnouts 1996) and *photutils* (Bradley et al. 2021) to generate masks, based on the *r*-band image from SDSS or DECaLS. A "cold and hot" method (e.g., Rix et al. 2004) is applied. In the "cold" mode, we run SExtractor twice. The first run, with detecting threshold set to 1.5σ, detects all clearly separated neighboring sources and masks them. The second run, however, unmasks faint clumpy features possibly belonging to the peripheral parts of the target by setting a threshold of 1.0σ and a deblending parameter of 0.005. In the "hot" mode, foreground stars are detected using `DAOStarFinder` in photutils, with a box size of 10×10 pixels for background estimation, detection threshold as 5σ, and roundness threshold as 0.7. A star candidate is masked only if its peak is larger than five times the local background level and is not around the galaxy center. All masks are dilated by 1.5 times the seeing size, checked with *g*-band images, and manually adjusted if necessary.
2. *Background subtraction and galaxy geometry.* After we flag the pixels belonging to the sample galaxy and those masked in the last step, the background of the image is modeled using a 2D linear equation and removed. We replace the masked pixels with the centrosymmetric or the azimuthally averaged value around the galaxy center. Function `detect_sources` of photutils is used to measure the center, position angle, and ellipticity with a threshold of 1.5σ.
3. *Surface brightness (SB) profile.* The geometry parameters of *r*-band images are used for generating photometric annuli of all bands. We measured the 3σ clipped average value in each elliptical ring as the SB. At the outer region, annuli enlarge with a geometric step of 1.05 times. When 15 contiguous annuli's SB values are linearly uncorrelated with their sizes by a *p*-value of 0.05 (using an *F*-test), we consider the profile flattens hereafter. The size ratio between the largest and the smallest of these 15 annuli is typically around 2. The 3σ clipped average of these 15 values is subtracted as residue background, and 10 times their clipped standard deviation is used as the threshold for final profile.
4. *Total fluxes.* We then measure the growth curve (GC) of the flux within each elliptical aperture as a function of aperture size. Again, the GC is considered flattened with 15 uncorrelated contiguous flux values. The 3σ clipped average of these 15 values is then considered to be the total flux of the galaxy, and their scatter is taken as the uncertainty. Some of the GCs rise or fall slightly beyond the flat region and then flatten again, and we attribute it to variations in the local background. We take the extent of rise or fall as the extra uncertainty of background estimation and propagate this into the uncertainty of the flux.

Dey et al. (2019) reported that the difference between fluxes measured by DECaLS and SDSS can be modeled as a cubic function of $g - i$ color in SDSS. We use the SDSS color measurements and this model to remove the systematic difference of DECaLS fluxes from the SDSS ones. For consistency, the *g*- and *i*-bands' SDSS fluxes used here are

[25] https://github.com/astromatic/swarp/releases/tag/2.41.4

[26] https://github.com/astromatic/sextractor/releases/tag/2.25.0

measured with the GC method using apertures based on the DECaLS r-band geometric parameters.

For all fluxes, the Galactic extinction is corrected based on the dust map of Schlegel et al. (1998) and the extinction curve of Cardelli et al. (1989).

3.2. Size

We characterize the size of stellar disk with $R_{25,g}$, the radius at which the SB drops to 25 mag arcsec^{-2}. The $R_{25,g}$ is derived through linearly interpolating the g-band SB profile. We want to use this radius to trace the edge of disk growth, and thus it is defined in g band here, which is relatively blue.

By cubically interpolating the GC, we also get the radii enclosing 50% and 90% of fluxes, R_{50} and R_{90}, in the r band. The r band is used here instead, in order to track the radial structure of stellar mass dominated by old stars.

We note that the so-called *radius* here is always the semimajor axis of the corresponding elliptical annulus, accounting for projection effects.

3.3. Color

We calculate for each galaxy the total $g-r$ color and $g-r$ color profile, the latter of which is truncated when the uncertainty reaches 0.1 mag. We further define three localized color parameters of each galaxy at the center, at R_{50}, and at $2R_{50}$, denoted as $(g-r)_0$, $(g-r)_{R_{50}}$, and $(g-r)_{2R_{50}}$, respectively. They are derived from regions within $0.2\sqrt{2}R_{50}$, between 0.8 and $1.25R_{50}$, and between 1.6 and $2.5R_{50}$, based on the GC.

3.4. Stellar Mass and SFR

The total $g-r$ is converted to the r-band stellar mass-to-light ratio following Zibetti et al. (2009). We then determine the stellar mass with the r-band luminosity. Stellar mass profiles are obtained similarly using the r-band SB profiles and $g-r$ color profiles after correction for the inclination, with the assumption of infinitely thin disks.

We obtained SFRs following the methods of Wang et al. (2017). The same photometric pipeline of Wang et al. (2017) is used to derive fluxes from the Galaxy Evolution Explorer (GALEX; Martin et al. 2005) and the Wide-field Infrared Survey Explorer (WISE; Wright et al. 2010) images.

W4-band images from WISE are used for an estimate of the dust-attenuated part of the SFR, with far-ultraviolet (FUV) images from GALEX for the unattenuated part. Near-ultraviolet (NUV) data are used when FUV images are unavailable. The luminosity in each band is converted to SFR using the equations of Calzetti (2013). There are 58 galaxies out of 119 having no FUV images, and three of them are also missing NUV data (#49, #65, and #75). W4-band luminosities provide the lower-limit estimation of SFR for #49 and #75, leaving the H I-detected galaxy #65 without SFR measurement. Additionally, H I-nondetected #28, #50, and #69, although covered by GALEX, have neither ultraviolet nor W4 detection and as a result have no SFR measurement either.

3.5. H I Properties

H I mass values are calculated using H I fluxes from the catalog compiled in Section 2.2. We derive the size of H I disk, $R_{\rm H\,I}$, from H I mass, using the relation given by Wang et al. (2016, with a ∼0.06 dex scatter), where $R_{\rm H\,I}$ is the radius where H I surface density reaches 1 $M_\odot$ pc^{-2}. For 11 galaxies with a derived $R_{\rm H\,I}$ larger than $b_{\rm maj}\sqrt{a/b}$, we also measured their $R_{\rm H\,I}$ from their WALLABY moment (0) map. Here, $b_{\rm maj}$ is the WALLABY beam FWHM (∼30″ or 2.3 kpc), and a and b are the major-axis and minor-axis of the galaxy measured from optical images. We confirmed that they indeed follow the relation after correcting the smearing effect by adopting $R_{\rm H\,I} = \sqrt{R^2_{\rm H\,I,obs} - (b_{\rm maj}/2)^2}$ (Wang et al. 2016), where $R_{\rm H\,I,obs}$ is the radius directly derived from the deprojected surface density profile. The ellipticity of the H I disk is assumed to be the same as that of the stellar disk. More discussion on $b_{\rm maj}\sqrt{a/b}$ as the criterion of selecting a reliable $R_{\rm H\,I}$ directly measured from images can be found at Appendix B.

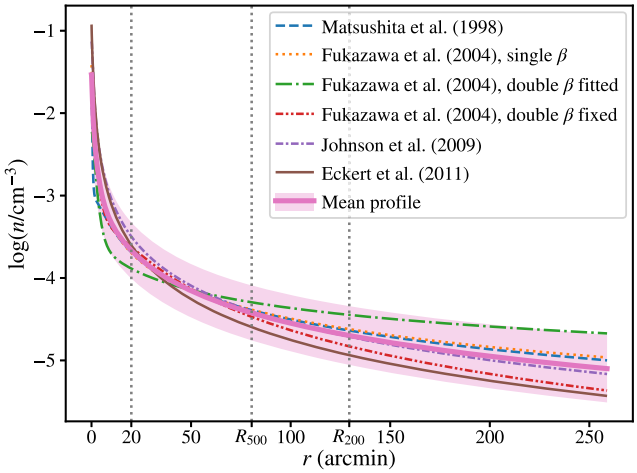

Figure 2. Different ICM density models for N4636G from the literature (see the legend) and the averaged ICM density profile (bold pink line). The pink shaded region indicates the uncertainty, considering the scatter of different models and the uncertainty of $M_{\rm gas,500}$ estimation. Historical X-ray surveys covered less than 20′ (vertical dotted gray line) from the group center. The R_{500} and R_{200} of N4636G are also drawn as vertical lines.

3.6. ICM Properties

We use the findings of earlier publications to create a reasonable model of the ICM density profile $\rho(r)$ of N4636G. The final ICM number density profile $n(r)$, shown in Figure 2, is the geometric average of six different models of this group from the literature (Matsushita et al. 1998; Fukazawa et al. 2004; Johnson et al. 2009; Eckert et al. 2011). These models are normalized to a uniform ICM mass within R_{500}, $\log(M_{\rm gas,500}/M_\odot) = 11.72 \pm 0.32$. Beyond $r = 20'$, our averaged model can be well fitted as

$$n(r) = 11.7 \times 10^{-3}\,{\rm cm}^{-3}(r/{\rm arcmin})^{-1.32}, \quad (1)$$

with a scatter of ∼0.3 dex.

We caution that the actual measurements of X-ray brightness, from which these models were derived, are limited to a small radial range of 20′ ($\sim R_{200}/6$) from the group center. The ICM mass density is $\rho(r) = 1.4 m_{\rm p} n(r)$, where $m_{\rm p}$ is the mass of the proton, and where the factor 1.4 accounts for the presence of helium. Similar to R_{200}, R_{500} is the radius within which the average density is 500 times the critical density. The value of $M_{\rm gas,500}$ is calculated from M_{200} following Sereno et al. (2020).

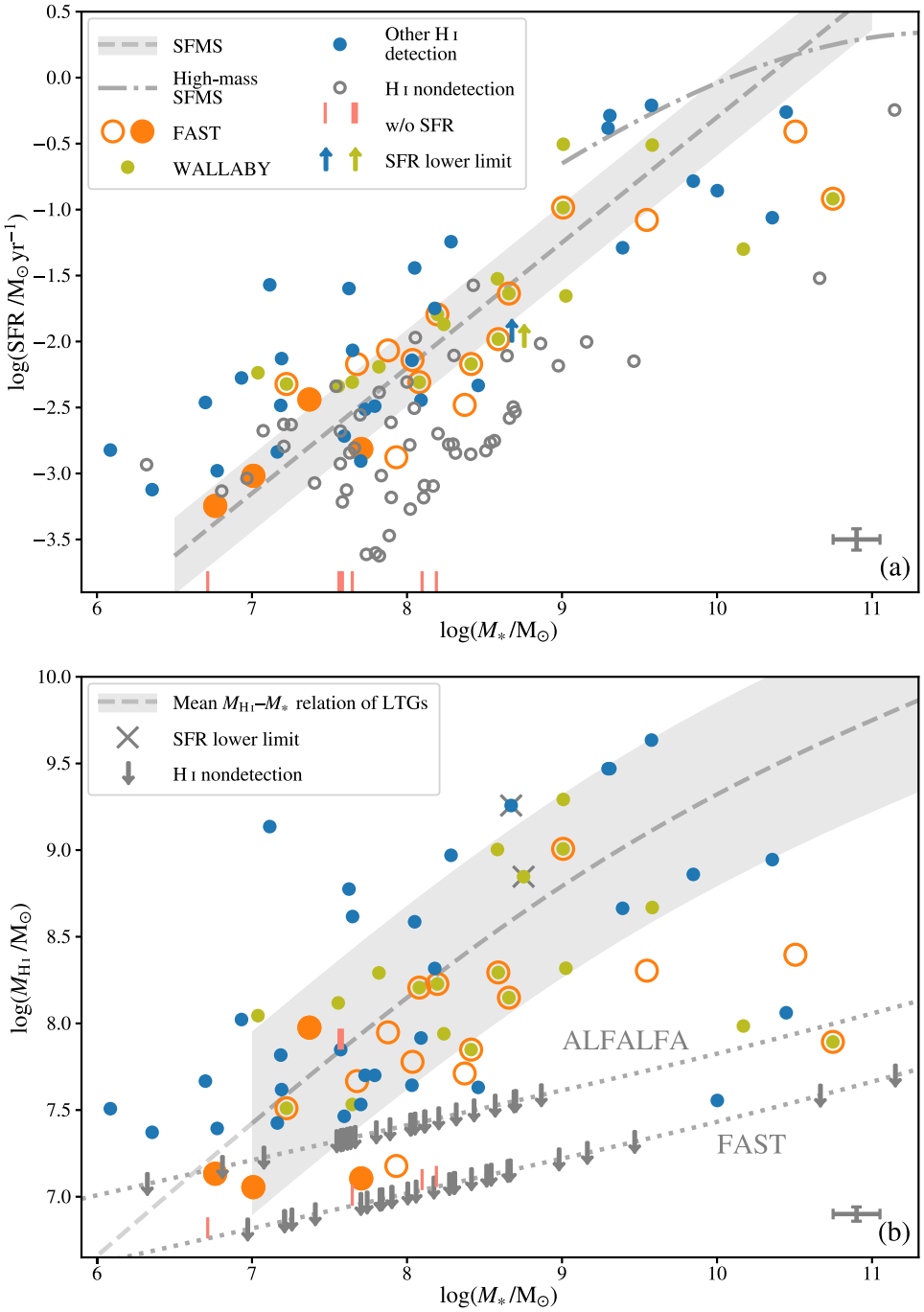

Figure 3. The SFR and H I mass ($M_{\rm H\,I}$) of our sample galaxies, compared with the average relation from star-forming nearby galaxies. (a) SFR vs. stellar mass M_*. H I nondetections are indicated by empty gray dots; H I detections by WALLABY, FAST, and previous H I surveys are plotted as olive dots, orange circles, and blue dots, respectively. Estimations of lower limits of SFR are plotted as upward arrows in the corresponding color. All WALLABY detections have been covered by previous ALFALFA or HIPASS surveys, while FAST provides four new H I sources (orange filled circle). The stellar masses of H I-detected and -nondetected galaxies without SFR measurements are pointed out with bold and regular vertical salmon ticks, respectively. As a reference, the fitted local SFMS from Cook et al. (2014) is given as dashed gray line, and the scatter of 0.29 dex is given as the shaded region. The local SFMS of high-mass galaxies from Saintonge et al. (2016) is also plotted as the dashed–dotted gray line. The typical uncertainties of data points are plotted at the lower-right corner. (b) $M_{\rm H\,I}$ vs. M_*. Most of the symbols are the same as those in panel (a). The upper limits of $M_{\rm H\,I}$ (dotted gray line) of H I nondetections (gray arrow) are provided, calculated with FAST or ALFALFA parameters according to their coordinates. Galaxies that only have lower limits of SFR are overlaid with gray crosses. The mean $M_{\rm H\,I}$ relation of local LTGs from Calette et al. (2018) is plotted as dashed gray line, with the extrapolated part of $M_* < 10^7\,M_\odot$ translucent. Its scatter of 0.53 dex is given as shading. The typical uncertainties are also given.

4. Overview of the Galaxy Population

We present our measurements of SFR and H I mass $M_{\rm H\,I}$ in Figure 3 against the stellar mass M_*. We also plotted the star-forming main sequence (SFMS; from Cook et al. 2014) and the mean $M_{\rm H\,I}$ relation of local late-type galaxies (LTGs; Calette et al. 2018) for comparison.

It is clear that most of H I detections lie very close to the SFMS (1.5 dex below it at most), which is consistent with the

view that the galaxies need neutral gas to sustain the star formation (Wang et al. 2020a; Guo et al. 2021).

Our H I sample generally follows and scatters around the mean $M_{\rm H\,I}$ relation. At the high-mass end, one can find H I detections nearly 2 dex below the relation; at the low-mass end, however, the detection limit meets the relation, which results in a bias toward gas-rich galaxies. Notwithstanding, FAST lowers the limit by ∼0.4 dex compared with ALFALFA (Zuo et al. 2022). For the optical-only sample, we estimated the upper limit of $M_{\rm H\,I}$ mainly following Wang et al. (2021), which is based on the rms of data and the line widths predicted from the baryonic Tully–Fisher relation (McGaugh et al. 2000). We confirm that the predicted line widths are all larger than the velocity resolution.

The offset relative to the SFMS or the mean $M_{\rm H\,I}$ relation can be seen as an indicator of star formation strength or H I richness (e.g., Schiminovich et al. 2010). We denote them as $\Delta\log {\rm SFR} := \log({\rm SFR}/{\rm SFR_{MS}})$ and $\Delta\log M_{\rm H\,I} := \log(M_{\rm H\,I}/M_{\rm H\,I,MS})$. By doing so, the underlying dependence on M_* in galaxy evolution (i.e., the secular evolution) is removed in a first-order approximation. In this study, we refer to the galaxies above (or below) the mean $M_{\rm H\,I}$ relation as *gas-rich* (or *gas-poor*) ones.

Figures 1(c) and (d) show how $\Delta\log M_{\rm H\,I}$ and $\Delta\log {\rm SFR}$ change as a function of position in the projected PSD, which roughly indicates the infalling stage. There is a general trend that both offsets drop toward the group center. In particular, they decrease significantly inside the virialized region (triangle bordered by gray dashed lines), suggesting that galaxies there have been strongly processed by environmental effects recently or in the distant past.

5. Quantifying the Tidal and Ram Pressure Effects

We consider two environmental effects, the gravitational tidal interaction (with an effect of either stripping or perturbation), and the hydrodynamic ram pressure (with an effect of either stripping or compression). We use two types of parameters to describe the effect of stripping: the strength of stripping at the optical-disk edge, and the fraction of strippable H I.

We note that we derive these two parameters from only the total H I flux; although, Wang et al. (2021) showed that it is possible to calculate them from an H I moment (0) map. The reason for this is that only five galaxies are resolved enough for this calculation (see Appendices B and E for more information). Still, we provide the atlas of these five galaxies and brief discussion in Appendix I.

5.1. The Strength of Stripping at the Optical-disk Edge

Elmegreen et al. (1991) described the strength of tidal interaction in simulations using

$$\frac{M_{\rm p}}{M_{\rm g}}\left(\frac{R_{\rm g}}{\delta}\right)^3\frac{\Delta t}{T}. \tag{2}$$

This quantity compares the impulse transferred by tidal force and the inherent momentum of self-revolution. Here "p" and "g" denoted the perturber and the target galaxy, respectively, M is the total mass of galaxy, $R_{\rm g}$ is the characteristic radius of "g," and δ is the minimum distance between these two galaxies during the whole encounter. The value Δt is the interaction time, measured as the time needed for "p" to rotate 1 rad with respect to "g" when they are nearest, while T is the time for "g" to self-rotate 1 rad.

Wang et al. (2022) modified Equation (2), made it suitable for observation, and explored the effects of tidal interaction on the optical disk in the Eridanus supergroup. They replaced the minimum distance δ with the current projected distance $\delta_{\rm proj}$, and calculate Δt using the difference of heliocentric radial velocity $\Delta v_{\rm rad}$. They defined

$$\begin{aligned} S_{\rm tid} &= \sum_{\rm all\ p}\frac{M_{\rm p}}{M_{\rm g}}\left(\frac{R_{\rm g}}{\delta_{\rm proj}}\right)^3\frac{\Delta t}{T} \\ &= \sum_{\rm all\ p}\frac{M_{\rm p}}{M_{\rm g}}\left(\frac{R_{\rm g}}{\delta_{\rm proj}}\right)^3\frac{\delta_{\rm proj}/\sqrt{(\Delta v_{\rm rad})^2+V_{\rm circ}^2}}{R_{\rm g}/V_{\rm circ}}, \end{aligned} \tag{3}$$

which is summed over all possible perturbers "p." In Equation (3), the ratio $\Delta t/T$ is transformed into the ratio of angular velocity. The $V_{\rm circ}$ is the circular velocity of "g" calculated from the baryonic mass of the galaxy with the Tully–Fisher relation (McGaugh et al. 2000), using the sum of stellar mass and the helium-corrected H I mass. If the galaxy is H I-nondetected, the upper limit of $M_{\rm H\,I}$ is used. The $V_{\rm circ}$ term in $\sqrt{(\Delta v_{\rm rad})^2+V_{\rm circ}^2}$ is a smooth parameter introduced by Wang et al. (2022) to avoid zero divides, but it also reflects that when two galaxies have a low relative velocity, the circular velocity determines the timescale of tidal interaction.

We follow the procedure of Wang et al. (2022) to derive $S_{\rm tid}$. The total mass M of the galaxy is estimated as $V_{\rm circ}^2 R_{25,g}/G$, where G is the gravitational constant. The characteristic radius $R_{\rm g}$ is chosen as the $R_{25,g}$. We note that $M_{\rm p}$ should have been the total mass within the virial radius of the perturber's dark matter halo, instead of just within $R_{25,g}$. Theoretically and in a first-order approximation, however, the optical-disk size linearly scales with the virial radius (Mo et al. 1998), and thus our $M_{\rm p}$ is roughly a uniformly scaled estimate. Since in this study only the relative values of $S_{\rm tid}$ are important, this systematic offset of total mass is to some extent properly accounted for. The major uncertainty is from the projection effects, which we estimate using simulation data as 0.41 dex (see Appendix D).

Massive galaxies surrounding the group could add to the tidal interaction. Using the coordinate and redshift-independent distance in the Cosmicflows-3 catalog (Tully et al. 2016, hereafter CF3), we found 13 galaxies within $3R_{200}$ from the center of N4636G that are not in our sample. They are included as potential perturbers. Their stellar masses are measured using SDSS images, and ALFALFA H I fluxes are adopted when possible.

We generalize the idea of $S_{\rm tid}$ to express the strength of RPS as

$$S_{\rm RPS} = \frac{P_{\rm ram}}{F_{\rm anch}(R_{25,g})}, \tag{4}$$

where $P_{\rm ram}$ is the ram pressure, estimated as $\rho(d_{\rm proj})(\Delta v)^2$ (Gunn & Gott 1972), where $\rho(r)$ is the volumetric mass density of the ICM at a distance r from the group center. The anchoring force $F_{\rm anch}$ describes the gravity exerted on gas from the stellar disk and the gas disk itself, estimated as (Wang et al. 2021)

$$F_{\rm anch} = 2\pi G(\Sigma_* + \Sigma_{\rm gas})\Sigma_{\rm gas}, \tag{5}$$

where G is the gravitational constant, and Σ_* and $\Sigma_{\rm gas}$ are deprojected stellar and cold-gas surface density, respectively. The value at $R_{25,g}$ is used. We mostly follow the method of Wang et al. (2021) for the determination of RPS parameters. More details of $F_{\rm anch}$ are given in Appendix E. The major source of uncertainty for $S_{\rm RPS}$ is $P_{\rm ram}$, the projective random uncertainty of which is estimated as 0.48 dex using simulation data (see Appendix D for more discussion).

We note that, due to the way that $P_{\rm ram}$ is derived, $S_{\rm RPS}$ can practically extend to physically meaningless infinitely low values when the galaxy evolution is almost unaffected by RPS. Relatedly, $S_{\rm RPS}$ has a much larger dynamical range (∼6 dex) than $S_{\rm tid}$ has (∼2 dex). We thus manually set $S_{\rm RPS}$ for galaxies with $\log S_{\rm RPS} < -3.2$, which are 10% of the sample, as invalid, assuming the RPS effect on these galaxies to be insignificant in galaxy evolution. As shown later in Section 6.1, this does not change our classification of RPS- or TS-dominant galaxies (introduced in Section 5.4).

5.2. The Extent of Stripping: Fraction of Strippable H I

We follow the method of Wang et al. (2021) to derive $f_{\rm RPS}$ that represents the extent of RPS within the galaxy. This parameter measures the fraction of H I gas that is subjected to RPS, i.e., with $P_{\rm ram} > F_{\rm anch}$. The method makes use of the H I size–mass relation, assuming a characteristic H I-surface-density profile (Wang et al. 2020a) that we truncate at $1.5R_{\rm H\,I}$. We summarize the technical details in Appendix E.

We further define a similar parameter for TS, $f_{\rm tid}$. The main idea is to generalize $S_{\rm tid}$ to each radius r in the galaxy and to use a critical value $S_{\rm tid,crit}$ to determine the stripping radius. The conventional definition of tidal truncation radius (Merritt 1984; Taffoni et al. 2003) is not adopted here because it is purely gravitational and does not account for hydrodynamic effects.

The tidal strength as a function of the galactocentric distance r is derived as

$$S_{\rm tid}(r) = \sum_{\rm all\ p} \frac{M_{\rm p}}{V_{\rm g}^2(r) r/G} \left(\frac{r}{\delta_{\rm proj}}\right)^3 \frac{\Delta t}{T} = \frac{V_{\rm circ}^2}{V_{\rm g}^2(r)} \frac{r^2}{R_{25,g}^2} S_{\rm tid}, \quad (6)$$

where the timescale ratio $\Delta t/T$ is fixed. The total mass within r is calculated with $V_{\rm g}(r)$, the rotational velocity of "g" at r. Lelli et al. (2017) gave an observational relation between the localized radial acceleration $g(r) = V_{\rm g}^2(r)/r$ and the stellar gravitational field profile, which we calculate using the stellar mass $M_*(r)$ within r as $g_* = GM_*(r)/r^2$. Therefore, we can derive

$$S_{\rm tid}(r) = \frac{g(R_{25,g})r}{g(r)R_{25,g}} S_{\rm tid}. \quad (7)$$

We assume that the tidal interaction affects all mass outside of tidal radius $R_{\rm tid}$, which satisfies $S_{\rm tid}(R_{\rm tid}) = S_{\rm tid,crit}$. Here, $S_{\rm tid,crit}$ is the critical value that will be introduced in Section 6.1.1. Then $f_{\rm tid}$ is calculated as the fraction of gas outside of $R_{\rm tid}$. Similar to $f_{\rm RPS}$, those values of $f_{\rm tid}$ smaller than 1% are set to 0.

One would assume that the influence of tidal interaction would also be reflected in the stellar population. We confirm that six galaxies have $R_{\rm tid} < R_{25,g}$, all of which are dwarf galaxies (#5, #57, #58, #79, #107, and #112). We find obvious irregularity and asymmetric structures in three by visual inspection (#5, #58, and #79). However, since these dwarf galaxies are faint and it is hard to estimate the intrinsic irregularity of them, we thus did not quantify this and consider this question beyond the scope of this paper.

5.3. The Difference between S and f

Both f and S quantify the significance of environmental effects but describe different aspects. The major cause is that H I and stellar (or star-forming) disks have distinct radial profiles and extensions. For example, an H I-rich, massive galaxy may simultaneously have a high f and a low S: a significant portion of the H I could extend beyond the stellar disk, while the environmental forces at $R_{25,g}$ are not high enough compared to the restoring ones. Thus, f reflects the frontier of gas stripping while S describes the environmental influence at the edge of the stellar disk. The latter will be used to study the dependence of the consequent or instantaneous optically related properties of the galaxy on environmental effects (Section 6), and the former will be used to construct continuity equations to trace the process of gas stripping (Section 7).

5.4. The (Lack of) Correlation between RPS and TS Instantaneous Strengths

We examine the correlation of strengths between RPS and TS with the two types of parameters defined above.

We note that, while $S_{\rm RPS}$ and $S_{\rm tid}$ are defined in a similar way, they should not be directly compared. Indeed, their respective roles as *perturbation* and *stabilizer* are quite different. However, it is reasonable to compare the rank values. In Figure 4(a), we plot two S's against each other. The $S_{\rm RPS}$ and $S_{\rm tid}$ show no significant rank correlation, measured by the Spearman rank correlation coefficient ($r_{\rm s} = 0.12$). This indicates that the instantaneous strengths of RPS and tidal interaction are independent.

In Figure 4(b) we plot the two f's, and they show a moderate rank anticorrelation ($r_{\rm s} = -0.41$), implying that the two effects prefer different working conditions. Thus for most galaxies, one type of stripping clearly overrides the other one at a time. We define our *RPS sample* (27 galaxies) and *TS sample* (22) as those with $f_{\rm RPS} > f_{\rm tid}$ and $0 \neq f_{\rm tid} \geqslant f_{\rm RPS}$, respectively. Among these 49 galaxies, 25 have both $f_{\rm RPS}$ and $f_{\rm tid}$ larger than 0, indicating that they are undergoing RPS and TS simultaneously. Like $S_{\rm tid}$ and $S_{\rm RPS}$, the uncertainties of $f_{\rm tid}$ and $f_{\rm RPS}$ are predominantly caused by observational projection. We plot the typical values of uncertainties in the figure, and the estimation procedure is given in Appendix D.

We further investigate how the effects of RPS and TS processes are spatially distributed in N4636G. Figures 5(a) and (b) are maps of galaxies undergoing gas stripping by ram pressure and tidal interaction, respectively, color-coded by the corresponding S. A galaxy is plotted as a filled circle (RPS) or diamond (TS) as long as it has a nonzero value of the corresponding f, no matter how strong the other kind of stripping is.

One remarkable trend is that most galaxies undergoing TS are located in the northeast of the group while the southwestern part is almost void of such galaxies. In contrast, the galaxies undergoing RPS are spread over the entire volume of the group. Additionally, the galaxies with the largest values of $S_{\rm RPS}$ are within the R_{200} or

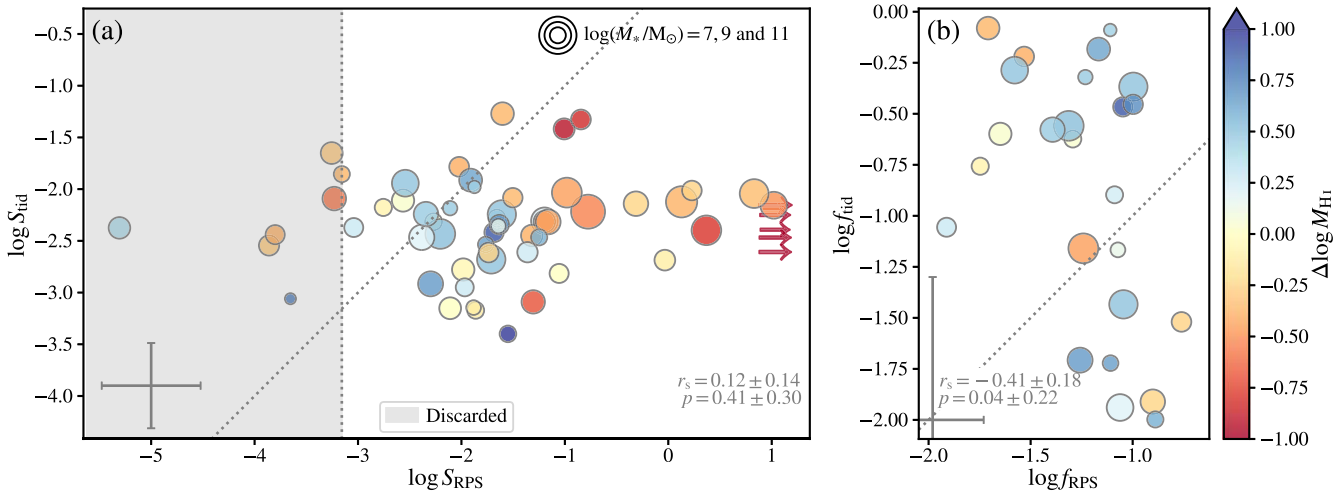

Figure 4. The relation between RPS and tidal interaction among H I-detected galaxies. Circles represent individual galaxies, color-coded by the deviation from the mean $M_{H\,I}$ relation. Their radii are proportional to the stellar mass. (a) Environmental strength S_{RPS} vs. S_{tid}. The Spearman rank correlation r_s and the p-value are given at the lower-right corner, the uncertainties of which are obtained with bootstrap. The last 10% of S_{RPS}'s are not included in correlation calculation and are covered with the gray shaded region. The line of $S_{RPS} = S_{tid}$ is drawn as the dotted gray line. Five galaxies have so little H I gas that $1.5R_{H\,I}$ is smaller than $R_{25,g}$. As a result, its S_{RPS} is infinite, and it is plotted as an arrow pointing rightward. The typical uncertainties of S_{tid} and S_{RPS} are given at the lower-left corner. (b) Strippable gas fraction f_{RPS} vs. f_{tid}. Only galaxies with both f nonzero are plotted. The line of $f_{RPS} = f_{tid}$ is drawn. The correlation between f_{RPS} and f_{tid} is given. The typical uncertainties of f_{tid} and f_{RPS} are given at the lower-left corner (only one side of the error bar is plotted due to limited space).

the east of N4636G. The value of S_{tid} shows no obvious relation with the position in the group. The trend corroborates the theoretical prediction of RPS and tidal interaction. At the group center, infalling galaxies get the largest relative velocity, and the ICM is densest, making RPS effective. While the galaxy number density is also the largest at the group center, which is favorable to TS, the high relative velocity shortens the impact time of possible galaxy–galaxy interactions.

Figure 5(c) gives the spatial distribution of the TS and RPS sample. In the southwest of N4636G, RPS galaxies are present, but no TS galaxies are found there. In the northeast, where the number density is higher, TS galaxies outnumber RPS ones. As we show in Appendix F, there seems to be abundant substructures in the eastern part of the group.

In summary, the TS and RPS instantaneous strengths and extents seem highly independent in N4636G with our models. The TS and RPS samples are distributed within a similar projected distance from the group center, but the TS is more sensitive to the presence of localized substructures. This may partly explain the relative independence of their strengths.

6. Dependence of Galactic Properties on Current Environmental Effects

6.1. The Change in H I Disk Size with Environmental Strengths

Figures 6(a) and (b) show how the H I disk size $R_{H\,I}$ (deduced from $M_{H\,I}$; see Section 3.5) changes with S_{tid} or S_{RPS}. We focus on low-mass galaxies (nonhatched circles) since they are thought to be more susceptible to environmental effects (Boselli et al. 2014). Some galaxies have their $R_{25,g}$ larger than $1.5R_{H\,I}$, the largest radius of our model H I profile. Their gas disks are heavily truncated, indicating that the gas depletion has almost finished. They will also have an infinite S_{RPS} with our methods. Thus, we do not include them in our analysis of this section and simply indicate them as short pink bars in Figure 6(a).

In Figure 6(a), no correlation is found between the size ratio and S_{tid} for H I-rich, low-mass galaxies. However, strong anticorrelations are found for H I-poor, low-mass galaxies, as in Wang et al. (2022).

Similarly, in Figure 6(b), H I-rich galaxies show a better correlation between the size ratio and S_{RPS} than H I-poor galaxies do. Also, galaxies that we discarded (with the lowest 10% of S_{RPS}, under gray shading) do not follow the relation, corroborating the idea that, with such a low S_{RPS}, other mechanisms, such as tidal interaction, play a larger role.

These anticorrelations indicate ongoing gas-stripping by ram pressure or tidal effects, which are likely to happen independently since no correlation is found between S_{tid} and S_{RPS} (see Figure 4). The drop of gas-richness (reflected by the size ratio here) should be the consequence of continuous stripping, while S's measure a more instantaneous process. Therefore, their correlation is likely due to the corresponding environmental process progressively strengthening during the infall of a galaxy. The stripping can also be self-enhancing: the removal of gas at the outskirts reduces the local anchoring force, which makes further stripping easier and which enlarges the corresponding S, possibly also giving rise to the anticorrelation.

The lack of correlation of the gas-rich sample, however, does not necessarily mean the absence of gas-stripping. It is possible that, for many of these gas-rich galaxies, neither TS nor RPS is well established, since the gas-rich sample also contains more newcomers to the group. This would be more significant if the gas-stripping is a cumulative process. It is also possible that weaker effects, like starvation, are more significant than direct stripping for gas-rich galaxies at this stage.

6.1.1. The Deviation of Critical Stripping Strength

The fitted relation (Figure 6(a)) for low-mass, gas-poor galaxies between the size ratio and S_{tid} intersects the line of $R_{H\,I} = R_{25,g}$. The intercept marks a critical value $\log S_{tid,crit} = -1.87 \pm 0.51$,[27] where the H I disk *has been* stripped close to

[27] The uncertainty is derived from bisector fitting results, and consistent with the uncertainty from projection.

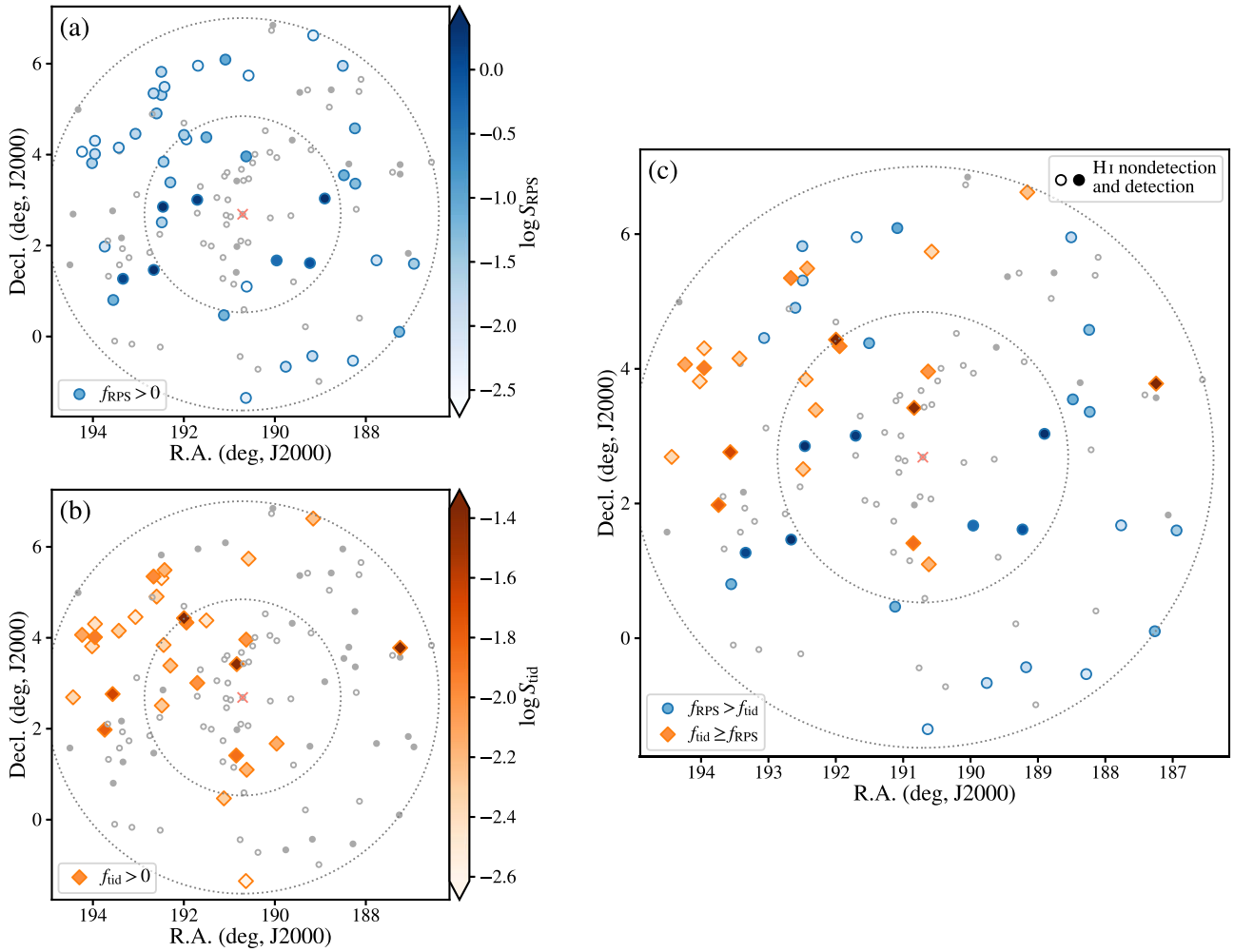

Figure 5. The spatial distribution of gas stripping. H I detections and nondetections are plotted as filled and empty symbols, respectively. Irrelevant galaxies (i.e., their corresponding $f = 0$) in each panel are plotted as gray dots. Two dotted gray circles of radii 1 and 2 times R_{200} indicate the range of N4636G, and the group center is labeled as a red cross. (a) The RPS strength map. Circles represent galaxies having gas strippable by ram pressure ($f_{\rm RPS} > 0$), color-coded by $S_{\rm RPS}$. The limits of the color bar are the 5th and 95th percentiles among all color-coded galaxies. (b) The tidal effect strength map. Galaxies having gas tidally strippable ($f_{\rm tid} > 0$) are plotted as diamonds, color-coded by $S_{\rm tid}$. The limits of the color bar are selected alike. (c) The stripping status map. Large colored symbols are those having strippable gas; blue circles are the RPS sample, and orange diamonds are the TS sample. They are color-coded exactly as those symbols in panels (a) and (b).

the radius $R_{25,g}$ while $S_{\rm tid}(R_{25,g}) = S_{\rm tid,crit}$. It naturally measures the level of $S_{\rm tid}$ needed for the TS to have obvious cumulative consequence, and we adopt it in the calculation of $f_{\rm tid}$. Due to the aforementioned chronology, the $f_{\rm tid}$ values might be slightly overestimated, since there is a delay between the onset and the completion of stripping. However, the overestimation is mitigated by the fact that H I disks can actually extend farther out than $R_{\rm H\,I}$.

In principle, we may calibrate a similar $\log S_{\rm RPS,crit}$ of -0.91 ± 0.55, and define $f_{\rm RPS}$ in a similar way to $f_{\rm tid}$. However, we notice the relatively large scatter and sparsity of data points near the intercept of Figure 6(b), and we thus prefer to stick to the well-established model of Gunn & Gott (1972). Nevertheless, we discuss how our major results may change if we use $S_{\rm RPS,crit}$ to derive $f_{\rm RPS}$ in Appendix G.3.

With the aforementioned intercepts, we could calculate the strippable gas fraction and select the RPS and TS samples as mentioned in Section 5.2. We replotted Figures 6(a) and (b) as Figures 6(c) and (d) with galaxies in the corresponding sample only. Galaxies in both samples show significant anticorrelations of the two parameters regardless of the gas-richness and stellar mass. This implies that the noncorrelation of the gas-rich sample in Figures 6(a) and (b) could be due to the fact that the relevant stripping process needs more time to show its effects. Additionally, the trends in Figures 6(c) and (d) are much tighter. This is possibly because, by selecting the TS and RPS sample, we removed galaxies with a lower signal-to-noise ratio in the S measurements, and simplified a more complex mixture of physical processes. The scatter is thus lowered.

We note that relations in Figures 6(a) and (b) are flatter than those in panels (c) and (d), probably due to the coexistence of two stripping mechanisms among many galaxies. The relations in Figures 6(c) and (d) give compatible intercepts with those given in panels (a) and (b), suggesting that our derivation of critical stripping strength is self-consistent.

6.2. The Radial Change of Color due to Tidal Interaction

Tidal forces could induce the redistribution of cold gas, either by stripping or by inflow. We examine the relation between $S_{\rm tid}$ and both the localized and global colors for the N4636G galaxies. When optimizing the photometric pipeline, we have separated the galaxies into two subsets, the low- and high-mass ones, with a dividing line at $M_* = 10^9\,M_\odot$. Such a

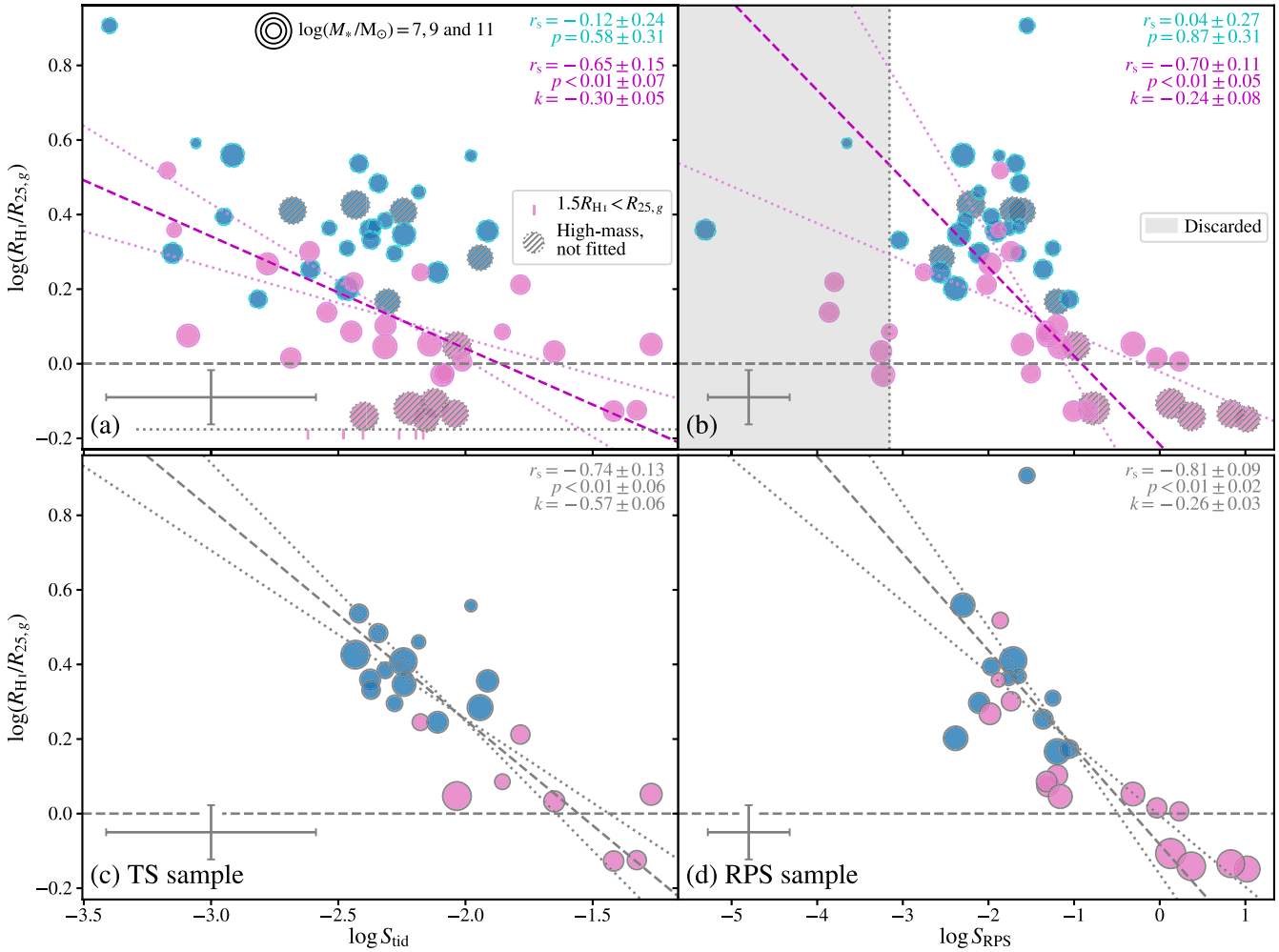

Figure 6. The relation between H I-to-optical-disk size ratio ($R_{\rm H\,I}/R_{25,g}$) and strengths of environmental effects in galaxies. The size of the symbols have the same meanings as those in Figure 4, and gas-rich and -poor galaxies are plotted as blue and pink circles, respectively. In panels (a) and (b), high-mass galaxies are hatched with gray lines and are *not* included in the linear fitting or correlation analysis. The typical uncertainties are given at the lower-left corner of each panel. (a) Size ratio plotted against tidal strength $S_{\rm tid}$. For *low-mass* gas-poor and -rich galaxies, the Spearman rank correlation $r_{\rm s}$ and the p-value are given at the upper-right corner in respective colors, the uncertainties of which are obtained with bootstrap. The bisector linear fitting of the low-mass gas-poor sample is plotted as the dashed magenta line, with two orthogonal fittings as dotted lines. The bisector fitting line crosses the $R_{\rm H\,I} = R_{25,g}$ line (dashed gray), at $\log S_{\rm tid} = -1.87 \pm 0.51$. The slope k of the line is also reported with the fitting uncertainty. (b) Size ratio plotted against RPS strength $S_{\rm RPS}$. Galaxies with the lowest 10% of $S_{\rm RPS}$'s are not used for correlation calculation or fitting, and they are covered in shading. The intercept of the bisector fitting line is $\log S_{\rm RPS} = -0.91 \pm 0.55$. Panels (c) and (d) are the same as (a) and (b), except that only the TS sample or the RPS sample is plotted, that high-mass galaxies are included, and that the gas-rich and gas-poor samples are not distinguished. The intercepts are -1.52 ± 0.27 and -0.34 ± 0.14, overlapping the 1σ confidence intervals of those in panels (a) and (b).

division is also supported by different patterns of reddening found in Wang et al. (2022) for the Eridanus group galaxies. Based on past ALFALFA observations, this line also divided galaxies into two groups exhibiting different properties (Huang et al. 2012), and in theory, it separates the regimes of galaxies being less and more prone to stellar feedback (Veilleux et al. 2005). We focus on the low-mass galaxies in the following because the high-mass TS subset is small (three galaxies). We notice that adding the high-mass galaxies to the low-mass subset would simply add noise to our calculations (shown in Appendix H).

6.2.1. The Trends

We show in Figure 7(a) that, for low-mass galaxies in the TS sample, the Spearman test indicates significant correlations of $g - r$ with $S_{\rm tid}$. In contrast, no significant correlations are found for the low-mass galaxies in the RPS sample (gray dots in Figure 7(a)), as TS is not the dominating mechanism for these galaxies. Similar correlations of low-mass galaxies in the TS sample are found for $(g - r)_{R_{50}}$ and $(g - r)_{2R_{50}}$ with $S_{\rm tid}$, but only tentative for $(g - r)_0$, as other panels of Figure 7 show.

We fitted the color with $S_{\rm tid}$ at three radii, and the bisector-fitted lines are shown in Figure 7. Compared with the relation at R_{50} (shown as the bold gray line), the line fitted at $2R_{50}$ (or galactic center) is redder (or bluer) than it. In addition, three fitted lines are parallel within the uncertainties. This indicates that, under tidal interaction, these galaxies statistically undergo a rather uniform reddening while retaining a blue core.

We exclude the possibility that the reddening is the result of dust attenuation, instead of tidal interaction, using the method by Wang et al. (2022, see their Figure 12). The global level of attenuation, $A_g - A_r$, is estimated from the W4-band and total SFR measurements (Calzetti et al. 2000; Wyder et al. 2007). A tight Spearman *anticorrelation* is found between $A_g - A_r$ and $S_{\rm tid}$ with $p < 0.05$, which strengthens the trends in Figure 7.

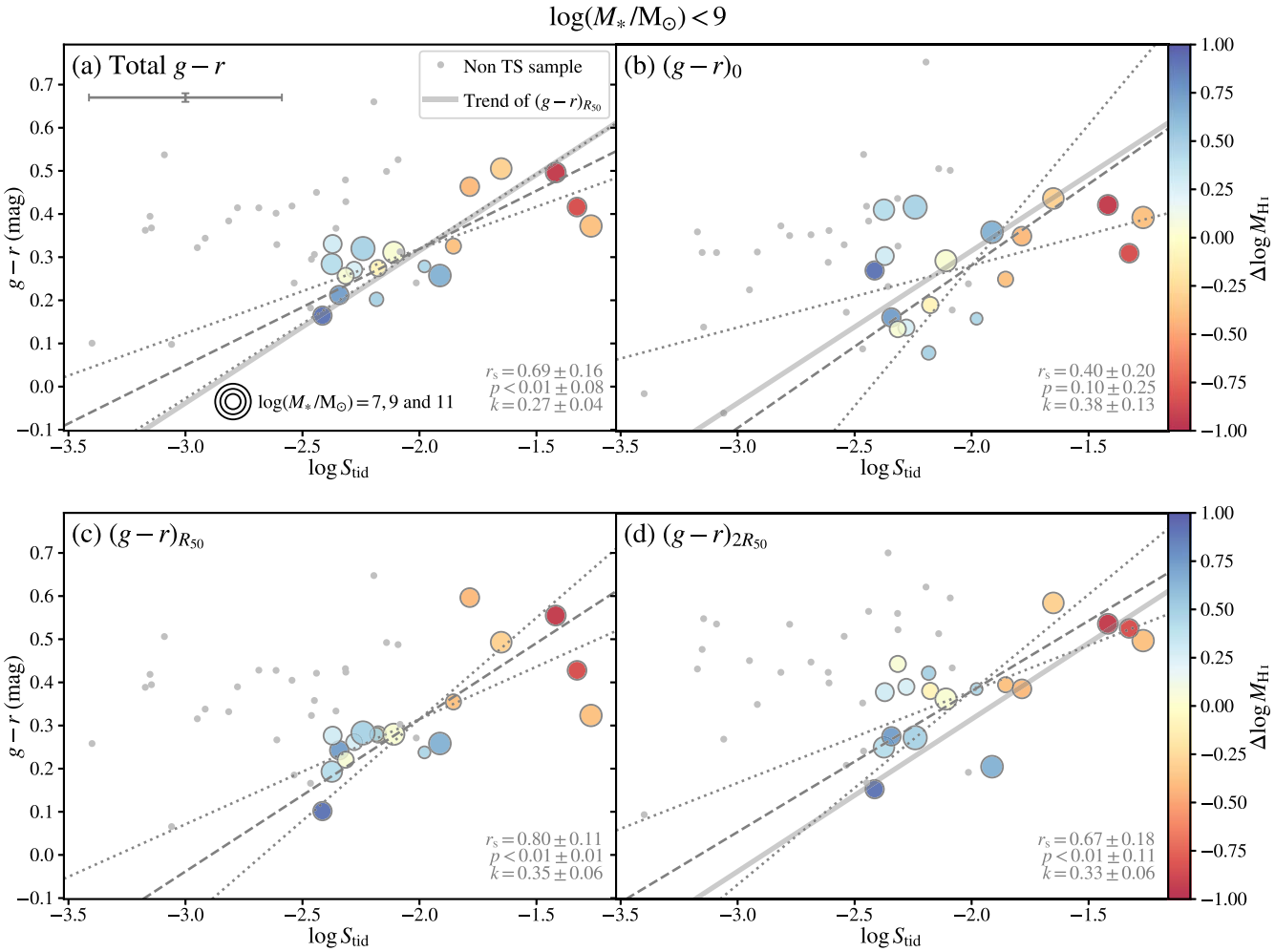

Figure 7. The $g - r$ color of H I-detected low-mass galaxies plotted against tidal strength $S_{\rm tid}$. The color is measured (a) using total fluxes, (b) at the galactic center, (c) at R_{50}, or (d) at $2R_{50}$ (see Section 3.3 for details). Galaxies in the TS sample ($f_{\rm tid} \geqslant f_{\rm RPS}$) are plotted as circles, color-coded as those in Figure 6. The size of circles represents stellar mass. For these galaxies, the Spearman correlation coefficient and the bisector fitting are given. The fitted line at R_{50} is plotted in all other panels as bold gray lines for comparison. Remaining H I detections are plotted as gray dots, all of which are not involved in correlation calculation or fitting. The typical uncertainties for low-mass TS galaxies are given in panel (a).

To better illustrate this uniform reddening, we replot Figure 7 as Figure 8, where the localized color is displayed as a function of galactocentric radius. The lines are color-coded by $S_{\rm tid}$. Among these 18 galaxies, 12 have $(g-r)_{R_{50}} - (g-r)_0 > -0.03$ mag and $(g-r)_{2R_{50}} - (g-r)_{R_{50}} > -0.03$ mag, where -0.03 mag accounts for uncertainty. If we do not consider the uncertainty, nine galaxies are strictly blue-cored.

We note that both $g - r$ color (global, at R_{50}, or at $2R_{50}$; see Figures 7 and 8) and H I richness (Figure 6(c)) are found to depend on $S_{\rm tid}$. They are known to correlate with each other, and both of them are known to correlate with other galactic properties. We thus use the partial Spearman rank correlation to find out how significant (p-value) and strong (r_s-value) $S_{\rm tid}$ directly influences the colors. We controlled for 10 possible parameters and calculated the respective partial rank coefficients between three different colors and $S_{\rm tid}$, shown in Figure 9. The correlations of all colors are still significant after fixing $d_{\rm proj}$, concentration C, or aggregate values like stellar mass, $M_{\rm H\,I}$, or SFR. But after being controlled for specific values from which the M_* is effectively divided (such as specific SFR (sSFR), $f_{\rm H\,I}$, $\Delta\log$ SFR, or $\Delta\log M_{\rm H\,I}$), the color parameters show weaker correlations with $S_{\rm tid}$, especially the global $g - r$. Nevertheless, $(g-r)_{R_{50}}$ still shows significant partial correlation in most cases.

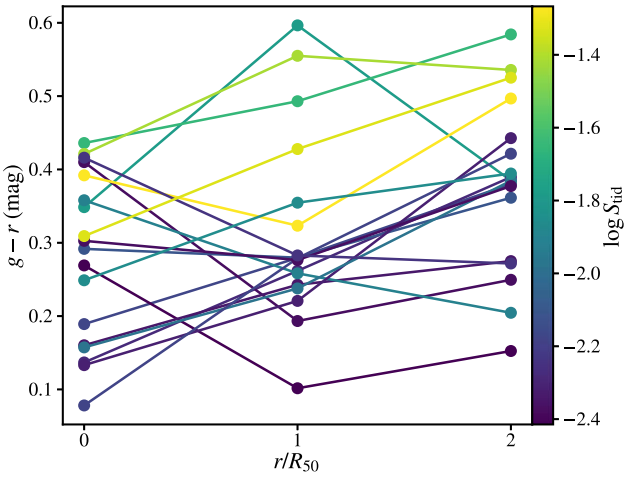

Figure 8. A reillustration of Figures 7(b)–(d). The $g - r$ color of H I-detected low-mass galaxies is plotted against the position of color measurement, color-coded by the tidal strength $S_{\rm tid}$.

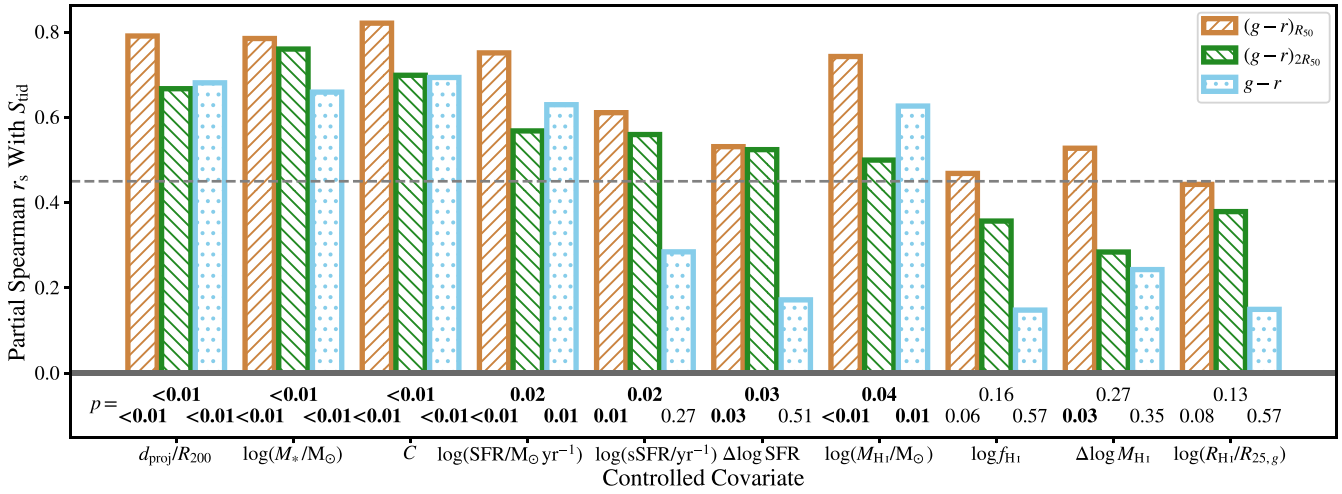

Figure 9. Partial Spearman correlation coefficients r_s for three $g-r$–S_{tid} relations given in Figure 7. Orange slashed, green backslashed, and blue dotted bars correspond to the relation at R_{50}, at $2R_{50}$, and of the whole galaxy, respectively. The controlled covariates are labeled along the x-axis. Only low-mass TS galaxies, i.e., colored symbols in Figure 7, are used. All of them have confident $M_{H\,I}$ and SFR measurements. The p-values of these partial correlations are listed at the bottom of the figure, boldfaced ones smaller than 0.05. The threshold for strong correlation, $|r_s| = 0.45$, is drawn as a gray dashed line.

These results indicate that tidal effects possibly affect the global color indirectly, through changing the global H I richness ($f_{H\,I}$ or $\Delta\log M_{H\,I}$), while the change in global color reflects a change in the integral star-forming status ($\Delta\log$ SFR or sSFR). It seems, however, that the localized colors, especially at R_{50}, are affected in more direct ways, possibly by causing gas-inflows or changing the localized star formation conditions.

6.2.2. Comparison with Trends in the Eridanus Group

A similar study (Wang et al. 2022) conducted for low-mass galaxies in the Eridanus group found the reddening of $g-r$ with S_{tid} to be most prominent in the central region, and less significant at or beyond R_{50}, contrary to our findings in the N4636G. Such a difference between the reddening patterns of these two groups indicates that the replenishment of star-forming gas near galaxy centers should be either suppressed in the Eridanus group or enhanced in the N4636G.

It is known that unperturbed dwarf irregular galaxies tend to show positive color gradients ("blue cores"; e.g., Zhang et al. 2012). Such a pattern is possibly maintained by fountain-driven gas-inflow (Elmegreen et al. 2014), or the higher star formation efficiency (SFE) at the galactic center (Bacchini et al. 2020). In groups, fountain-driven gas-inflow may be suppressed by the RPS of the circumgalactic medium (CGM; Bustard et al. 2018); also, gas affected by tidal interactions may have a high level of turbulence, which can suppress the star formation (Jeans 1902; Bolatto et al. 2011).

These effects may explain why Eridanus galaxies failed to maintain blue cores when they started to redden. The question then becomes how N4636G galaxies, while undergoing global reddening, manage to better replenish their inner disks with gas than Eridanus galaxies do.

Closely comparing two groups, we find that their ranges of S_{tid} are similar, but N4636G galaxies are systematically H I-richer. The median $\Delta\log M_{H\,I}$ of H I-detected galaxies in N4636G (-0.11 dex) is significantly higher than that in Eridanus (-0.34 dex), and there are more H I-detected galaxies in N4636G (43%) above the $M_{H\,I}$–M_* relation than in Eridanus (17%; For et al 2021; Wang et al. 2022). This difference may explain the different reddening patterns. Aside from its tidal-stripping effect, galaxy interactions are a major factor responsible for gas-inflows in galaxies at low redshift, which is more efficient in gas-rich environments, i.e., when the neighbors are gas-rich (Blumenthal & Barnes 2018; Moon et al. 2019). This is because the extended H I disks are more likely to encounter each other and/or interact with the CGM, which cause shocks and ram pressure compression (Moon et al. 2019). As a result, massive gaseous clumps are likely to form in the outer disks, which impose torques and drive inflows and/or migrate radially inward as a result of dynamic friction (Blumenthal & Barnes 2018). Thus, the N4636G galaxies, which on average have more H I-rich neighbors than the Eridanus ones do, have more efficient tidally driven gas-inflows, being more likely to retain blue cores.

As to why Eridanus galaxies are on average more H I-poor than N4636G galaxies, the reason might be in the different dynamic status of the two groups. In the middle of a major merger with another two groups, the Eridanus group has a spatial extent that is $\sim$2.5 times[28] larger than expected for its velocity dispersion (Brough et al. 2006). It indicates that its member galaxies used to be much closer to each other in the past than in the currently observed snapshot. The tidal interaction in the past might also be much stronger than that indicated by the current S_{tid}, which has efficiently accelerated the removal and consumption of the H I. This indicates that, aside from the virial mass, the dynamic status of groups also plays a role in determining the current properties of the galaxies within.

6.3. Additional Influence of Ram Pressure on Color

We searched for signatures of color reddening as a result of RPS. We conducted a similar analysis as in Section 6.2 for RPS, but do not find significant trends. The reason for this is possibly that removing outlying H I by RPS does not significantly affect star formation in the optical disk (Cortese

[28] Here we compare the maximum radial extents of the Eridanus group and of the NGC 1332 group reported by Brough et al. (2006). They have similar R_{500} deduced from respective velocity dispersion.

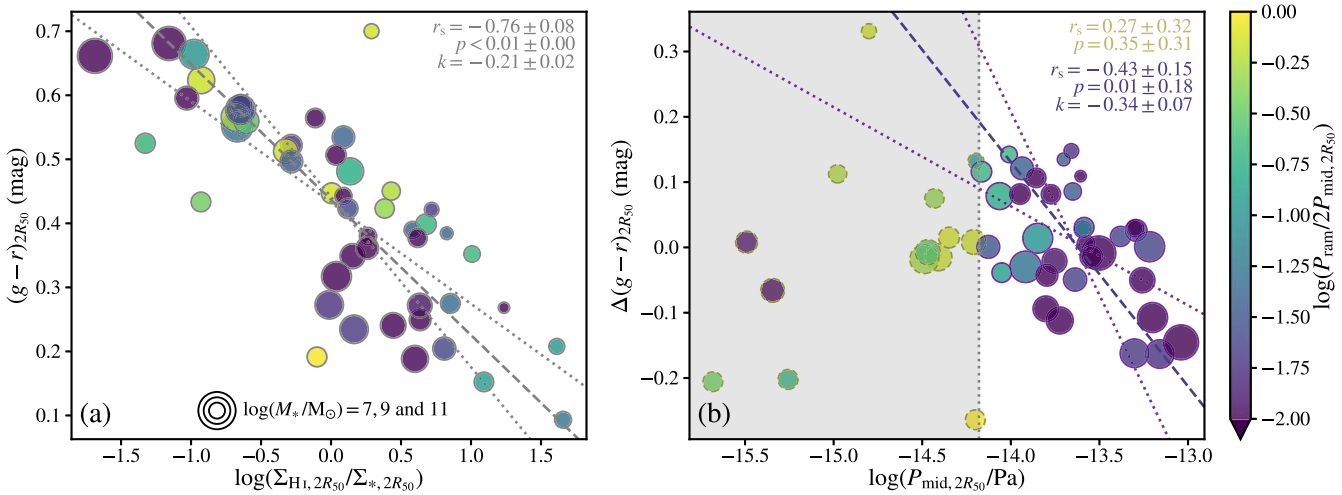

Figure 10. Additional effects of ram pressure $P_{\rm ram}$ on the $g-r$ color at $2R_{50}$. Only galaxies whose predicted H I-disk sizes satisfy $1.5R_{\rm H\,I} > 2R_{50}$ are plotted, color-coded by the importance of $P_{\rm ram}$ to the midplane gas pressure at $2R_{50}$, i.e., $P_{\rm mid,2R_{50}}$. The size of the circles represents stellar mass. (a) The relation between the $g-r$ color at $2R_{50}$ and the ratio of H I mass density to stellar mass density at $2R_{50}$. The bisector linear fitting result is plotted, and the slope is provided. The Spearman rank correlation and p-value of the relation are given with bootstrapped uncertainty. (b) The deviation of $(g-r)_{2R_{50}}$ from the fitted relation in panel (a) vs. $P_{\rm mid,2R_{50}}$. A threshold of log ($P_{\rm mid,2R_{50}}$/Pa) (-14.18, vertical dotted gray line) is chosen to let samples above it have the strongest correlation. The Spearman correlation coefficient and the bisector fitting are given in dark purple. The correlation of galaxies below the threshold is listed in yellow.

et al. 2021), at least not as much as by tidal interaction as suggested by our results.

On the other hand, we also searched for signatures of excess blue colors (indicating star formation enhancement) induced by ram pressure. The conversion efficiency of H I to the molecular gas, thus the SFE for H I gas, is reported to be related with the local midplane interstellar pressure (Wong & Blitz 2002; Leroy et al. 2008; Ostriker et al. 2010). It is suggested that ram pressure might increase this midplane pressure and, as a result, boost star formation (e.g., Poggianti et al. 2016; Mok et al. 2017; Vulcani et al. 2018a, 2020). Although there are also observations against this (e.g., Vollmer et al. 2012), several recent studies found enhanced molecular gas fractions in RPS galaxies in clusters (e.g., Cramer et al. 2020, 2021; Moretti et al. 2020; Roberts et al. 2022).

To verify this idea, we use the formula below (Ostriker et al. 2010) to calculate the midplane gas pressure:

$$P_{\rm mid} = \frac{1}{2}P_{\rm ram} + \pi G\left(\Sigma_* + \frac{1}{2}\Sigma_{\rm gas}\right)\Sigma_{\rm gas}, \quad (8)$$

assuming that ram pressure is exerted on one side of the disk, which gives rise to the first 1/2 factor. Here Σ_* and $\Sigma_{\rm gas}$ are the deprojected stellar and cold-gas surface density, respectively. Their derivations are described in Appendix E. Equation (8) implies that $P_{\rm mid}$ also depends on the local baryonic surface density, and the increase of $P_{\rm mid}$ caused by $P_{\rm ram}$ would therefore be more significant on the periphery. We thus focus on the $P_{\rm mid}$ and $g-r$ color at $2R_{50}$, the latter as an indicator of local long-term sSFR.

The localized $g-r$ color as a proxy for sSFR is naturally correlated with the localized gas fraction (Wang et al. 2020a). It is thus necessary to control for the effect of $\Sigma_{\rm H\,I}/\Sigma_*$ before investigating any further dependence of $g-r$ on $P_{\rm ram}$. In Figure 10(a), we fitted the relation between $(g-r)_{2R_{50}}$ and log ($\Sigma_{\rm H\,I,2R_{50}}/\Sigma_{*,2R_{50}}$), which is tight. The role of $P_{\rm ram}$ would then reflect in the *color offset* from this relation, $\Delta(g-r)_{2R_{50}}$. Figure 10(b) shows the relation between it and the midplane pressure. The points are color-coded by log($P_{\rm ram}/2P_{\rm mid,2R_{50}}$), i.e., the fraction of the $P_{\rm ram}$ contribution in $P_{\rm mid}$ (factor 1/2 is included due to Equation (8)).

For galaxies with a $P_{\rm mid,2R_{50}}$ larger than the threshold of $10^{-14.18}$ Pa, the color offset and the midplane pressure show a significant negative Spearman correlation. This anticorrelation does not strongly depend on the threshold. Thresholds ranging from $10^{-14.2}$ to $10^{-13.8}$ Pa mostly give p-values below 0.05, and $10^{-14.18}$ Pa gives the lowest p-value. For these galaxies, $P_{\rm ram}/2$ comprises at most 25% of the whole $P_{\rm mid}$. Therefore, although there truly is a regulation of star formation by the midplane pressure, it is hard to assess the role of $P_{\rm ram}$.

The $P_{\rm ram}$ plays a more important role in $P_{\rm mid}$ for galaxies below the threshold. However, there is no correlation between $\Delta(g-r)_{2R_{50}}$ and $P_{\rm mid}$. This might be so because the pressure-regulating mechanism requires a threshold for star formation to take place, or the star formation enhancement by ram pressure demands a certain direction of orbit and is thus rare. We also note that $g-r$ generally traces star formation on a gigayear timescale, and thus the lack of correlation could be due to the $P_{\rm ram}$-triggered star formation enhancement being too short-lived or too weak for $g-r$ to indicate. The Hα emission may provide a better tracer for star formation enhancement of this kind (X. Lin et al. 2023, in preparation). Nevertheless, we find no evidence of a statistical link between $P_{\rm ram}$ and a significant (or long-term) increase of star formation in these galaxies.

7. The Process of Gas Stripping

7.1. The Dependence of f on Galactic Properties

The strippable H I fraction f is intended to describe the instantaneous extent of stripping in an H I disk. Figure 11(b) presents the value distribution of $f_{\rm RPS}$ and $f_{\rm tid}$. The Kolmogorov–Smirnov (K-S) tests show that their spatial distribution is different. Tidal interactions can induce a larger extent of simultaneous stripping than ram pressure does. Yet, RPS is spatially more widespread than TS (see Figure 5) and as a result should not be neglected in a study of the galactic environment. Our RPS sample is actually more populated than the TS sample.

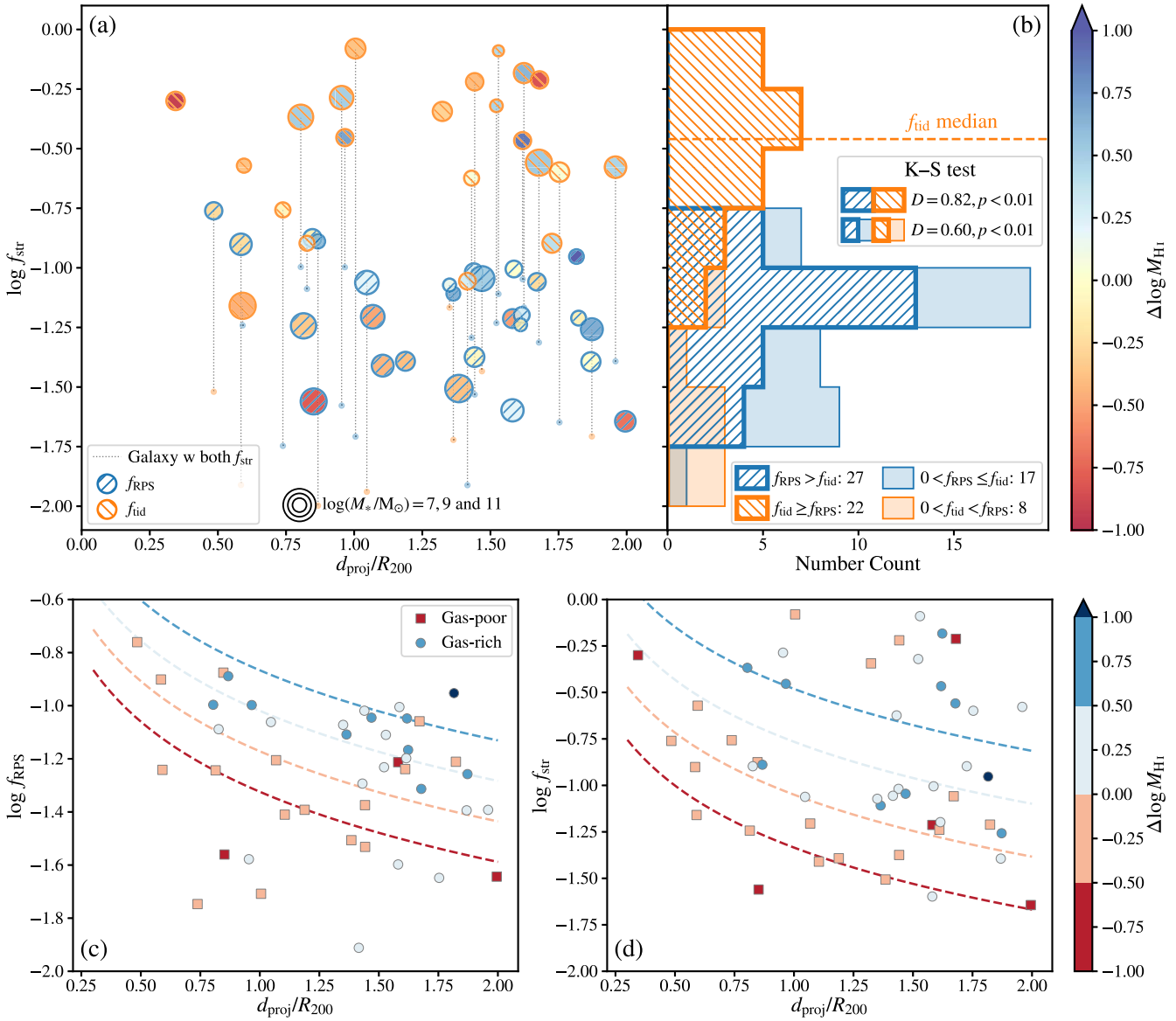

Figure 11. Comparison of the fractions of gas strippable by ram pressure (f_{RPS}) and by tidal interaction (f_{tid}). (a) How the strippable gas fraction f_{str} changes with the projected distance d_{proj} from the center of N4636G. If a galaxy has both f_{RPS} (blue-edged slashed) and f_{tid} (orange-edged backslashed) positive, the larger one is plotted as a circle, with the other plotted as a translucent dot. These two symbols are connected with a gray dotted thin line. The circle, color-coded by Δlog $M_{H\,I}$, has a radius related to the stellar mass. Thus, the blue-edged circles and orange-edged circles correspond to the RPS and TS sample, respectively. (b) Distributions of the f_{RPS} of the RPS sample (blue slashes) and the f_{tid} of the TS sample (orange backslashes). The positive f_{RPS} of the TS sample (translucent blue patch) and the positive f_{tid} of the RPS sample (translucent orange patch) are stacked as well. The results of K-S tests between f_{RPS} and f_{tid}, either limited to the RPS and TS samples or including all nonzero values, are given. An orange dashed line is drawn at the median value of f_{tid}. (c) Fitting result of f_{RPS} using Equation (10). Galaxies are divided (and color-coded) into four bins according to Δlog $M_{H\,I}$, and the four corresponding fitted lines are plotted as dashed lines of respective colors. Squares (and circles) are gas-poor (gas-rich) galaxies. (d) Fitting result of f_{str}. The symbols are the same as in panel (c).

Figure 11(a) shows f_{tid} (orange-edged backslashed) and f_{RPS} (blue-edged slashed) as a function of projected distance d_{proj}. Under the assumption that the outermost gas is most susceptible to stripping, f_{tid} and f_{RPS} cannot be added, and the larger one is dominant. So if a galaxy has both strippings ongoing, the smaller f is plotted as a dot in Figure 11(a). We take the larger one as the strippable gas fraction

$$f_{str} = \max\{f_{RPS}, f_{tid}\}. \quad (9)$$

Thus, all filled circles in Figure 11(a) are f_{str} data points.

We find that neither f_{tid} nor f_{RPS} shows a significant correlation with d_{proj}. The reason for this is likely that f further depends on the gas-richness of galaxy: a galaxy with an extended H I disk is likely to have more gas under stripping than gas-poor ones do under the same conditions. In Figure 11(a), the data points are colored by the H I richness Δlog $M_{H\,I}$, and it shows that gas-rich galaxies are generally indeed located at the region of large f and d_{proj}. We further verify this scenario by calculating the partial rank correlations and report the results in Table 1. The f_{RPS} is dependent on Δlog $M_{H\,I}$ (or d_{proj}) at a given d_{proj} (or Δlog $M_{H\,I}$), and f_{str} is dependent on Δlog $M_{H\,I}$ at a given d_{proj}. The dependence of f_{str} on d_{proj} is not that significant due to the inclusion of f_{tid}, which depends on neither parameter (consistent with the discussion in Section 5.4).

We thus conclude that with a given d_{proj}, the extent of stripping, f_{str}, increases with an increasing Δlog $M_{H\,I}$, and that f_{str} also tentatively increase toward the group center. The shape

Table 1
Partial Rank Correlations of f

Variable	$f_{\rm RPS}$	$f_{\rm tid}$	$f_{\rm str}$
$d_{\rm proj}$	−0.48; 0.01	0.10; 0.67	−0.23; 0.11
$\Delta\log M_{\rm H\,I}$	0.55; <0.01	−0.01; 0.98	0.32; 0.03

Note. The partial Spearman rank correlation coefficient r_s and the p-value are presented side-by-side, separated by a colon. The coefficient is calculated between the column and row headings; the other parameter in column "Variable" is set as the controlled covariate. For example, the r_s value of −0.48 is calculated between $f_{\rm RPS}$ and $d_{\rm proj}$ after controlling for $\Delta\log M_{\rm H\,I}$. Please refer to Figure 11.

Table 2
Fitted Parameters of Equation (10)

f	A	B	C	$\sigma_{\log f}$ (dex)
$f_{\rm RPS}$	-1.10 ± 0.04	0.31 ± 0.09	-0.88 ± 0.22	0.16
$f_{\rm str}$	-0.91 ± 0.05	0.57 ± 0.11	-1.11 ± 0.28	0.29

Note. Fitting results of $f_{\rm RPS}$ and $f_{\rm str}$ are given with uncertainty. The scatters around the best-fitting relation after excluding outliers, $\sigma_{\log f}$, are also listed. Please refer to Figures 11(c) and (d).

of this trend is largely set by the RPS, while the TS mainly contributes by systematically elevating the level of $f_{\rm str}$. We fit the relation of $f_{\rm str}$ and $f_{\rm RPS}$ as a function of $d_{\rm proj}$ and $\Delta\log M_{\rm H\,I}$,

$$\log f = A + B\Delta\log M_{\rm H\,I} + C\log\frac{d_{\rm proj}}{R_{200}}, \quad (10)$$

where A, B, and C are the fitting parameters. The fitting results for $f_{\rm RPS}$ ($f_{\rm str}$) are presented in Table 2 and are plotted in Figures 11(c) and (d). There is only one galaxy with $\Delta\log M_{\rm H\,I} = 1.62 > 1$, and we exclude it from fitting. During the fitting of $f_{\rm str}$, we further exclude six outliers with 2.25σ clipping. The final fitted relations have rather uniform scatters $\sigma_{\log f}$, which are also reported in Table 2.

7.2. Empirically Modeling the Stripping Process

7.2.1. The Motivation

A major goal of quantifying the strengths of RPS and TS is to find out how they together shape the H I distribution (and subsequently influence star formation) of satellite galaxies. In Section 6 we have already discussed the respective influences of these two environmental processes on H I gas and optical colors, while, in Section 7.1 we have shown how gas stripping is prevalent and varies throughout the group.

Correspondingly, the gas content and the star formation status of infalling star-forming galaxies may change with $d_{\rm proj}$ as well. We plot them in Figure 12, and try to model them with known information in this section. We note that we only plotted galaxies with an sSFR $> 10^{-11}\,{\rm yr}^{-1}$ in Figure 12 to better trace the recent infalling galaxies (Cortese et al. 2021). There are significant correlations (Spearman rank) between the $\Delta\log M_{\rm H\,I}$ and $d_{\rm proj}$ ($p = 0.02$) and between $\Delta\log M_{\rm H\,I}$ and $\Delta\log$ SFR ($p < 1\times10^{-13}$). The latter corroborates the link between the gas-stripping and quenching (Saintonge & Catinella 2022). If low-sSFR galaxies are included, the aforementioned correlations remain significant, and $\Delta\log$ SFR and $d_{\rm proj}$ will also show a significant correlation. For a similar diagram featuring all galaxies in the group, please refer to Appendix G.2.

The pattern of H I becoming on average more deficient toward the group center is similar to previous results for other groups and clusters (e.g., Hess & Wilcots 2013; Jaffé et al. 2015). Hereafter, we take an empirical approach that is based on both physical considerations and observations, to model the drop of $\Delta\log M_{\rm H\,I}$ with decreasing $d_{\rm proj}$. Similar approaches have been used by Vollmer (2003) to infer (based on the multiwavelength morphologies) the infall orbits of galaxies near the Virgo cluster center, by Boselli et al. (2014) to distinguish the role of RPS and strangulation in the reddening of satellites in massive clusters, and by Jaffé et al. (2015) to explain dramatically rising fraction of H I nondetections driven by RPS toward the small-distance and high-velocity region of massive clusters. Compared to these early works mostly focusing on massive clusters, our major improvements are the inclusion of TS and timescales for stripping the strippable H I ($t_{\rm str}$; also see Wang et al. 2021 for deviation of RPS timescales in an RPS-dominated environment).

7.2.2. The Empirical Model

The core part of this empirical, simple model is the decreasing rate of the H I amount during the infall process. We make use of $f_{\rm str}$ as a function of $d_{\rm proj}$ and $\Delta\log M_{\rm H\,I}$ that is fitted in Section 7.1. Combining it with $t_{\rm str}$ (the time needed for all strippable gas to be removed under the same environment), and adding a persistent gas consumption due to the star formation, leads to a simplified prescription of the decreasing rate of the $\Delta\log M_{\rm H\,I}$.

We ignore the influence of gas accretion, feedback driven outflows, and return of mass from stellar evolution. Most of these effects are related to the star formation, and they together can be viewed as a modification to the gas consumption rate due to star formation. They may be better constrained in the future when more information becomes available as the WALLABY survey progresses. We also ignore the increase of stellar mass, which will further reduce $\Delta\log M_{\rm H\,I}$, in the main part of this paper. The influence of these approximations on the main results is discussed in Appendix G.3. Additionally, previous simulations (Tonnesen & Bryan 2012; Jáchym et al. 2013; Quilis et al. 2017; Köppen et al. 2018) and observations (e.g., Cramer et al. 2021) found the falling-back of stripped gas, especially when the ram pressure is unsteady or changes abruptly, which could slow down the quenching. In this model, however, we focus on the first-time infalling of galaxies before they pass the pericenter, and thus falling-back would be less important and is ignored here.

This model additionally has the following components and assumptions.

1. *The infall starts at $2R_{200}$ and the time since then is traced by $d_{\rm proj}$.* The $d_{\rm proj}$ of infalling galaxies decreases at a constant velocity of σ_v, the 1D velocity dispersion of the group. We use the half-crossing time $T_0 = R_{200}/\sigma_v = 2.146$ Gyr as the time unit. By doing so, we have assumed radially infalling orbits for these relatively star-forming galaxies, and thus the calculation is only statistically meaningful. We also presumed that stripping is weak enough beyond $2R_{200}$, which is confirmed later.

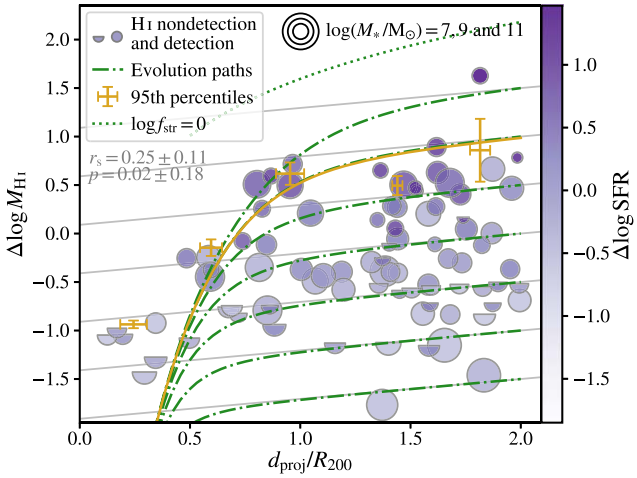

Figure 12. The evolution of galaxies' $\Delta\log M_{\rm H\,I}$ as they infall. Only galaxies with an sSFR $> 10^{-11}$ yr^{-1} are plotted in this figure. H I detections (circle) and nondetections (semicircle, plotted using the upper limit) are color-coded by $\Delta\log$ SFR. The radius of these circles and semicircles correlates with the stellar mass. The medians of $d_{\rm proj}$ and the 95th percentiles of $\Delta\log M_{\rm H\,I}$ (including H I nondetections but not low-sSFR galaxies) in five even $d_{\rm proj}$ bins are given in orange, and the uncertainties are estimated with bootstrap. Hypothetical evolutionary paths for infalling galaxies with different initial $\Delta\log M_{\rm H\,I}$ are plotted as green dashed–dotted lines. The Spearman rank correlation and the p-value are given. The galaxy pair are indicated by cyan-edged triangles. The line of $f_{\rm str} = 100\%$ is plotted as green dotted lines, above which galaxies should not appear in our model. The evolutionary path with star formation as the only gas consumption is plotted with gray lines for reference.

2. *The $t_{\rm str}$ depends only on $d_{\rm proj}$ but not on $\Delta\log M_{\rm H\,I}$.* Once H I becomes strippable, the restoring force is fully counteracted by the stripping force, and the acceleration for stripped H I to leave the galactic disk is determined by the residual stripping force fully depending on the external environmental conditions. This scenario is in concept consistent with the theoretical prediction of TS-assisted RPS and vice versa (Boselli et al. 2022). We simplistically parameterize $t_{\rm str}$ as $10^{\alpha}d^{n}T_0$ without further physical motivation, where α and n are free parameters to be derived, and $d := d_{\rm proj}/R_{200}$. We have ignored additional pushes by the stellar feedback and the clumpy or multiphase nature of gas (Kazantzidis et al. 2017).
3. *We use the most H I-rich galaxies as the reference population to fit the model.* We do this because they are least affected by the detection limit of $M_{\rm H\,I}$. Also, the most H I-rich galaxies at the outskirts are very likely to remain the most H I-rich after infalling. We thus focus on the most gas-rich galaxies at each $d_{\rm proj}$, which form the upper envelope of the data points in Figure 12. This envelope is almost horizontal beyond R_{200}, but plummets within it. We quantitatively describe this envelope with the 95th percentiles of $\Delta\log M_{\rm H\,I}$ in five even bins of $0.4R_{200}$ width, which are plotted in Figure 12 in orange. The percentiles are calculated without galaxies with sSFR $\leqslant 10^{-11}$ yr^{-1}, and the result including them can be found in Appendix G.3. The choice of bin edges alleviates the influence of the gap at $\sim$1.25R_{200}, possibly linked with the second turnaround radius of groups (Shandarin & Zeldovich 1989; Tully 2015).
4. *Galaxies have a uniform SFE of* 0.22 Gyr^{-1} (Saintonge et al. 2017). This corresponds to an intrinsic slope of $0.205/R_{200}$ on the $\Delta\log M_{\rm H\,I}$–$d_{\rm proj}$ diagram (gray lines in Figure 12). We note that the SFE of star-forming galaxies significantly decreases toward low M_* (Huang et al. 2012). This effect actually cancels out and mitigates the systematic bias caused by the assumption of holding M_* constant (see Appendix G.3).

With all of these assumptions, the empirical model is described by the following differential equation:

$$\frac{{\rm d}\Delta\log M_{\rm H\,I}}{{\rm d}d} = \frac{\log[1/(1-f_{\rm str})]}{t_{\rm str}/T_0} + 0.205, \qquad (11)$$

where $1 - f_{\rm str}$ is the fraction of remaining gas, and where $f_{\rm str}$ is calculated using Equation (10).

7.3. The Stripping Timescale

Equation (11) can be solved as an initial value problem numerically with given parameters α, n, and T_0. We use the Python package *emcee* (Foreman-Mackey et al. 2013) to fit these three parameters with Markov Chain Monte Carlo (MCMC) methods, the details of which are reported in Appendix G.1.

The median values of two parameters with a 1σ confidence interval are $\alpha = -0.88^{+0.54}_{-0.25}$ and $n = 4.1^{+5.0}_{-2.8}$, and the corresponding fitted evolutionary path is plotted as the orange solid line in Figure 12, which reproduces the gradual-then-steep feature and follows five percentile points well. We additionally plotted several evolutionary paths with different initial $\Delta\log M_{\rm H\,I}$ at $2R_{200}$ as green dashed–dotted lines. Galaxies with less gas tend to spend more time losing gas almost solely by star formation (i.e., following gray lines) and to drastically lose gas by stripping later. Within R_{200}, the evolutionary paths gradually converge, suggesting the overwhelming effect of stripping there.

Figure 13(a) plots our model of stripping timescale estimation adopting these two values and shows the corresponding 1σ scatter. At the outer region of the group, it takes several gigayears to strip all strippable gas. The timescale there could even reach the age of the universe given the large error bar. At R_{200}, $t_{\rm str}$ decreases to hundreds of megayears. It drops rapidly toward the group center, reaching a submegayear scale.

Interestingly, the range of $t_{\rm str}$ is largely consistent with that estimated by Wang et al. (2021) within R_{200} of the Hydra cluster using a different method. Different from N4636G, the dominating stripping effect in the Hydra cluster is RPS, which might be assisted by thermal evaporation (Wang et al. 2021). Compared to the Hydra cluster, N4636G is six times lower in M_{200}, resulting in a twice-as-low velocity dispersion and, on average, a four-times-lower ram pressure (Gunn & Gott 1972). N4636G also has a 3.3-times-lower ICM temperature and a 4.5-times-less-efficient thermal evaporation (Cowie & McKee 1977). While instantaneously and for individual galaxies, TS and RPS are possibly highly independent, it seems that, on a longer timescale during which the satellite is infalling and for the whole satellite population in the group, TS and RPS may work together to make stripping efficient in N4636G, as suggested by the simulations of McPartland et al. (2016).

7.4. The Depletion Timescale

With these deduced evolutionary paths of $\Delta\log M_{\rm H\,I}$, it is possible to translate them into the timescale of the depletion of gas, $t_{\rm dpl}$, since crossing the group border defined as $2R_{200}$ or as R_{200}, the radius where stripping becomes dominant.

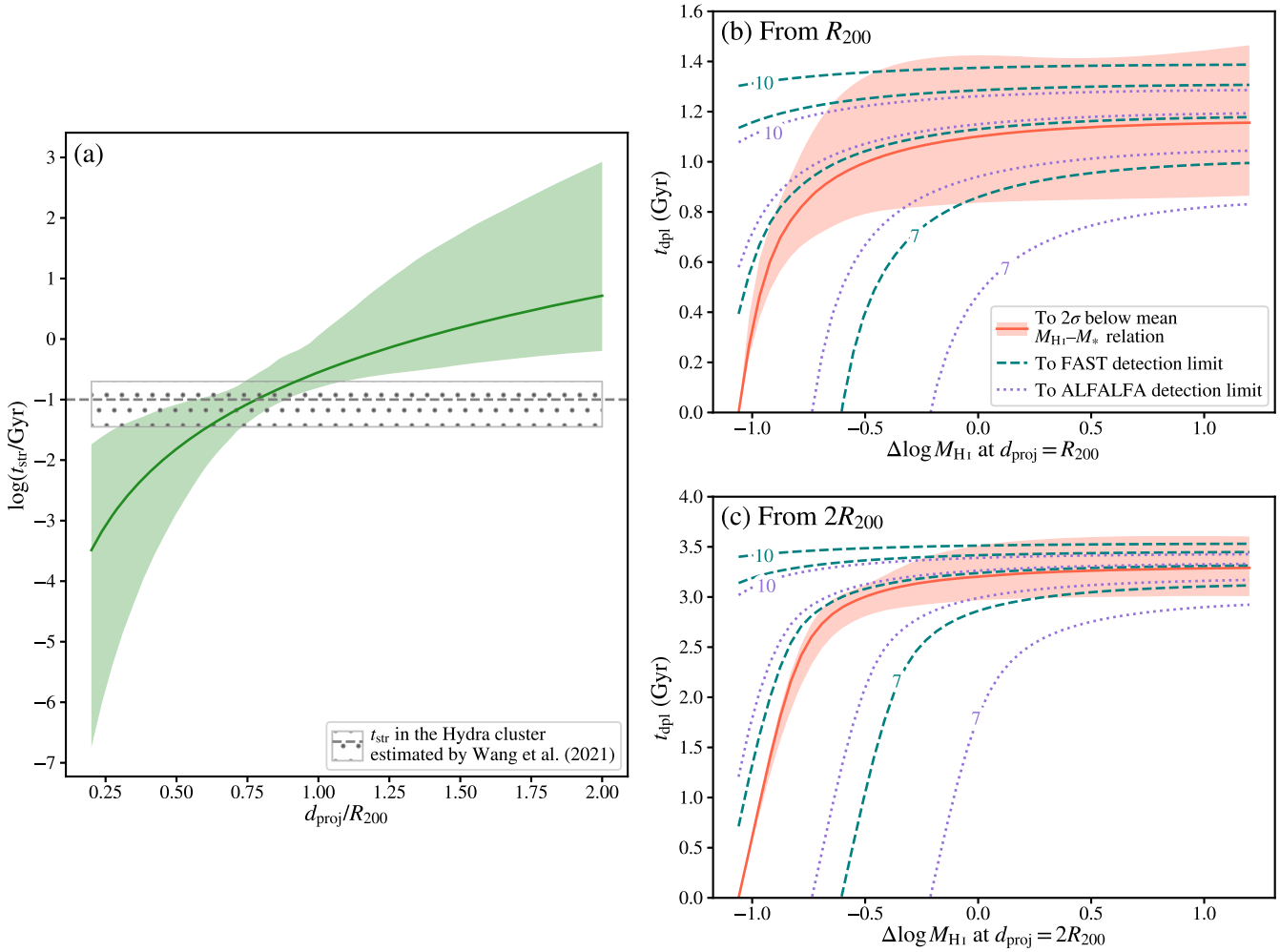

Figure 13. Model timescales of gas stripping and depletion. (a) Time needed for all strippable gas to be stripped, t_{str}, as a function of d_{proj}. To estimate the uncertainty, we use random parameters of α and n from MCMC to construct an ensemble of stripping timescales. The shading area is bordered by the 16th and 84th percentiles of the timescale distribution, indicating the 1σ uncertainty. As a reference, the t_{str} of RPS estimated by Wang et al. (2021) is plotted. The median value is the dashed gray line, and the 16th and 84th percentiles are given as gray dotted shadings. (b) Duration of galaxies becoming gas poor, t_{dpl}, vs. the initial $\Delta\log M_{H\,I}$ at $d_{proj} = R_{200}$. With different definitions of *gas poor* and different stellar mass, the relation is different. Red solid, green dashed, and purple dotted lines give the time for galaxies to reach 2σ (1.06 dex) below the mean $M_{H\,I}$ relation, FAST detection limit, and ALFALFA detection limit, respectively. For the latter two, the results for galaxies with $\log(M_*/M_\odot)$ of 7, 8, 9, and 10 are different. A galaxy with a higher stellar mass has a longer depletion time. The uncertainty of the red solid line is given in shading and is obtained similarly as the uncertainty in panel (a). Panel (c) is similar to panel (b), but the starting time is when $d_{proj} = 2R_{200}$. The abscissa is the value there, too.

We first use a more controlled definition of the t_{dpl}: the time needed to drop to two times the scattering below the mean $M_{H\,I}$–M_* relation, i.e., 2×0.53 dex. With our simple model of infalling and this definition of t_{dpl}, t_{dpl} is independent of the stellar mass and is only a function of the initial $\Delta\log M_{H\,I}$. The red solid lines in Figures 13(b) and (c) show these depletion timescales since crossing R_{200} and $2R_{200}$ and their scatter, respectively. All galaxies with an initial $\Delta\log M_{H\,I}$ larger than -0.5 dex have long and similar timescales of $\sim$1 and $\sim$3 Gyr. We note that this $\sim$2 Gyr difference between the R_{200} and $2R_{200}$ values is similar to T_0, the crossing time of one R_{200}, indicating that the stripping is mild beyond R_{200}. The t_{dpl} of galaxies with less gas drops significantly.

If we define depletion from a more observational point of view as being H I nondetectable, the story will be quite different. The H I detection limit hinges on the stellar mass, and for galaxies with lower M_*, the threshold is higher relative to the mean $M_{H\,I}$ relation, resulting in a shorter t_{dpl}. Figure 13(b) gives the t_{dpl} relations of different stellar masses detected by ALFALFA (purple dotted) and by FAST (green dashed). Galaxies of low stellar mass become H I-nondetected much quicker than those of high M_* do, and the dependence of M_* is more obvious for initially gas-poor galaxies. Meanwhile, the galaxies with a stellar mass of $10^{10}\,M_\odot$ retain a t_{dpl} of $\sim$1.2 Gyr even when their initial $\Delta\log M_{H\,I}$ is as low as -1.0. A similar discussion applies to the $2R_{200}$ results shown in Figure 13(c).

In summary, it takes $\sim$1 Gyr to deplete the galactic H I (to 2σ below the mean $M_{H\,I}$–M_* relation) since galaxies enter R_{200}, within which stripping dominates. If we start the clock at $2R_{200}$ instead, the depletion time is largely uniform around 3 Gyr for H I-rich galaxies, but for H I poor galaxies, it shortens dramatically depending on the starting $\Delta\log M_{H\,I}$. This result is highly consistent with t_{dpl} of group galaxies in the literature (e.g., Wetzel et al. 2013; Haines et al. 2015; Jones et al. 2019; Rhee et al. 2020; Cortese et al. 2021; Loni et al. 2021; Oman et al. 2021; Morokuma-Matsui et al. 2022).

The new aspect of the analysis here is that we use a relatively observational perspective to separate the effect of different physical mechanisms (RPS, TS, and star formation), which may lead to gas depletion in group environments. We quantify

the combined stripping effect of RPS and TS (with $f_{\rm str}$ and $t_{\rm str}$) by adding them up after characterizing each of them, instead of using the more conventional way of inferring them as a whole from a mixed consequence (e.g., by quantifying $\Delta\log M_{\rm H\,I}$ as a function of local density or dark matter halo mass). The $t_{\rm str}$ we derived and its trend with $d_{\rm proj}$ provides a new observational constraint, which may be useful to break degeneracies in more theoretically oriented models. The $t_{\rm str}$ combines the effect of RPS and TS, but the relative role of each has been separated and addressed in Sections 5.4 and 7.1, based on which it is decided that $t_{\rm str}$ is sufficient to capture the combined effect.

The experiment above also suggests that studying the environmental effects on galactic H I is sensitive to the definition of H I depletion other than using $\Delta\log M_{\rm H\,I}$, and the depth of H I data. A secondary dependence on M_* and other parameters may be introduced by those definitions. Studies of the comparison of environmentally driven galactic H I depletion between studies should be done with caution. We also again stress that here only the first-time infalling of galaxies into the group is considered.

8. Summary and Conclusion

In this paper, we have developed a method to quantify the strength of TS and RPS using two types of parameters: S and f. The S parameter describes the instantaneous strength of these effect at the optical-disk edges, while the f parameter describes the radial extent of H I affected by each of these effects. We investigate the response of satellite galaxies to these two effects, make a phenomenon-based simple prescription of gas stripping to trace the change of $M_{\rm H\,I}$, and estimate the timescale of gas stripping and depletion as galaxies infall in the N4636G. We summarize our major results as follows.

First and most importantly, we provide a promising method to separate the effects of RPS and TS on galaxies in N4636G. This is supported by the following results:

1. RPS and TS coexist in the group but do not grow simultaneously. The RPS and TS affect 72% and 49% of H I-detected nonmerging satellite population, respectively, and 41% of the satellites are undergoing both strippings. Among these satellites, 44% (36%) are mainly influenced by RPS (TS). The values of S of the two kinds of stripping effects are independent, while the values of f of two effects are moderately anticorrelated for the same galaxy. The $f_{\rm RPS}$ increases toward the group center and in more gas-rich galaxies, while $f_{\rm tid}$ does not show similar relations. In N4636G, TS generally reaches a higher S and f than RPS does.
2. The RPS (TS) sample shows a clearer correlation between $R_{\rm H\,I}/R_{25,g}$ and $S_{\rm RPS}$ ($S_{\rm tid}$) than the remaining galaxies.
3. The low-mass ($M_* < 10^9\,M_\odot$) subset of the TS sample shows significant trends of optical color (throughout the disks, at R_{50}, and at $2R_{50}$) reddening with stronger $S_{\rm tid}$, while the remaining low-mass galaxies of the group do not.

On the separate and cooperative role of TS and RPS in driving galaxy evolution, we find the following:

1. The H I disks respond to RPS and TS similarly, by shrinking, but the reddening of the low-mass optical disks does not. For relatively H I-poor galaxies, the H I-to-optical-disk size ratio shows anticorrelations with S of both environmental effects. The low-mass TS galaxies show a reddening across the galaxy with the increase of $S_{\rm tid}$, but the increase of $S_{\rm RPS}$ has no similar effect on either all galaxies or the RPS ones.
2. The average stripping timescale well characterizes the strengthening process of RPS and TS when galaxies infall from beyond the virial radius to near the group center. It drops from nearly the Hubble time when galaxies are at $2R_{200}$ to less than 1 Gyr at R_{200}, and then less than 100 Myr at $0.5R_{200}$. As a result, active stripping and passive strangulation are the more dominant mechanisms to deplete the H I when galaxies are within and beyond R_{200}, respectively. Galaxies experience a first slow (timescale $\sim$3 Gyr) and then fast H I depletion after crossing $2R_{200}$ and $\sim 0.5R_{200}$, respectively, qualitatively consistent with the conclusion of many previous studies (e.g., Haines et al. 2015).

Comparing the TS and RPS effects in N4636G with those in more extreme environments, we find the following:

1. Compared to the more TS-dominated Eridanus supergroup, the trend of H I disks shrinking in response to TS is similar, but the pattern of reddening in low-mass optical disks is not. While the low-mass optical disks in the Eridanus supergroup redden inside out (Wang et al. 2022), those in the N4636G redden throughout the disks rather uniformly.
2. Compared to the more RPS-dominated Hydra cluster (Wang et al. 2021), there are fewer f values reaching unity, but the time needed to strip the strippable H I of galaxies within R_{200} is similar. The efficient stripping suggests the cooperative effect of RPS and TS on stripping the galaxies in N4636G.
3. In contrast to some previous findings in jellyfish galaxies under strong RPS (e.g., McPartland et al. 2016; Jaffé et al. 2018; Ruggiero et al. 2019), we do not find evidence for enhanced star formation (i.e., being bluer than expected) in RPS-affected galaxies using the $g-r$ color as the tracer.

Putting these results together, our efforts to disentangle RPS and TS are reflected in different behaviors of H I-disk shrinking and color reddening when either dominates the galaxy or the whole group. The different effects and weights of RPS and TS in different groups raise caution on the conventional operation to blindly stack satellites by the normalized projected distance or PSD of corresponding groups. On the other hand, the consistent behavior of H I decreasing with both types of S and in different groups enables the possibility of empirically combining these two effects, and supports our derivation of $f_{\rm str}$.

Despite the encouraging results, we must keep in mind the possible uncertainty of using a median $\Sigma_{\rm H\,I}$ profile when deriving the stripping strengths (S) and extents (f). We must also be cautious about the limited statistics (e.g., data points are sparse close to $S_{\rm tid,crit}$) and related large uncertainties throughout the analyses. The method of deriving $t_{\rm str}$ relies on simple assumptions, including effectively assuming that the gas accretion, outflow, and stellar mass loss cancel out and disappear in the term of SFE. These aspects should be

improved when more data come in from FAST and the main survey of WALLABY (Koribalski et al. 2020) and when comparable hydrodynamic simulation mocks are analyzed in a similar observational way.

Our H I sample has combined both interferometric and single-dish surveys to achieve a full group coverage as well as to exploit the advantage of each. While some results (e.g., the upper envelope of the $\Delta\log M_{\rm H\,I}$–$d_{\rm proj}$ relation; Figure 12) benefit from the capability of FAST to detect a wide dynamic range in $\Delta\log M_{\rm H\,I}$, the basis of the analysis (i.e., deriving f and S based on a uniform shape of H I profile) is supported by the consistent H I size–mass relation of the few galaxies with resolved WALLABY images in this group. The deviation of $f_{\rm RPS}$ and $S_{\rm tid}$ was also calibrated and tested using resolved images from WALLABY in pilot studies (Wang et al. 2021, 2022). When more complexities of galaxy evolution are studied in the future, the cooperation of the two types of data in a similar manner will continue to be powerful.

Acknowledgments

We thank the anonymous referee for providing constructive and helpful comments. J.W. acknowledges research grants from Ministry of Science and Technology of the People's Republic of China (No. 2022YFA1602902) and the National Science Foundation of China (No. 12073002). B.L. acknowledges the support from the Korea Astronomy and Space Science Institute grant funded by the Korea government (MSIT; Project No. 2022-1-840-05). P.K. acknowledges financial support by the German Federal Ministry of Education and Research (BMBF) Verbundforschung grant 05A20PC4 (Verbundprojekt D-MeerKAT-II). A. Bosma acknowledges support from the Centre National d'Etudes Spatiales (CNES), France. L.C.H. was supported by the National Science Foundation of China (11721303, 11991052, 12011540375, 12233001) and the China Manned Space Project (CMS-CSST-2021-A04, CMS-CSST-2021-A06). H.Y.W. is supported by NSFC No. 12192224. L.V.M. acknowledges financial support from grants CEX2021-001131-S funded by MCIN/AEI/10.13039/ 501100011033, RTI2018-096228-B-C31 and PID2021-123930OB-C21 by MCIN/AEI/10.13039/501100011033, by "ERDF A way of making Europe" and by the European Union and from IAA4SKA (R18-RT-3082) funded by the Economic Transformation, Industry, Knowledge and Universities Council of the Regional Government of Andalusia and the European Regional Development Fund from the European Union. Parts of this research were supported by High-performance Computing Platform of Peking University.

This work has used the data from the Five-hundred-meter Aperture Spherical radio Telescope (FAST). FAST is a Chinese national mega-science facility, operated by the National Astronomical Observatories of Chinese Academy of Sciences (NAOC).

The Australian SKA Pathfinder is part of the Australia Telescope National Facility, which is managed by CSIRO. Operation of ASKAP is funded by the Australian Government with support from the National Collaborative Research Infrastructure Strategy. ASKAP uses the resources of the Pawsey Supercomputing Centre. Establishment of ASKAP, the Murchison Radio-astronomy Observatory, and the Pawsey Supercomputing Centre are initiatives of the Australian Government, with support from the Government of Western Australia and the Science and Industry Endowment Fund. We acknowledge the Wajarri Yamatji people as the traditional owners of the observatory site.

Funding for the Sloan Digital Sky Survey IV has been provided by the Alfred P. Sloan Foundation, the U.S. Department of Energy office of Science, and the participating institutions.

SDSS-IV acknowledges support and resources from the Center for High Performance Computing at the University of Utah. The SDSS website is www.sdss.org.

SDSS-IV is managed by the Astrophysical Research Consortium for the Participating Institutions of the SDSS Collaboration including the Brazilian Participation Group, the Carnegie Institution for Science, Carnegie Mellon University, Center for Astrophysics—Harvard & Smithsonian, the Chilean Participation Group, the French Participation Group, Instituto de Astrofísica de Canarias, The Johns Hopkins University, Kavli Institute for the Physics and Mathematics of the Universe (IPMU)/University of Tokyo, the Korean Participation Group, Lawrence Berkeley National Laboratory, Leibniz Institut für Astrophysik Potsdam (AIP), Max-Planck-Institut für Astronomie (MPIA Heidelberg), Max-Planck-Institut für Astrophysik (MPA Garching), Max-Planck-Institut für Extraterrestrische Physik (MPE), National Astronomical Observatories of China, New Mexico State University, New York University, University of Notre Dame, Observatário Nacional/MCTI, The Ohio State University, Pennsylvania State University, Shanghai Astronomical Observatory, United Kingdom Participation Group, Universidad Nacional Autónoma de México, University of Arizona, University of Colorado Boulder, University of Oxford, University of Portsmouth, University of Utah, University of Virginia, University of Washington, University of Wisconsin, Vanderbilt University, and Yale University.

The Legacy Surveys consist of three individual and complementary projects: the Dark Energy Camera Legacy Survey (DECaLS; Proposal ID #2014B-0404; PIs: David Schlegel and Arjun Dey), the Beijing–Arizona Sky Survey (BASS; NOAO Prop. ID #2015A-0801; PIs: Zhou Xu and Xiaohui Fan), and the Mayall z-band Legacy Survey (MzLS; Prop. ID #2016A-0453; PI: Arjun Dey). DECaLS, BASS, and MzLS together include data obtained, respectively, at the Blanco telescope, Cerro Tololo Inter-American Observatory, NSF's NOIRLab; the Bok telescope, Steward Observatory, University of Arizona; and the Mayall telescope, Kitt Peak National Observatory, NOIRLab. Pipeline processing and analyses of the data were supported by NOIRLab and the Lawrence Berkeley National Laboratory (LBNL). The Legacy Surveys project is honored to be permitted to conduct astronomical research on Iolkam Du'ag (Kitt Peak), a mountain with particular significance to the Tohono O'odham Nation.

NOIRLab is operated by the Association of Universities for Research in Astronomy (AURA) under a cooperative agreement with the National Science Foundation. LBNL is managed by the Regents of the University of California under contract to the U.S. Department of Energy.

This project used data obtained with the Dark Energy Camera (DECam), which was constructed by the Dark Energy Survey (DES) collaboration. Funding for the DES Projects has been provided by the U.S. Department of Energy, the U.S. National Science Foundation, the Ministry of Science and Education of Spain, the Science and Technology Facilities Council of the United Kingdom, the Higher Education Funding Council for England, the National Center for Supercomputing

Applications at the University of Illinois at Urbana-Champaign, the Kavli Institute of Cosmological Physics at the University of Chicago, Center for Cosmology and Astro-Particle Physics at the Ohio State University, the Mitchell Institute for Fundamental Physics and Astronomy at Texas A&M University, Financiadora de Estudos e Projetos, Fundacao Carlos Chagas Filho de Amparo, Financiadora de Estudos e Projetos, Fundacao Carlos Chagas Filho de Amparo a Pesquisa do Estado do Rio de Janeiro, Conselho Nacional de Desenvolvimento Cientifico e Tecnologico and the Ministerio da Ciencia, Tecnologia e Inovacao, the Deutsche Forschungsgemeinschaft, and the collaborating institutions in the Dark Energy Survey. The collaborating institutions are Argonne National Laboratory, the University of California at Santa Cruz, the University of Cambridge, Centro de Investigaciones Energeticas, Medioambientales y Tecnologicas-Madrid, the University of Chicago, University College London, the DES-Brazil Consortium, the University of Edinburgh, the Eidgenossische Technische Hochschule (ETH) Zurich, Fermi National Accelerator Laboratory, the University of Illinois at Urbana-Champaign, the Institut de Ciencies de l'Espai (IEEC/CSIC), the Institut de Fisica d'Altes Energies, Lawrence Berkeley National Laboratory, the Ludwig Maximilians Universitat Munchen and the associated Excellence Cluster Universe, the University of Michigan, NSF's NOIRLab, the University of Nottingham, the Ohio State University, the University of Pennsylvania, the University of Portsmouth, SLAC National Accelerator Laboratory, Stanford University, the University of Sussex, and Texas A&M University.

BASS is a key project of the Telescope Access Program (TAP), which has been funded by the National Astronomical Observatories of China, the Chinese Academy of Sciences (the Strategic Priority Research Program "The Emergence of Cosmological Structures" grant No. XDB09000000), and the Special Fund for Astronomy from the Ministry of Finance. The BASS is also supported by the External Cooperation Program of Chinese Academy of Sciences (grant No. 114A11KYSB20160057), and Chinese National Natural Science Foundation (grant Nos. 12120101003 and 11433005).

The Legacy Survey team makes use of data products from the Near-Earth Object Wide-field Infrared Survey Explorer (NEOWISE), which is a project of the Jet Propulsion Laboratory/California Institute of Technology. NEOWISE is funded by the National Aeronautics and Space Administration.

The Legacy Survey's imaging of the DESI footprint is supported by the Director, office of Science, office of High Energy Physics of the U.S. Department of Energy under contract No. DE-AC02-05CH1123, by the National Energy Research Scientific Computing Center, a DOE office of Science User Facility under the same contract; and by the U.S. National Science Foundation, Division of Astronomical Sciences under contract No. AST-0950945 to NOAO.

Facilities: Arecibo, ASKAP, Blanco (DECam), FAST:500m, GALEX, IRSA, NED, Sloan, and WISE.

Software: astropy 5.1 (Astropy Collaboration et al. 2022), astroquery 0.4.2 (Ginsburg et al. 2019), numpy 1.21.4 (Harris et al. 2020), photutils 1.2.0 (Bradley et al. 2021), pingouin 0.5.1 (Vallat 2018), emcee 3.1.2 (Foreman-Mackey et al. 2013), Python 3.8.10, scipy 1.8.0 (Virtanen et al. 2020), SExtractor 2.25.0 (Bertin & Arnouts 1996), SWarp 2.41.4 (Bertin et al. 2002).

Appendix A
Escaping Velocity and Interlopers

We define the 3D escape velocity $v_{\rm esc,3D}$ as the minimum velocity required for a galaxy to escape the gravitational potential of a group. With $d_{\rm 3D}$ as the 3D group-centric distance and applying the Navarro–Frenk–White cold dark matter halo model (Navarro et al. 1996),

$$v_{\rm esc,3D} = v_{200}\sqrt{\frac{2\ln(1+xc)}{x[\ln(1+c)-c/(1+c)]}}, \tag{A1}$$

where $x = d_{\rm 3D}/R_{200}$, $v_{200} = \sqrt{GM_{200}/R_{200}}$, and the concentration c is set as 4.

Assuming equipartition and isotropy, the projected values are

$$v_{\rm esc,proj} = \frac{v_{\rm esc,3D}}{\sqrt{3}}, \quad d_{\rm proj} = \frac{\pi}{4}d_{\rm 3D}, \tag{A2}$$

respectively.

To estimate the fraction of interlopers (galaxies out of $2R_{200}$ in 3D) under our sample selection, we use simulated catalogs generated by IllustrisTNG-100 (Marinacci et al. 2018; Naiman et al. 2018; Nelson et al. 2018; Pillepich et al. 2018; Springel et al. 2018). For all simulated groups with an M_{200} within 0.3 dex around that of N4636G, we select their *members* using a similar criteria based on the projected PSD, which is introduced in Section 2.1. We find that the interloper fraction is mainly determined by the projected group-centric distance. At $1.5R_{200}$, the fraction is ∼40% and is ∼20% at R_{200}, consistent with the result of Oman & Hudson (2016). We confirm that trends introduced in Section 6 remain significant if $1.5R_{200}$ is used as the boundary to select group members.

We excluded certain interlopers using redshift-independent distances available for some of our galaxies from CF3. Four galaxies are excluded whose distances exceed $3R_{200}$ from 16.2 Mpc (N4636G's distance) after considering the uncertainty.

N4636G also has a massive neighbor cluster, Virgo, to its northwest, making galaxies and groups around it (including N4636G) experiencing gravitational acceleration and having a complex relation between the redshift and heliocentric distance (Shaya et al. 2017; Kourkchi et al. 2020). This results in unavoidable uncertainty of our sample selection. This problem is mitigated by using the equipartitioned escape velocity, instead of the maximum one, when selecting member galaxies. We further assess the significance of the problem by estimating the tidal truncation radius of N4636G as a satellite halo of the Virgo cluster following Taffoni et al. (2003), taking $2.5\times10^{14}\,M_\odot$ as the mass of the Virgo (Boselli & Gavazzi 2006). Only five out of 119 galaxies possibly have a group-centric distance larger than the truncation radius. Therefore, we concluded that the influence of Virgo is negligible.

Appendix B
Mock Test for Image-based H I Measurements Dependent on Spatial Resolution

We do simple mock tests to check the influence of spatial resolution on two kinds of measurements from the observed H I images, $R_{\rm H\,I}$ and $f_{\rm RPS}$. Based on results from these tests, we determine the criteria for selecting H I disks resolved enough for these image-based measurements. We select resolved H I galaxies to get reliable image-based measurements, using these

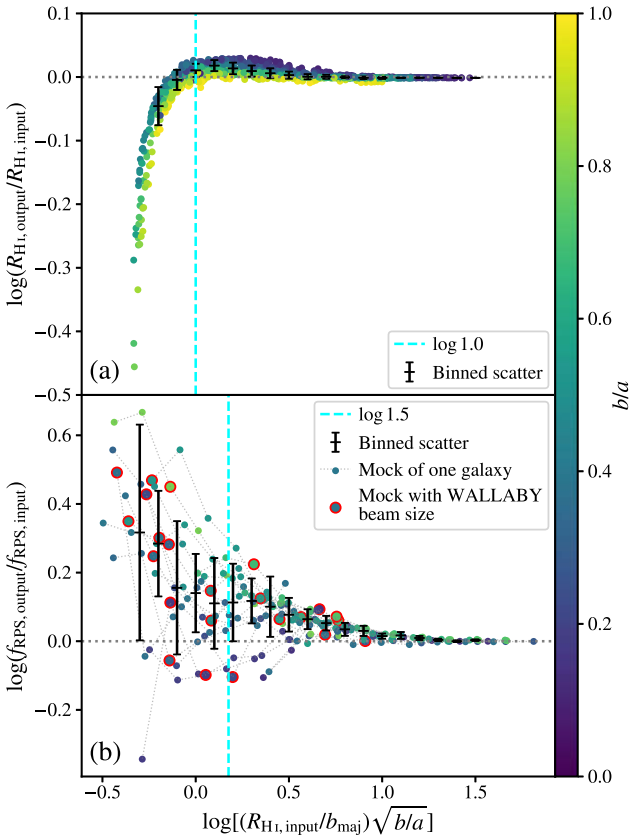

Figure 14. Results of mocking test about the influence of H I resolution on moment (0) map analysis. Mock H I images are generated assuming a surface density profile of Wang et al. (2016) and are convolved using Gaussian kernels of different FWHM, $b_{\rm maj}$. The pixel scale is one-fifth of $b_{\rm maj}$, the same as WALLABY data. The ellipticity of the projected disk is expressed as b/a, the ratio between minor-axis and major-axis, by which points are color-coded. The abscissa is equivalent to the input ratio of projected disk's area to the beam's. The criterion of disk's area being 1.5^2 times the beam's is plotted as a vertical dashed cyan line. Scatters in 0.1 dex width bins are plotted in black. (a) The ratio of $R_{\rm H\,I,output}$ measured from mock image, after correction introduced in Section 3.5, to the input $R_{\rm H\,I,input}$. The images are generated using random geometric parameters. (b) The ratio of $f_{\rm RPS}$ measured from mock image, following Wang et al. (2021), to the $f_{\rm RPS}$ directly measured using profiles. The ram pressure, disk size, and ellipticity are all true values from our H I sample, and mock $b_{\rm maj}$ ranges from 3.″75 to 60″. Results of one galaxy with different beam sizes are linked with dotted gray lines, and the results using the WALLABY beam size, 30″, have red edges.

to assess the consistency with the H I-profile-based estimations that are used in the main part of this paper.

For the test related to $R_{\rm H\,I}$, we simulate H I images of disks with different axis ratios b/a and at different spatial resolution levels ($R_{\rm H\,I}/b_{\rm maj}$). High-resolution, thin H I disks are first generated using the $R_{\rm H\,I}$ we provide as the "input" and the average surface density profile measured by Wang et al. (2020a). These disks are projected to images with different inclinations, and thus having different b/a. They are then downgraded to different resolution by convolving with Gaussian kernels of different $b_{\rm maj}$ and the pixel size is always set to be $b_{\rm maj}/5$. We then directly measure $R_{\rm H\,I}$ from the downgraded images, which are denoted as $R_{\rm H\,I,obs}$. We fix the ellipticity of annuli at the input value, instead of measuring from convolved images. We empirically correct for the beam smearing effects as $R_{\rm H\,I,output} = \sqrt{R^2_{\rm H\,I,obs} - (b_{\rm maj}/2)^2}$, following the formula in Wang et al. (2016), to obtain the final measurements $R_{\rm H\,I,output}$. We compare the input with output, and the results are shown in Figure 14(a).

The $R_{\rm H\,I,output}$ generally reproduces the value of $R_{\rm H\,I,input}$ when the projected disk has an area within $R_{\rm H\,I,input}$ larger than $b^2_{\rm maj}$ (dashed cyan line), with a small scatter and a systematic offset smaller than 5%. There are 11 out of 19 N4636G galaxies detected by WALLABY whose expected $R_{\rm H\,I,input}$ (from $M_{\rm H\,I}$) satisfies this criterion. We confirm that their image-based $R_{\rm H\,I}$'s follow the H I size–mass relation with a median offset of 0.03 dex and scatter of 0.03 dex. The positive offset mainly comes from six galaxies that are close to the $b_{\rm maj}$ criterion, consistent with the mock. We get an offset of 0.00 dex and a scatter of 0.02 dex excluding them. Because 82% of the H I-sample galaxies are either not resolved enough according to the criterion above or beyond the WALLABY footprint, we use $R_{\rm H\,I}$ estimated from the H I size–mass relation for scientific analysis in the paper.

For the test related to image-based $f_{\rm RPS}$, we set the input $f_{\rm RPS}$ (or equivalently, the ram pressure and stellar mass radial distribution) and $R_{\rm H\,I}$ based on the galaxies that have an $f_{\rm RPS} > 1\%$ from our H I sample. We produce mock images as above for the $R_{\rm H\,I}$-related test, but remove fluxes below the WALLABY depth, $10^{20}\,{\rm cm}^{-2}$. We derive image-based $f_{\rm RPS}$ by comparing the pixel values of the anchoring-force map with the ram pressure, following the procedure of Wang et al. (2021). We compare the input and output $f_{\rm RPS}$ in Figure 14(b). The input $b_{\rm maj}$ ranges from 3.″75 to 60″, and we highlight the output with the WALLABY beam size, 30″, with red circles.

We find that the image-based measurements (output) systematically overestimated the true value (input), especially when the projected disk area is small compared with the beam area. If the projected disk has an area larger than $1.5^2 b^2_{\rm maj}$ (dashed cyan line), the median relative error can be less than 25%. Only five galaxies from the WALLABY detections are resolved enough by this criterion, and their RPSs are weak ($f_{\rm RPS} < 10\%$), making the image-based method very uncertain. Due to the small number of reliable image-based measurements, we use the estimation based on median profiles for science analysis in the paper.

Appendix C
Comparison of SDSS and DECaLS Images

We compare the photometric products from the Sloan Digital Sky Survey (SDSS) and DECam Legacy Survey (DECaLS) to justify their preferred usage for high- and low-mass galaxies, respectively.

Figure 15(a) compares CG-based total fluxes from the two surveys. We have applied the correction reported by Dey et al. (2019) for the DECaLS fluxes to be calibrated against the SDSS ones. We find the following:

1. The fluxes from the two surveys are highly consistent when (SDSS) magnitudes are between 18 and 14 mag.
2. Around $\mathcal{M} = 15$ mag, there are a few galaxies for which DECaLS detects much lower flux than SDSS does. We found that these galaxies have a similar diameter to the size of the background-estimating box used by the DECaLS data processing pipeline, ∼250″. So, the large difference could be the result of oversubtracting background when the DECaLS pipeline produces the stacked images. For these galaxies that have $\mathcal{M}_{\rm DECaLS} < 14.8$ mag and $\mathcal{M}_{\rm DECaLS} - \mathcal{M}_{\rm SDSS} > 0.15$ mag, we choose to use the SDSS images for measurements.
3. For the galaxies whose $\mathcal{M} > 18$ mag, DECaLS detects more flux thanks to its better depth.

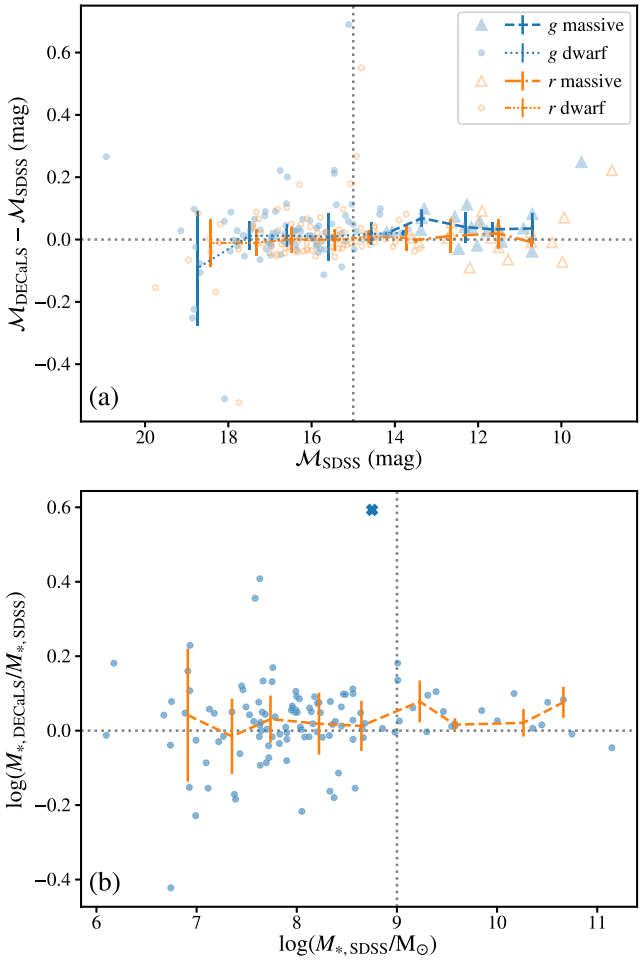

Figure 15. Comparison of the luminosities (and stellar mass M_*) from SDSS and DECaLS surveys. (a) The difference of magnitudes using images from two surveys plotted against SDSS magnitudes. Measurements are carried out using same apertures for consistency. DECaLS magnitudes are corrected following Dey et al. (2019). Individual measurements are plotted as translucent symbols. Triangles (circles) are high-mass (low-mass) galaxies, and blue (orange) points are g-band (r-band) measurements. Binned, σ-clipped median values and scatters are plotted for each of these four categories. A reference line of 15 mag is plotted. (b) The ratio of M_*'s from two surveys plotted against SDSS results and corresponding binned, σ-clipped median values and scatters. DECaLS image of #75 is of low quality and is plotted as a cross. The separation between low- and high-mass galaxies, $10^9\,M_\odot$, is plotted.

4. For the galaxies with magnitudes between 14 and 10 mag, DECaLS clearly underestimates the fluxes, especially in the g band.
5. For the brightest (and largest) galaxies with $\mathcal{M} < 10$ mag, their fluxes are significantly underestimated by DECaLS. It is possible that this is similarly due to background oversubtraction of the DECaLS pipeline.

Figure 15(b) compares the stellar mass estimated using these two surveys. We find the following:

1. The scatter of the difference increases below $10^9\,M_\odot$ from $\sim$0.07 to $\sim$0.19 dex.
2. For high-mass galaxies, although DECaLS underestimates their fluxes, DECaLS gives a higher $g-r$ value, which leads to a higher stellar mass-to-light ratio and thus a higher stellar mass.
3. Low-mass galaxies have less systematic difference but a larger scatter. Interestingly, the large difference of fluxes between the two surveys for galaxies around $\mathcal{M} = 15$ mag does not lead to an unacceptably high level of difference in stellar mass.
4. One galaxy, #75 (the cross), has a mosaicking issue in its DECaLS image, which introduces a dramatic overestimation of stellar mass. The SDSS image of this galaxy is used for photometric measurements.

Putting these together and after properly treating the few specific cases as described above, we conclude that it is reasonable to set the dividing line between using SDSS and DECaLS photometric products at $10^9\,M_\odot$.

Appendix D
The Projective Uncertainties of S and f

Assuming that the projective effects of $|\Delta v_{\rm 3D}|$ and d are the only source of uncertainties in $P_{\rm ram}$ and $S_{\rm tid}$, we use the same data as used in Appendix A, and calculate the logarithmic difference between the 3D and projected values of $|\Delta v_{\rm 3D}|$, d, $P_{\rm ram}$, and $S_{\rm tid}$. The median value and scatter, i.e., the systematic offset and random uncertainty for these parameters, are listed in Table 3. Interlopers are included in the calculation because they are included in the observations. The systematic offset of d is consistent with those reported by Wang et al. (2020b).

With our ICM model, $P_{\rm ram} \propto |\Delta v_{\rm 3D}|^2/d^{1.32}$. We find that the underestimation and projective scatter of $P_{\rm ram}$ increase significantly when $|\Delta v| < 0.5 v_\sigma$. This introduces a bias against galaxies with a small $|\Delta v|$, making our RPS sample incomplete but rather clean. We confirm that all but one of our RPS galaxies satisfy $|\Delta v| > 0.5 v_\sigma$, and thus the scatter of $P_{\rm ram}$ in this region (0.48 dex) is used in the main text.

Although $S_{\rm tid}$ is calculated for galaxy pairs, we estimate its projective effect using $1/|\Delta v_{\rm 3D}|d^2$. The scatter of the latter is 0.68 dex, almost independent of $|\Delta v|$ or $d_{\rm proj}$. We emphasize that the observed $S_{\rm tid}$ is the sum of all possible pairs, which would reduce the final logarithmic scatter. Following Wang et al. (2022; see their Figure 2), we find that the three strongest perturbers have a median contribution of 90% in total $S_{\rm tid}$. We thus use $0.68/\sqrt{3} = 0.41$ dex as the scatter. According to the theoretical definition of $S_{\rm tid}$, only the components of $v_{\rm 3D}$ that are perpendicular to the 3D d need consideration. This, however, does not change the scatter much ($S_{{\rm tid},\perp,i}$ in Table 3).

Table 3
Systematic Offset and Uncertainty from Projection

Quantity x	$\log(x_{\rm 3D}/x_{\rm proj})$		
	Median (dex)	16th and 84th Percentiles (dex)	Scatter (dex)
$\lvert\Delta v_{\rm 3D}\rvert$	0.32	$^{+0.49}_{-0.24}$	0.37
d	0.10	$^{+0.41}_{-0.10}$	0.25
$P_{\rm ram}$	0.41	$^{+0.99}_{-0.58}$	0.78
$P_{\rm ram}$ ($\lvert\Delta v\rvert > 0.5\sigma_v$)	0.13	$^{+0.44}_{-0.52}$	0.48
$S_{{\rm tid},i}$	−0.71	$^{+0.44}_{-0.92}$	0.68
$S_{{\rm tid},\perp,i}$	−0.55	$^{+0.47}_{-0.96}$	0.71

Note. The 16th and 84th percentiles are given as the value relative to the median. The scatter given in the rightmost column is half the difference between these two percentiles. The 3D and the line-of-sight velocities are denoted as $|\Delta v_{\rm 3D}|$ and $|\Delta v|$, respectively. Please refer to the text in Appendix D for more details.

We note that, although $S_{\rm RPS}$ and $S_{\rm tid}$ are systematically underestimated and overestimated, respectively, our results are not altered by it, because what matters is their relative values.[29] We do emphasize, however, that their large scatters demand that our methods be used statistically.

We further propagate the uncertainty in S and get the uncertainty of the radius of stripping boundary ($0.1R_{\rm H\,I}$ for RPS, and 0.3 dex for TS). Then, the uncertainty in $\log f$ could be calculated, which decreases strongly with an increasing f. For typical $\log f_{\rm RPS} \approx -1.25$ dex and $\log f_{\rm tid} \approx -0.5$ dex, the uncertainties are 0.25 and 0.7 dex, respectively.

Appendix E
Measurement of Strippable-gas Fraction

We provide details about estimating the strippable H I fraction here. The estimated anchoring force as a function of the radius, which is used by Wang et al. (2021), is given as Equation (5). The stellar density profile measurement is reported in Section 3.4 and $\Sigma_{\rm gas} = 1.4\Sigma_{\rm H\,I}$, where the factor 1.4 accounts for helium, and $\Sigma_{\rm H\,I}$ is the $R_{\rm H\,I}$-normalized median H I-surface-density profile of galaxies (Wang et al. 2020a) scaled with $R_{\rm H\,I}$. The H I profile is truncated at $1.5R_{\rm H\,I}$, and if the Σ_* profile is not extended enough, it is extrapolated as an exponential disk.

With Equation (5), the radius where $F_{\rm anch} = P_{\rm ram}$ can be derived. The fraction of H I beyond this radius is taken as $f_{\rm RPS}$, calculated by integrating the $\Sigma_{\rm H\,I}$ profile. If an $f_{\rm RPS}$ is smaller than 1%, we take this as unreliable, and set it to 0.

Wang et al. (2021) also calculated $f_{\rm RPS}$ using the moment (0) map for galaxies with an $R_{\rm H\,I} > 1.5b_{\rm maj}$ and found a correction factor of 1.4 for the "predicted" $f_{\rm RPS}$. In this study, we do not apply any correction factor: all five galaxies resolved enough for the moment (0) map method have $f_{\rm RPS}$ less than 10%, making the determination of a correction factor difficult. Similarly, only two resolved galaxies have $f_{\rm tid}$ larger than 10%, and no correction factor is applied to $f_{\rm tid}$.

Appendix F
Substructures in N4636G

We identified four possible substructures in N4636G by crossmatching the sample with the K&T17 catalog, and by inspecting the clustering of galaxies in the redshift map (Figure 1) and the stripping map (Figure 5(c)). The results are shown in Figure 16.

Substructure C consists of two groups, PGC1–42797 and PGC1–1242969, identified in K&T17. Substructure NE comprises three groups (PGC1–43413, PGC1–44086, and PGC1–1263098) from K&T17 plus seven other galaxies, all

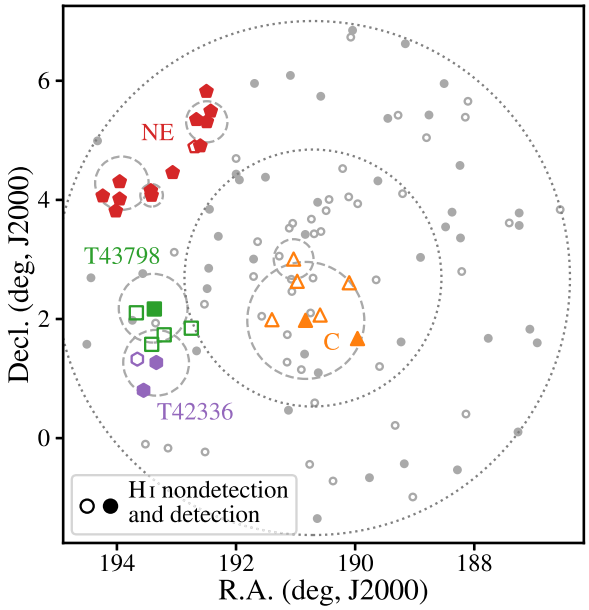

Figure 16. The substructure map. Four substructures (C, T43798, NE, T42336) are plotted in different colors and symbols and are labeled. Several groups listed in K&T17 that share galaxies with these substructures are plotted as dashed gray circles, radii of which are corresponding R_{200}'s.

of which have similar and negative heliocentric velocities relative to the center of N4636G.

We note that these identifications are of large uncertainty due to the gravitational influence of the Virgo cluster and the lack of redshift-independent distance measurements.

All substructures, apart from NE, have few H I-detected galaxies, and thus do not *contaminate* much our analysis sample in the main part of paper. Figure 17 compares the galaxies in NE with those in the same range of $d_{\rm proj}$ or in the whole group. The galaxies of NE have both their median $\Delta\log M_{\rm H\,I}$ (H I-detections only) and $\Delta\log$ SFR significantly larger than those of the two comparison samples. The differences are significant according to the K-S test probabilities. If we include H I-nondetections in the $\Delta\log M_{\rm H\,I}$ comparison, the p-values are even lower. NE, with such high SFR and H I content, could be a young and small group falling into N4636G recently.

One question is whether galaxies in these substructures (especially NE), which might have experienced significant preprocessing, follow the same relations discussed in Section 6. Figures 5(a) and (b) reveal that the galaxies in NE undergo both RPS and TS. We confirm that in Figures 7 and 10 the NE galaxies do not stand out. It is worth future investigation to determine whether such relations apply to more systems.

[29] In particular, the deviation of $S_{\rm tid,crit}$ makes $f_{\rm tid}$ insensitive to the systematic bias in $S_{\rm tid}$. We acknowledge that the absolute value of $S_{\rm RPS}$ (based on the Gunn & Gott 1972 model) is used to determine $f_{\rm RPS}$, but using $S_{\rm RPS,crit}$ to determine $f_{\rm RPS}$ does not change our major results.

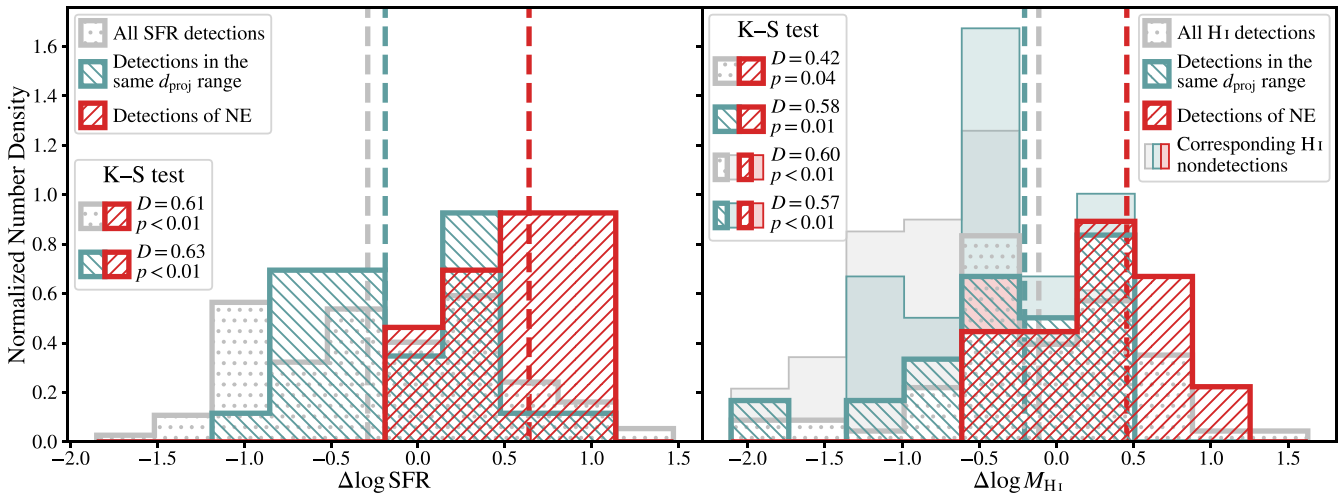

Figure 17. The galaxies in NE (red slashes) compared with galaxies in the same range of d_{proj} (dark-cyan backslashes) or in the whole sample (gray dots). The distributions of the deviations from SFMS (left) and the mean $M_{H\,I}$ relation (right) are plotted. In the left panel, two galaxies that have only lower limits of SFR are included, which makes no apparent difference to the results. In the right panel, H I nondetections are plotted as translucent patches in corresponding colors using the upper limits of $M_{H\,I}$. The median values of $\Delta \log$ SFR and H I-detected $\Delta \log M_{H\,I}$ in each sample are indicated with vertical dashed lines. The results of the K-S tests between the NE sample and the whole sample and between the NE sample and the same-d_{proj} sample are listed. For $\Delta \log M_{H\,I}$, K-S tests are also performed with H I nondetections. All distributions are normalized.

Appendix G
Models of H I Stripping

G.1. MCMC Fitting of the Model

While fitting the evolutionary path described by Equation (11), other than α and n, we also introduced parameters Y_0, the initial value of $\Delta \log M_{H\,I}$ at $d_{proj} = 2R_{200}$, and $\log f$, the factor of variance underestimation. The posterior probability distributions of all four parameters are shown in Figure 18, and the median values are reported with 1σ uncertainties. The probability-weighted values (orange lines) are similar to the corresponding median values that we used in science analyses.

We adopt such a prior probability distribution that Y_0 cannot result in a strippable gas fraction f_{str} larger than 100%. We also found that there is a second peak of posterior probability on n–α corresponding to an unphysically large α, which would result in a t_{str} much larger than the Hubble time out of R_{200} and an abrupt stripping at $\sim 0.5R_{200}$. We set the prior probability within this region as 0. The region is bordered by a blue dashed–dotted line in Figure 18.

G.2. The Uncertainty of the Fitted Evolution Path

The uncertainty of fitted α and n would be propagated into the uncertainty of the evolutionary path itself. We show the bootstrapped 1σ uncertainty as the green shading in Figure 19. The 95th percentiles of $\Delta \log M_{H\,I}$ (with sSFR $> 10^{-11}$ yr^{-1}) and the path of median parameters fitted from them are shown as orange data points and the solid green line, respectively, as references. The green shaded region covers the percentile points well.

G.3. Modified Models with Different Assumptions

We test three different modifications to our fiducial gas-stripping empirical model described in Section 7.2.2, and present the changes in t_{str} and t_{dpl} they introduce.

One modification is to use the 95th percentiles of all galaxies for MCMC fitting, instead of only those with high sSFR. In Figure 19 we show all galaxies, and their 95th percentiles are shown as narrow blue error bars. They are similar to the percentiles of high-sSFR galaxies (orange error bars), and the fitted result (dashed line) does not deviate much, except that the plummet happens nearer to the group center.

Shown in Figure 20 as dashed green lines, in this model, the t_{str} around group center is a bit longer, and the t_{dpl} increases by $\sim$150 Myr because of the delay of stripping.

Another modification is lowering the criterion of RPS from $P_{ram} = F_{anch}(r)$ to $P_{ram}/F_{anch}(r) = S_{RPS,crit}$, in the fashion of defining f_{tid}. From Figure 6 we have $S_{RPS,crit} = 10^{-0.91}$.

The change due to this modification (dashed–dotted purple lines) is shown in Figure 20. All f_{RPS}'s consistently increase to three times the original values. Correspondingly, the stripping timescale t_{str} increases by $\sim$2 dex toward the group center, where RPS is strongest, since the extent of H I disk for stripping is larger. At the outskirts, however, t_{str} decreases a bit. Because of the flatter relation of t_{str} with d_{proj} under this model, t_{dpl} shows a larger slope with respect to the initial $\Delta \log M_{H\,I}$.

The third modification considers the combined effect of SFE decreasing toward low-mass galaxies (Huang et al. 2012) and the increase of stellar mass as a function of time because of star formation. These two effects lead to the lower and higher decrease rates in $\Delta \log M_{H\,I}$, respectively, than the fiducial model would imply. The combined effect can be summarized into multiplying the slope term related to SFE by a factor of $\sim$3.

This modified model (dashed–dotted–dotted brown lines in Figure 20) does not change t_{str} much, but decreases the t_{dpl} of galaxies with a low $\Delta \log M_{H\,I}$ at R_{200}. The reason is that, for these initially gas-poor galaxies, enhanced star formation consumption quickly depletes the H I before the stripping takes over.

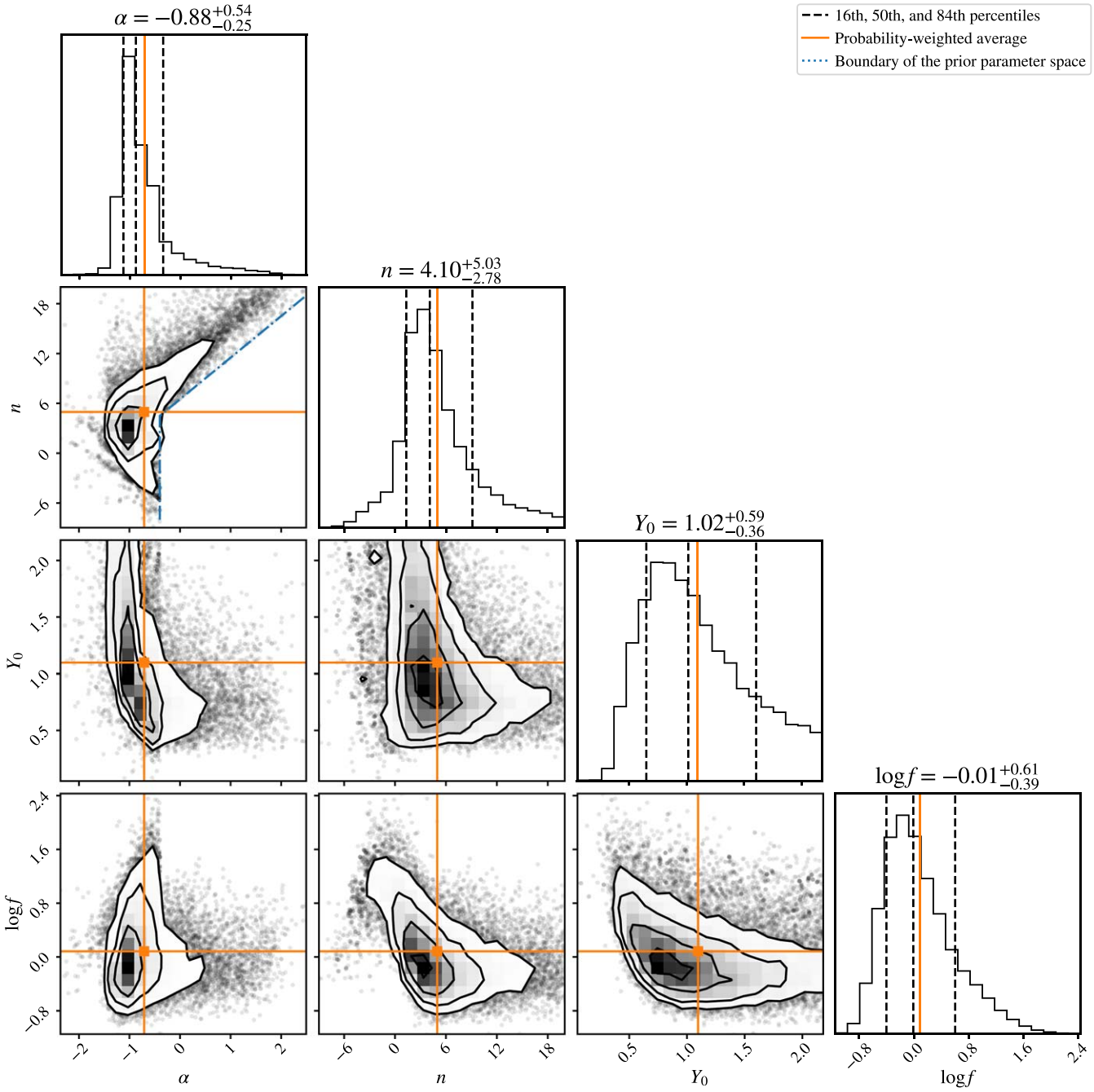

Figure 18. The posterior probability distributions of four parameters of evolutionary path model. The probability-weighted average is plotted in orange, and the 16th, 50th, and 84th percentiles are given as black dashed lines. Above each histogram, the values of three percentiles are listed. The region on the α–n plane where the prior probability is set to 0 is bordered by blue dashed–dotted line.

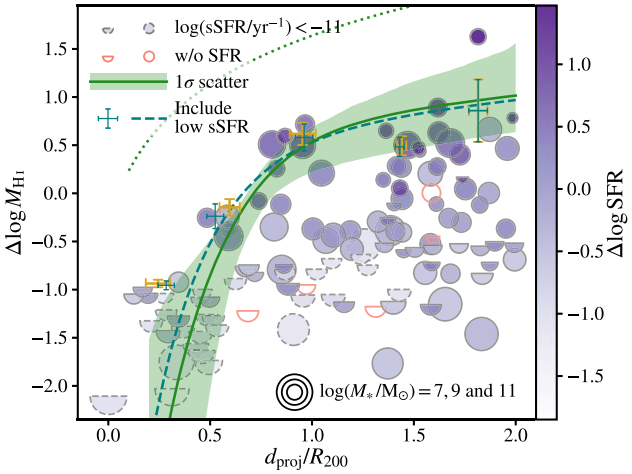

Figure 19. The uncertainty of the fitted evolutionary path, shown as the green shaded region. The meanings of circles and semicircles are the same as those in Figure 12, and symbols with dashed edges represent galaxies with $\log(\mathrm{sSFR}/\mathrm{yr}^{-1}) \leqslant -11$. Galaxies without SFR measurements are plotted as empty salmon symbols. The evolutionary path with the median values of α and n is given as a solid line. The 1σ uncertainty of the path is estimated using the bootstrap method and is plotted as as the green shaded region. The 95th percentiles and evolutionary path taking into account low-sSFR galaxies are plotted as narrow blue error bars and the dashed blue line, respectively.

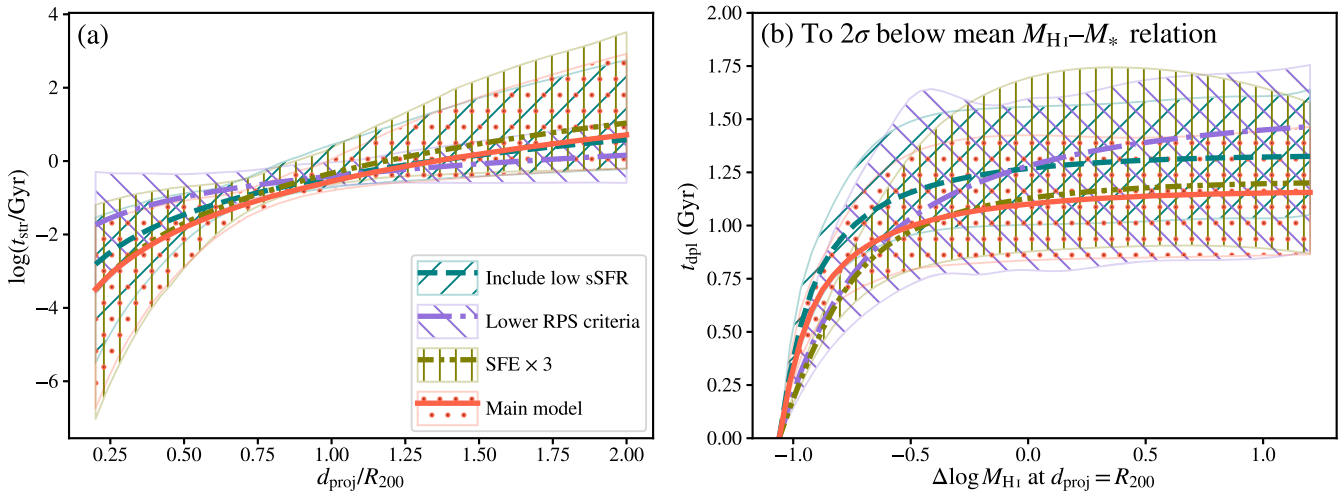

Figure 20. The influence of model specification on the values of t_{str} and t_{dpl}. Panels are similar to Figures 13(a) and (b). Four models are plotted with different line-styles and patches. The main model we used is the solid red line. For details of other three models, please refer to the text. In panel (b) the criterion of gas depletion is reaching 1.06 dex below the mean $M_{H\,I}$–M_* relation.

Appendix H
Colors of High-mass TS Galaxies

We plotted the four high-mass TS galaxies in Figure 21. Compared with low-mass ones, they do not have a very high S_{tid}. They scatter around the linear fittings we get in Section 6.2.

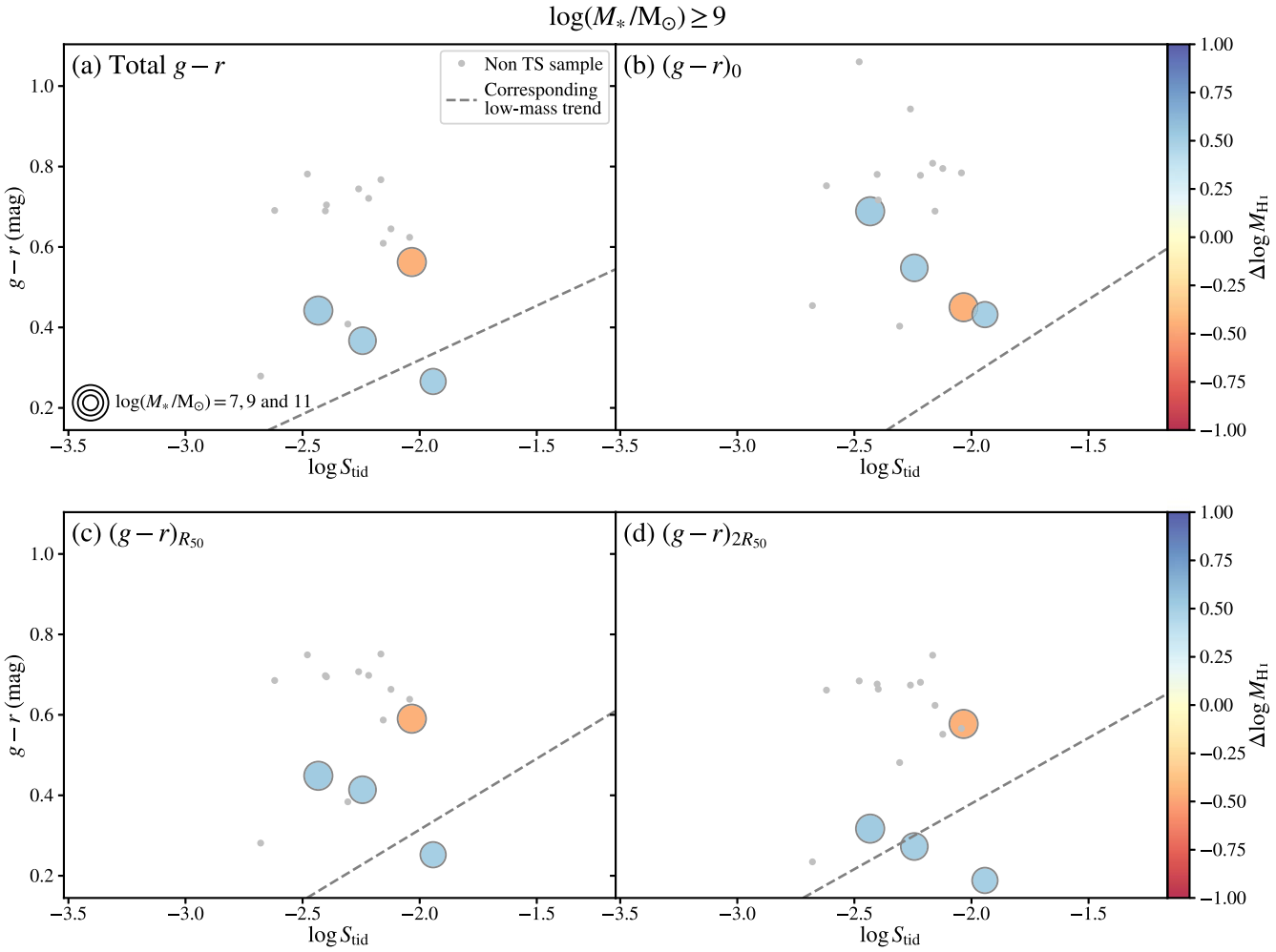

Figure 21. The same as Figure 7, but only H I-detected high-mass galaxies are plotted. The bisector fitting results of Figure 7 are plotted as references. The *x*-axis range is the same as that in Figure 7.

Appendix I
Atlas of H I-resolved Galaxies

We provide the optical images and H I-column-density maps of five galaxies resolved by WALLABY as Figure 22. Two of them (left column) are among the RPS sample, and the other three (right) belong to the TS sample. All of them have a stellar mass larger than $10^{8.5}\,M_{\odot}$, and thus the irregularity of the H I disk, if any, is less likely due to internal supernovae feedback than to external perturbations.

Both galaxies undergoing RPS have a low $f_{\rm RPS}$ (<10%), and do not show strong directional irregularities. Galaxy #67 has the largest $f_{\rm RPS}$, and shows a compressed feature in the southeast, *backward* from the group center (cyan arrow). It is possible that #67, with $d_{\rm proj} = 1.05R_{200}$ and $\Delta v = 0.93\sigma_v$, is at the backsplash stage, moving outward from the group.

Two of three TS galaxies (#23 and #78) have high values of $f_{\rm tid}$. Compared with the other three galaxies with weaker tidal interaction, a striking feature is that both galaxies have a half-ring-like H I structure in the direction of the major tidal perturber, which provides the largest portion of $S_{\rm tid}$. It is a tentative result worth future investigation when more resolved H I images are available.

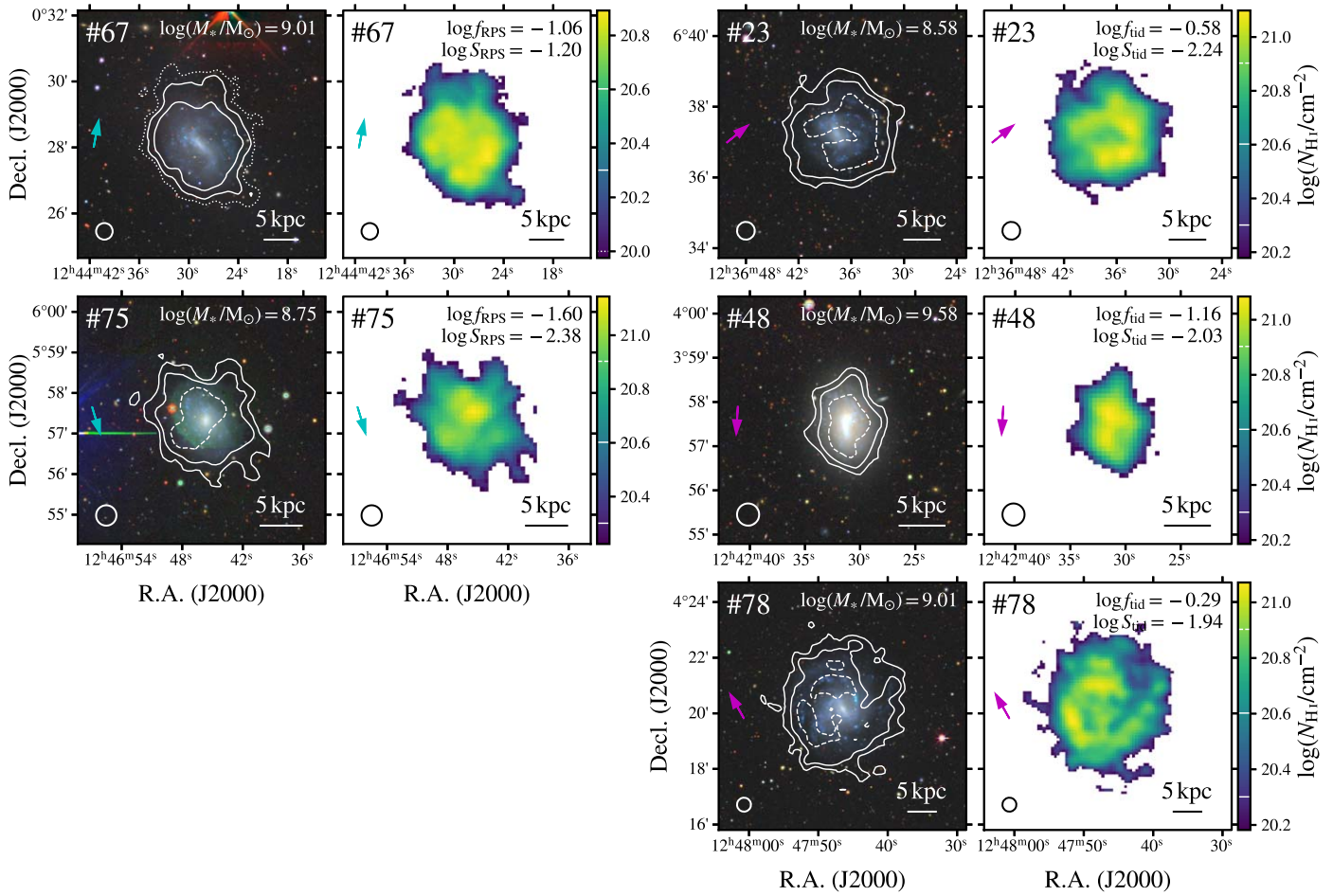

Figure 22. The atlas of five H I-resolved galaxies (see also Appendix B). RPS and TS galaxies are plotted on the left and right, respectively. For each galaxy, the DECaLS DR9 optical image and the WALLABY H I-column-density map are placed adjacently. In the H I intensity map, only pixels with values $>5\sigma$ are shown. The optical image is overlaid with the contour of $N_{\rm H\,I}$, with levels of 1, 2, 4, and 8×10^{20} cm^{-1}. The lowest and the highest level are plotted as dotted and dashed lines, respectively, for clarity. The ID, beam size ($\sim 30''$), 5 kpc scale bar, stellar mass, and the relevant values of f and S are given at each panel. The direction of the group center is indicated by a cyan arrow for RPS galaxies, with the direction of the major tidal perturber by a magenta arrow for TS ones.

Appendix J
Galaxy Properties

Basic properties and the SFR and optical measurements of our sample are listed in Table 4. H I-related measurements of our H I sample (and the merging pair) are given in Table 5.

Table 4
Galaxy Properties and Non-H I Measurements

ID	Name	R.A.	Decl.	v_{hel}	References	log SFR	Δlog SFR	SFR Note	Image Source	log P_{ram}	log S_{tid}	g	r	$g-r$ Color at Center	$g-r$ Color at R_{50}	$g-r$ Color at $2R_{50}$	log M_*	$R_{25,g}$	R_{50}	R_{90}
		(deg)	(deg)	(km s^{-1})		($M_\odot$ yr^{-1})	(dex)			(Pa)	(dex)	(mag)	(mag)	(mag)	(mag)	(mag)	($M_\odot$)	(kpc)	(kpc)	(kpc)
(1)	(2)	(3)	(4)	(5)	(6)	(7)	(8)	(9)	(10)	(11)	(12)	(13)	(14)	(15)	(16)	(17)	(18)	(19)	(20)	(21)
1	…	186.5579	3.8371	809	S	-2.68 ± 0.08	-0.07	cn	D	-15.6	-2.55	17.467 ± 0.007	16.929 ± 0.007	0.449	0.589	0.555	7.57 ± 0.15	0.726 ± 0.006	0.438 ± 0.003	1.11 ± 0.02
2	…	186.9430	1.5996	1298	A	-1.57 ± 0.08	1.47	uf	S	-14.5	-3.40	16.358 ± 0.040	16.257 ± 0.027	-0.017	0.258	0.093	7.11 ± 0.17	1.324 ± 0.050	1.815 ± 0.055	4.01 ± 0.25
3	…	187.0663	1.8288	905	A	-2.49 ± 0.09	-0.09	uf	D	-17.3	-2.54	16.297 ± 0.009	15.879 ± 0.011	0.329	0.405	0.507	7.79 ± 0.15	1.461 ± 0.005	0.759 ± 0.008	1.95 ± 0.06
4	N4457	187.2460	3.5704	885	A	-0.41 ± 0.07	-0.59	cf	S	-16.5	-2.62	10.911 ± 0.001	10.220 ± 0.001	0.752	0.685	0.662	10.51 ± 0.15	10.348 ± 0.014	2.143 ± 0.003	9.18 ± 0.03
5	…	187.2465	3.7804	825	F	-2.81 ± 0.10	-0.33	uf	D	-15.7	-1.33	16.502 ± 0.004	16.086 ± 0.006	0.309	0.428	0.525	7.70 ± 0.15	1.337 ± 0.005	0.700 ± 0.004	1.65 ± 0.03
6	…	187.2664	0.1037	1199	F	-2.48 ± 0.08	-0.63	un	S	-14.8	-3.09	15.455 ± 0.034	14.918 ± 0.012	0.311	0.506	0.535	8.37 ± 0.16	1.707 ± 0.011	1.905 ± 0.028	5.95 ± 0.20
7	…	187.4129	3.6132	1303	S	-1.97 ± 0.07	0.18	cf	D	-14.4	-1.93	15.520 ± 0.003	15.125 ± 0.003	0.409	0.361	0.417	8.05 ± 0.15	1.433 ± 0.002	0.650 ± 0.002	1.37 ± 0.01
8	…	187.7656	1.6756	1103	F	-1.79 ± 0.06	0.22	cf	D	-15.0	-2.78	15.265 ± 0.003	14.851 ± 0.007	0.350	0.390	0.535	8.20 ± 0.15	2.002 ± 0.006	1.386 ± 0.010	3.77 ± 0.07
9	…	188.1062	5.6555	1143	K	-2.84 ± 0.12	-0.29	uf	S	-15.0	-2.56	16.583 ± 0.029	16.187 ± 0.027	0.524	0.591	0.153	7.63 ± 0.16	1.053 ± 0.044	1.266 ± 0.032	3.17 ± 0.32
10	…	188.1402	0.4048	1259	K	…	…	…	D	-14.5	-1.10	18.756 ± 0.012	18.384 ± 0.011	0.617	0.368	0.125	6.71 ± 0.15	0.281 ± 0.012	0.069 ± 0.001	0.23 ± 0.01
11	…	188.1507	5.3881	894	K	-3.22 ± 0.08	-0.62	un	S	-16.8	-2.32	17.058 ± 0.030	16.592 ± 0.078	0.575	0.563	0.564	7.58 ± 0.21	1.064 ± 0.041	0.746 ± 0.065	1.81 ± 0.35
12	…	188.2108	2.7978	1041	K	-2.31 ± 0.06	-0.11	cn	D	-15.3	-2.32	16.291 ± 0.006	15.772 ± 0.004	0.523	0.535	0.562	8.00 ± 0.15	1.431 ± 0.005	0.824 ± 0.003	1.98 ± 0.02
13	…	188.2322	3.3603	739	F	-2.14 ± 0.09	0.02	uf	S	-14.9	-2.45	15.113 ± 0.016	14.805 ± 0.017	0.418	0.358	0.168	8.04 ± 0.16	1.802 ± 0.011	1.928 ± 0.043	7.25 ± 0.36
14	…	188.2417	4.5784	1228	A	-2.19 ± 0.08	0.18	un	D	-14.6	-2.61	15.770 ± 0.003	15.441 ± 0.012	0.362	0.267	0.399	7.82 ± 0.15	2.229 ± 0.006	1.558 ± 0.013	3.43 ± 0.12
15	…	188.2833	-0.5336	725	F	-2.31 ± 0.08	-0.18	un	S	-15.1	-3.15	15.457 ± 0.026	15.062 ± 0.013	0.311	0.419	0.478	8.08 ± 0.16	1.828 ± 0.016	2.759 ± 0.034	6.92 ± 0.19
16	…	188.3728	3.7939	909	F	-2.17 ± 0.08	-0.36	un	D	-17.3	-2.09	15.294 ± 0.005	14.768 ± 0.007	0.501	0.487	0.596	8.41 ± 0.15	2.554 ± 0.004	1.587 ± 0.008	3.39 ± 0.07
17	U7715	188.4818	3.5462	1135	F	-1.64 ± 0.07	-0.06	cf	D	-14.7	-2.32	14.444 ± 0.001	13.965 ± 0.004	0.436	0.432	0.560	8.66 ± 0.15	3.041 ± 0.004	1.836 ± 0.005	3.98 ± 0.04
18	…	188.5062	5.9528	648	A	-2.84 ± 0.11	0.16	uf	D	-14.8	-3.17	17.580 ± 0.013	17.217 ± 0.026	0.359	0.389	0.431	7.16 ± 0.16	0.442 ± 0.016	2.120 ± 0.042	4.48 ± 0.16
19	…	188.7605	5.4250	865	A	-2.33 ± 0.08	-0.57	cn	D	-16.1	-2.19	15.869 ± 0.003	15.209 ± 0.004	0.752	0.648	0.621	8.46 ± 0.15	2.907 ± 0.010	1.396 ± 0.005	3.30 ± 0.03
20	…	188.8023	5.0446	1001	S	-3.13 ± 0.11	0.20	cn	D	-15.7	-2.70	21.200 ± 0.040	19.590 ± 0.027	2.065	1.580	1.461	$6.80 \pm$ …[a]	0.201 ± 0.007	0.172 ± 0.004	0.36 ± 0.02
21	N4544	188.9022	3.0351	1148	F	-1.08 ± 0.07	-0.35	cf	S	-14.5	-2.40	13.377 ± 0.004	12.673 ± 0.003	0.717	0.695	0.664	9.55 ± 0.15	5.612 ± 0.025	2.027 ± 0.005	6.47 ± 0.07
22	…	189.0320	-0.9884	959	K	-2.79 ± 0.09	0.16	cf	D	-16.5	-2.81	17.758 ± 0.012	17.341 ± 0.015	0.245	0.477	0.520	7.21 ± 0.15	0.686 ± 0.006	0.432 ± 0.006	1.04 ± 0.04
23	I3576	189.1562	6.6202	1072	A	-1.52 ± 0.08	0.12	un	D	-15.4	-2.24	13.812 ± 0.001	13.492 ± 0.004	0.416	0.283	0.272	8.58 ± 0.15	4.123 ± 0.005	2.588 ± 0.009	5.91 ± 0.05
24	…	189.1755	-0.4305	1150	F	-3.25 ± 0.08	0.13	uf	D	-14.9	-3.15	18.609 ± 0.028	18.241 ± 0.030	0.138	0.395	0.547	6.76 ± 0.17	0.454 ± 0.008	0.892 ± 0.029	2.06 ± 0.13
25	…	189.2042	4.1046	832	K	-2.53 ± 0.08	-1.00	un	D	-15.4	-2.04	15.169 ± 0.005	14.529 ± 0.003	0.662	0.630	0.619	8.70 ± 0.15	1.957 ± 0.003	1.110 ± 0.003	3.11 ± 0.03
26	…	189.2290	1.6147	583	F	-2.07 ± 0.07	0.25	cn	D	-14.2	-2.69	16.061 ± 0.010	15.647 ± 0.005	0.352	0.428	0.447	7.88 ± 0.15	2.585 ± 0.009	1.420 ± 0.006	3.51 ± 0.05
27	…	189.2793	5.4216	1173	K	-2.75 ± 0.08	-1.09	un	D	-14.7	-2.02	15.565 ± 0.003	14.913 ± 0.003	0.738	0.644	0.607	8.56 ± 0.15	1.622 ± 0.003	0.690 ± 0.002	1.85 ± 0.02
28	…	189.3282	0.2134	908	K	…	…	…	D	-17.3	-2.59	16.718 ± 0.008	16.068 ± 0.009	0.616	0.624	0.632	8.10 ± 0.15	1.392 ± 0.008	0.951 ± 0.008	2.59 ± 0.10
29	N4580	189.4516	5.3684	1038	A	-0.86 ± 0.07	-0.56	cf	S	-15.4	-2.40	12.164 ± 0.005	11.475 ± 0.001	0.780	0.697	0.677	10.00 ± 0.15	6.248 ± 0.010	2.379 ± 0.002	5.39 ± 0.01
30	…	189.5905	1.2021	1198	K	-2.63 ± 0.06	0.28	cn	D	-14.4	-2.78	17.663 ± 0.007	17.241 ± 0.013	0.331	0.418	0.486	7.25 ± 0.15	0.519 ± 0.003	0.228 ± 0.002	0.57 ± 0.02
31	N4586	189.6186	4.3190	790	A	-1.30 ± 0.06	-1.16	cn	S	-15.2	-2.26	12.025 ± 0.002	11.281 ± 0.001	0.943	0.707	0.674	10.17 ± 0.15	10.118 ± 0.018	4.060 ± 0.005	10.51 ± 0.06
32	N4587	189.6476	2.6573	901	K	-2.15 ± 0.08	-1.34	un	S	-16.3	-1.99	13.294 ± 0.003	12.646 ± 0.003	0.712	0.672	0.640	9.46 ± 0.15	4.081 ± 0.023	1.213 ± 0.004	4.61 ± 0.06
33	…	189.7606	-0.6645	1140	F	-2.44 ± 0.08	0.36	un	D	-14.9	-2.95	16.855 ± 0.008	16.533 ± 0.016	0.224	0.316	0.450	7.37 ± 0.15	1.116 ± 0.019	1.523 ± 0.019	3.03 ± 0.10
34	…	189.9574	3.9356	1398	K	-2.51 ± 0.09	-0.35	uf	D	-13.7	-2.66	15.969 ± 0.002	15.490 ± 0.003	0.361	0.494	0.545	8.05 ± 0.15	1.155 ± 0.003	0.443 ± 0.001	1.24 ± 0.01
35	U7824	189.9596	1.6723	1222	F	-1.98 ± 0.09	-0.34	uf	D	-14.1	-2.14	14.716 ± 0.004	14.217 ± 0.004	0.505	0.492	0.513	8.59 ± 0.15	3.549 ± 0.007	2.132 ± 0.008	4.76 ± 0.05
36	…	190.0433	6.8465	1008	A	-2.31 ± 0.08	0.23	un	D	-15.8	-2.08	16.115 ± 0.005	15.803 ± 0.007	0.177	0.303	0.433	7.65 ± 0.15	1.750 ± 0.005	1.177 ± 0.006	2.68 ± 0.05
37	…	190.0736	6.7319	992	S	-2.34 ± 0.08	0.30	cn	D	-16.0	-2.14	17.433 ± 0.022	16.915 ± 0.009	0.556	0.547	0.545	7.54 ± 0.16	0.930 ± 0.005	0.596 ± 0.004	1.22 ± 0.02
38	…	190.0996	2.6085	1333	K	-3.09 ± 0.09	-1.06	un	D	-13.4	-2.04	16.507 ± 0.021	15.864 ± 0.013	0.673	0.628	0.638	8.17 ± 0.16	1.480 ± 0.010	1.443 ± 0.020	3.99 ± 0.20
39	…	190.1080	4.0502	727	S	-2.78 ± 0.11	-0.60	w	D	-14.5	-2.15	16.671 ± 0.018	16.069 ± 0.008	0.622	0.583	0.568	8.02 ± 0.15	1.100 ± 0.006	0.897 ± 0.007	2.25 ± 0.06
40	…	190.2098	4.5259	718	K	-1.57 ± 0.06	0.22	cn	D	-14.6	-2.19	15.188 ± 0.016	14.676 ± 0.006	0.331	0.629	0.580	8.43 ± 0.15	2.036 ± 0.005	1.012 ± 0.006	2.87 ± 0.06
41	…	190.3715	-0.7199	1181	K	-2.63 ± 0.09	0.33	uf	D	-14.8	-2.73	17.859 ± 0.018	17.422 ± 0.011	0.360	0.460	0.519	7.20 ± 0.15	0.757 ± 0.007	0.443 ± 0.005	1.03 ± 0.03
42	…	190.4383	4.0065	807	K	-2.85 ± 0.08	-0.94	un	D	-15.0	-1.81	15.968 ± 0.004	15.360 ± 0.021	0.649	0.601	0.574	8.31 ± 0.15	1.457 ± 0.004	0.882 ± 0.019	2.39 ± 0.15
43	…	190.4878	3.8192	881	K	-2.83 ± 0.08	-1.11	un	D	-15.8	-1.79	15.695 ± 0.008	15.045 ± 0.009	0.668	0.649	0.619	8.51 ± 0.15	1.878 ± 0.006	1.189 ± 0.011	3.29 ± 0.08
44	…	190.5745	3.4689	731	S	-2.77 ± 0.08	-1.08	un	D	-14.2	-1.83	15.430 ± 0.007	14.817 ± 0.004	0.618	0.631	0.602	8.54 ± 0.15	2.068 ± 0.005	1.732 ± 0.006	3.81 ± 0.04

Table 4
(Continued)

ID	Name	R.A.	Decl.	v_{hel}	References	log SFR	Δlog SFR	SFR Note	Image Source	log P_{ram}	log S_{tid}	g	r	$g-r$ Color at Center	$g-r$ Color at R_{50}	$g-r$ Color at $2R_{50}$	log M_*	$R_{25,g}$	R_{50}	R_{90}
		(deg)	(deg)	(km s^{-1})		($M_\odot$ yr^{-1})	(dex)			(Pa)	(dex)	(mag)	(mag)	(mag)	(mag)	(mag)	($M_\odot$)	(kpc)	(kpc)	(kpc)
(1)	(2)	(3)	(4)	(5)	(6)	(7)	(8)	(9)	(10)	(11)	(12)	(13)	(14)	(15)	(16)	(17)	(18)	(19)	(20)	(21)
45	…	190.5773	5.7394	972	A	-2.34 ± 0.08	0.28	un	D	−16.1	−2.37	16.434 ± 0.005	16.103 ± 0.007	0.303	0.276	0.377	7.56 ± 0.15	1.522 ± 0.008	0.943 ± 0.004	2.08 ± 0.03
46	…	190.5886	2.0666	1337	K	-2.11 ± 0.06	−0.52	cn	D	−13.4	−1.40	15.187 ± 0.003	14.569 ± 0.007	0.620	0.624	0.603	8.65 ± 0.15	1.720 ± 0.005	0.827 ± 0.007	3.18 ± 0.09
47	…	190.6190	1.0976	962	F	-2.32 ± 0.07	0.62	cn	D	−15.9	−2.18	16.980 ± 0.008	16.706 ± 0.005	0.189	0.279	0.380	7.22 ± 0.15	0.915 ± 0.004	0.428 ± 0.002	0.97 ± 0.01
48	N4630	190.6299	3.9588	740	A	-0.51 ± 0.07	0.19	cn	S	−14.5	−2.03	12.562 ± 0.002	11.999 ± 0.001	0.450	0.590	0.577	9.58 ± 0.15	5.562 ± 0.011	2.038 ± 0.003	5.72 ± 0.03
49	N4629	190.6362	−1.3502	1109	H	-1.92 ± 0.08	−0.36	w	D	−15.1	−2.92	13.714 ± 0.005	13.370 ± 0.003	0.312	0.338	0.349	8.67 ± 0.15	3.397 ± 0.011	1.503 ± 0.004	3.62 ± 0.03
50	…	190.6786	0.5922	1039	K	…	…	…	D	−15.2	−2.57	17.560 ± 0.009	16.966 ± 0.012	0.610	0.602	0.538	7.65 ± 0.15	0.753 ± 0.006	0.588 ± 0.006	1.37 ± 0.06
51	…	190.6889	3.4305	596	S	-2.11 ± 0.08	−0.19	cn	D	−13.7	−2.00	15.798 ± 0.015	15.228 ± 0.005	0.618	0.580	0.580	8.30 ± 0.15	1.859 ± 0.006	1.183 ± 0.006	3.30 ± 0.05
52	N4636	190.7072	2.6883	938	K	-0.25 ± 0.06	−1.03	cn	S	−13.7	−2.05	9.520 ± 0.009	8.788 ± 0.004	0.780	0.715	0.709	11.15 ± 0.15	25.054 ± 0.013	9.248 ± 0.044	31.28 ± 0.38
53	…	190.7348	3.6766	970	K	-2.00 ± 0.06	−0.90	cn	S	−15.5	−1.91	14.067 ± 0.009	13.418 ± 0.007	0.726	0.668	0.629	9.16 ± 0.15	2.472 ± 0.009	0.823 ± 0.006	2.56 ± 0.07
54	…	190.7490	2.1008	861	K	-3.62 ± 0.10	−1.25	un	D	−15.0	−1.66	17.499 ± 0.012	16.832 ± 0.017	0.673	0.711	0.583	7.82 ± 0.15	0.657 ± 0.008	0.774 ± 0.012	1.80 ± 0.08
55	…	190.7635	−0.4406	1079	K	-3.04 ± 0.13	0.14	un	D	−15.1	−2.62	18.601 ± 0.020	18.135 ± 0.023	0.574	0.465	0.489	6.97 ± 0.16	0.543 ± 0.006	0.437 ± 0.009	0.98 ± 0.06
56	N4643	190.8338	1.9782	1310	F	-0.92 ± 0.06	−1.33	cn	S	−13.5	−2.17	10.698 ± 0.002	9.931 ± 0.003	0.808	0.751	0.748	10.75 ± 0.15	10.898 ± 0.011	2.696 ± 0.014	10.58 ± 0.13
57	…	190.8377	3.4202	953	F	-2.88 ± 0.08	−0.61	uf	D	−15.7	−1.42	16.348 ± 0.007	15.852 ± 0.007	0.421	0.555	0.536	7.93 ± 0.15	1.461 ± 0.006	0.957 ± 0.007	2.31 ± 0.05
58	…	190.8492	1.4105	932	F	-3.02 ± 0.12	0.12	uf	D	−16.9	−1.85	17.779 ± 0.013	17.453 ± 0.019	0.249	0.355	0.394	7.01 ± 0.15	0.777 ± 0.014	0.980 ± 0.016	2.08 ± 0.09
59	…	190.9036	1.1501	743	S	-3.07 ± 0.12	−0.31	uf	D	−14.6	−2.46	18.027 ± 0.010	17.461 ± 0.013	0.613	0.566	0.501	7.40 ± 0.15	0.944 ± 0.010	0.698 ± 0.007	1.49 ± 0.05
60	…	190.9730	2.6334	1383	K	-3.02 ± 0.08	−0.66	un	D	−12.9	−1.62	16.688 ± 0.013	16.172 ± 0.006	0.431	0.562	0.547	7.83 ± 0.15	1.160 ± 0.006	0.634 ± 0.003	1.62 ± 0.03
61	…	191.0332	3.0061	1365	K	-2.85 ± 0.08	−1.04	un	D	−13.2	−1.85	15.870 ± 0.004	15.233 ± 0.004	0.665	0.608	0.633	8.41 ± 0.15	1.626 ± 0.006	0.917 ± 0.004	2.61 ± 0.04
62	…	191.0487	3.6068	814	K	-2.58 ± 0.08	−1.01	un	D	−14.8	−1.72	15.147 ± 0.017	14.529 ± 0.003	0.659	0.634	0.606	8.66 ± 0.15	2.213 ± 0.006	1.753 ± 0.006	4.87 ± 0.05
63	…	191.0622	2.4619	861	S	-2.39 ± 0.08	−0.01	cn	D	−14.9	−1.32	17.262 ± 0.009	16.641 ± 0.012	0.654	0.614	0.596	7.82 ± 0.15	1.198 ± 0.010	1.016 ± 0.011	2.68 ± 0.08
64	…	191.0725	2.6673	1077	K	-2.56 ± 0.09	−0.07	cn	D	−14.0	−1.71	17.817 ± 0.012	17.148 ± 0.014	0.700	0.721	0.645	7.70 ± 0.15	0.581 ± 0.005	0.447 ± 0.007	1.16 ± 0.04
65	…	191.0874	6.0898	1289	A	…	…	…	D	−14.5	−2.82	16.668 ± 0.006	16.284 ± 0.007	0.372	0.332	0.423	7.57 ± 0.15	1.601 ± 0.008	1.136 ± 0.007	2.76 ± 0.05
66	…	191.1067	3.5252	478	K	-2.18 ± 0.08	−0.91	cf	D	−13.6	−2.13	14.449 ± 0.007	13.814 ± 0.006	0.699	0.630	0.608	8.98 ± 0.15	3.043 ± 0.007	1.257 ± 0.010	3.94 ± 0.08
67	U7911	191.1198	0.4687	1180	F	-0.98 ± 0.07	0.27	cf	S	−14.5	−2.31	13.201 ± 0.011	12.798 ± 0.014	0.404	0.383	0.472	9.00 ± 0.15	6.275 ± 0.006	3.717 ± 0.044	6.81 ± 0.17
68	…	191.1393	1.7370	999	K	-2.78 ± 0.12	−0.84	un	D	−15.1	−1.89	16.099 ± 0.010	15.487 ± 0.011	0.631	0.594	0.579	8.27 ± 0.15	1.514 ± 0.006	1.245 ± 0.012	3.07 ± 0.10
69	…	191.1433	1.2753	1407	S	…	…	…	D	−13.7	−2.39	16.276 ± 0.009	15.668 ± 0.012	0.693	0.618	0.557	8.19 ± 0.15	1.331 ± 0.005	0.920 ± 0.011	2.82 ± 0.13
70	N4665	191.2751	3.0557	785	K	-1.52 ± 0.06	−1.85	cf	S	−14.4	−1.88	10.704 ± 0.009	9.977 ± 0.003	0.765	0.744	0.747	10.66 ± 0.15	11.098 ± 0.010	3.724 ± 0.014	11.00 ± 0.12
71	…	191.3969	1.9887	1246	K	-3.18 ± 0.08	−0.89	un	D	−13.9	−2.04	16.904 ± 0.011	16.315 ± 0.009	0.672	0.590	0.534	7.90 ± 0.15	1.055 ± 0.005	0.572 ± 0.004	1.36 ± 0.03
72	…	191.5065	4.3810	642	A	-2.24 ± 0.08	0.88	un	D	−14.4	−2.47	16.967 ± 0.010	16.785 ± 0.011	0.087	0.166	0.352	7.04 ± 0.15	1.469 ± 0.008	1.029 ± 0.009	2.40 ± 0.06
73	…	191.5685	2.0463	928	K	-2.61 ± 0.10	−0.31	cn	D	−17.2	−1.87	16.938 ± 0.007	16.343 ± 0.008	0.556	0.604	0.613	7.90 ± 0.15	1.002 ± 0.006	0.650 ± 0.005	1.69 ± 0.04
74	…	191.6382	3.2986	745	S	-2.78 ± 0.08	−0.86	uf	D	−14.5	−1.56	15.876 ± 0.003	15.293 ± 0.006	0.526	0.609	0.633	8.30 ± 0.15	2.279 ± 0.008	1.273 ± 0.006	2.93 ± 0.05
75	U7943	191.6912	5.9551	837	A	-1.96 ± 0.09	−0.44	w	S	−15.7	−2.46	13.241 ± 0.003	12.965 ± 0.011	0.538	0.323	0.228	8.72 ± 0.15	4.801 ± 0.011	2.352 ± 0.025	5.62 ± 0.23
76	…	191.7060	2.7136	946	K	-3.61 ± 0.11	−1.16	un	D	−16.1	−1.83	17.174 ± 0.021	16.611 ± 0.017	0.608	0.594	0.411	7.74 ± 0.16	0.749 ± 0.008	1.300 ± 0.023	4.07 ± 0.27
77	…	191.7067	3.0071	1232	A	-2.17 ± 0.08	0.34	uf	D	−13.9	−2.01	15.667 ± 0.005	15.427 ± 0.005	0.238	0.271	0.191	7.68 ± 0.15	1.903 ± 0.003	1.129 ± 0.004	2.20 ± 0.02
78	N4688	191.9447	4.3377	984	A	-0.51 ± 0.06	0.74	cn	S	−15.7	−1.94	12.471 ± 0.005	12.206 ± 0.007	0.432	0.252	0.188	9.01 ± 0.15	6.661 ± 0.013	3.534 ± 0.024	8.27 ± 0.12
79	…	191.9985	4.4335	1038	K	-1.87 ± 0.06	0.11	cn	D	−15.3	−1.27	14.945 ± 0.002	14.573 ± 0.002	0.391	0.323	0.497	8.24 ± 0.15	2.355 ± 0.004	1.189 ± 0.002	2.46 ± 0.01
80	…	191.9993	4.6949	1023	K	-2.50 ± 0.08	−0.95	un	D	−15.4	−2.14	15.043 ± 0.002	14.433 ± 0.003	0.579	0.620	0.621	8.69 ± 0.15	2.134 ± 0.005	1.024 ± 0.003	2.93 ± 0.03
81	N4701	192.2983	3.3888	719	A	-0.38 ± 0.06	0.59	cn	S	−14.6	−2.24	12.270 ± 0.001	11.903 ± 0.003	0.548	0.414	0.273	9.30 ± 0.15	6.160 ± 0.012	1.615 ± 0.005	5.99 ± 0.06
82	…	192.4259	5.4893	739	A	-2.46 ± 0.07	0.97	cn	D	−15.1	−2.18	17.918 ± 0.017	17.716 ± 0.021	0.078	0.279	0.421	6.70 ± 0.16	0.668 ± 0.005	0.476 ± 0.008	1.04 ± 0.07
83	U7983	192.4458	3.8421	694	A	-2.07 ± 0.08	0.47	un	D	−14.6	−2.34	15.595 ± 0.004	15.383 ± 0.005	0.160	0.243	0.275	7.65 ± 0.15	1.914 ± 0.008	1.261 ± 0.006	3.31 ± 0.04
84	U7982	192.4593	2.8511	1158	A	-1.29 ± 0.07	−0.41	cf	S	−14.5	−2.04	13.355 ± 0.003	12.731 ± 0.002	0.784	0.639	0.566	9.39 ± 0.15	8.399 ± 0.018	3.522 ± 0.006	8.30 ± 0.04
85	…	192.4848	2.5103	752	A	-2.48 ± 0.08	0.49	uf	D	−14.8	−2.28	17.054 ± 0.010	16.783 ± 0.007	0.137	0.262	0.390	7.19 ± 0.15	1.163 ± 0.005	0.594 ± 0.003	1.44 ± 0.02
86	N4713	192.4903	5.3110	653	A	-0.29 ± 0.06	0.67	cn	S	−14.7	−2.68	11.789 ± 0.004	11.510 ± 0.001	0.454	0.281	0.235	9.31 ± 0.15	6.123 ± 0.005	2.509 ± 0.002	4.90 ± 0.01
87	…	192.4966	5.8211	624	A	-2.51 ± 0.09	−0.06	uf	D	−14.7	−2.61	16.367 ± 0.008	15.965 ± 0.008	0.288	0.428	0.423	7.73 ± 0.15	1.003 ± 0.003	0.453 ± 0.003	1.13 ± 0.02
88	…	192.5196	−0.2323	754	K	-3.13 ± 0.09	−0.55	un	D	−15.2	−3.00	17.203 ± 0.010	16.696 ± 0.013	0.476	0.580	0.547	7.61 ± 0.15	0.814 ± 0.012	1.203 ± 0.012	2.75 ± 0.10

Table 4
(Continued)

ID	Name	R.A.	Decl.	v_{hel}	References	log SFR	Δlog SFR	SFR Note	Image Source	log P_{ram}	log S_{tid}	g	r	$g-r$ Color at			log M_*	$R_{25,g}$	R_{50}	R_{90}
		(deg)	(deg)	(km s^{-1})		($M_\odot$ yr^{-1})	(dex)			(Pa)	(dex)	(mag)	(mag)	Center (mag)	R_{50} (mag)	$2R_{50}$ (mag)	($M_\odot$)	(kpc)	(kpc)	(kpc)
(1)	(2)	(3)	(4)	(5)	(6)	(7)	(8)	(9)	(10)	(11)	(12)	(13)	(14)	(15)	(16)	(17)	(18)	(19)	(20)	(21)
89	…	192.5304	2.2479	1070	K	-3.09 ± 0.10	-1.00	un	D	-14.9	-2.12	16.433 ± 0.012	15.832 ± 0.010	0.603	0.588	0.622	8.11 ± 0.15	1.341 ± 0.006	1.108 ± 0.010	2.57 ± 0.07
90	…	192.6000	4.9057	650	A	-2.98 ± 0.10	0.38	uf	D	-14.6	-2.36	18.573 ± 0.034	18.206 ± 0.024	0.232	0.334	0.700	6.78 ± 0.17	0.601 ± 0.008	0.784 ± 0.015	1.73 ± 0.06
91	U7991	192.6626	1.4642	1272	A	-1.65 ± 0.07	-0.43	cf	S	-14.3	-2.16	14.194 ± 0.004	13.585 ± 0.003	0.689	0.587	0.624	9.02 ± 0.15	5.803 ± 0.024	2.500 ± 0.006	5.67 ± 0.04
92	…	192.6662	5.3480	675	A	-3.12 ± 0.08	0.64	un	D	-14.8	-1.98	19.169 ± 0.021	18.891 ± 0.033	0.157	0.238	0.385	6.36 ± 0.16	0.379 ± 0.008	0.352 ± 0.010	0.73 ± 0.03
93	…	192.6948	4.8899	721	S	-2.68 ± 0.09	0.41	cf	D	-14.9	-2.47	18.157 ± 0.013	17.727 ± 0.018	0.350	0.441	0.480	7.07 ± 0.15	0.566 ± 0.004	0.323 ± 0.005	0.82 ± 0.04
94	…	192.7508	1.8459	951	K	-3.18 ± 0.10	-1.09	un	D	-16.4	-2.01	16.478 ± 0.009	15.871 ± 0.013	0.639	0.595	0.570	8.11 ± 0.15	1.750 ± 0.008	1.073 ± 0.012	2.61 ± 0.10
95	…	193.0375	3.1210	1031	K	-3.47 ± 0.09	-1.16	un	D	-15.3	-2.21	16.960 ± 0.010	16.367 ± 0.011	0.616	0.625	0.537	7.89 ± 0.15	1.118 ± 0.009	1.048 ± 0.009	2.50 ± 0.10
96	…	193.0644	4.4575	701	A	-2.28 ± 0.06	0.94	cn	D	-14.8	-2.54	17.530 ± 0.012	17.290 ± 0.017	0.172	0.185	0.208	6.93 ± 0.15	1.263 ± 0.010	1.070 ± 0.016	2.50 ± 0.10
97	…	193.1421	−0.1679	1021	K	-2.93 ± 0.10	0.86	uf	D	-15.6	-2.61	18.612 ± 0.011	18.459 ± 0.019	0.264	0.140	0.119	6.32 ± 0.15	0.608 ± 0.002	0.421 ± 0.005	0.83 ± 0.04
98	…	193.2059	1.7346	836	K	-3.60 ± 0.11	-1.21	uf	D	-15.6	-2.32	17.204 ± 0.009	16.607 ± 0.012	0.627	0.602	0.589	7.80 ± 0.15	0.873 ± 0.007	0.696 ± 0.008	1.71 ± 0.05
99	N4771	193.3384	1.2692	1133	A	-0.78 ± 0.06	-0.34	cf	S	-14.9	-2.12	12.323 ± 0.006	11.678 ± 0.004	0.795	0.663	0.552	9.85 ± 0.15	9.909 ± 0.015	3.608 ± 0.013	8.06 ± 0.08
100	…	193.3508	1.9314	889	S	-3.27 ± 0.09	-1.09	un	D	-16.5	-1.81	16.663 ± 0.023	16.062 ± 0.007	0.607	0.634	0.600	8.02 ± 0.16	1.202 ± 0.005	0.924 ± 0.006	2.17 ± 0.05
101	N4772	193.3714	2.1683	1043	A	-1.06 ± 0.06	-1.10	cf	S	-15.3	-2.22	11.438 ± 0.001	10.717 ± 0.004	0.778	0.698	0.681	10.36 ± 0.15	11.266 ± 0.016	4.003 ± 0.023	13.04 ± 0.24
102	…	193.4160	1.5749	1087	K	-2.93 ± 0.08	-0.32	uf	D	-15.1	-1.51	17.051 ± 0.007	16.593 ± 0.009	0.463	0.460	0.491	7.57 ± 0.15	1.555 ± 0.009	1.066 ± 0.008	2.55 ± 0.07
103	…	193.4174	4.0758	899	A	-2.72 ± 0.09	-0.13	uf	D	-16.9	-2.44	16.951 ± 0.011	16.501 ± 0.010	0.384	0.421	0.565	7.59 ± 0.15	0.920 ± 0.004	0.577 ± 0.004	1.42 ± 0.04
104	…	193.4304	4.1541	768	A	-2.13 ± 0.07	0.84	cf	D	-15.2	-2.32	16.969 ± 0.006	16.712 ± 0.009	0.133	0.221	0.443	7.19 ± 0.15	0.752 ± 0.004	0.340 ± 0.003	0.87 ± 0.02
105	…	193.5210	−0.1012	840	K	-2.70 ± 0.09	-0.69	un	D	-15.9	-2.87	15.914 ± 0.013	15.371 ± 0.012	0.421	0.582	0.584	8.20 ± 0.15	1.451 ± 0.006	1.289 ± 0.016	3.23 ± 0.11
106	…	193.5526	0.8026	1202	A	-2.14 ± 0.08	0.03	un	D	-14.7	-2.31	15.749 ± 0.002	15.320 ± 0.008	0.326	0.424	0.522	8.03 ± 0.15	1.481 ± 0.005	0.530 ± 0.004	1.71 ± 0.05
107	…	193.5661	2.7626	905	A	-2.44 ± 0.08	-0.33	uf	D	-17.1	-1.65	15.997 ± 0.009	15.491 ± 0.008	0.436	0.493	0.584	8.09 ± 0.15	2.391 ± 0.007	1.658 ± 0.012	4.07 ± 0.09
108	…	193.6574	1.3258	1197	K	-2.81 ± 0.08	-0.28	uf	D	-14.7	-1.99	16.946 ± 0.008	16.465 ± 0.006	0.252	0.551	0.556	7.66 ± 0.15	1.016 ± 0.006	0.560 ± 0.003	1.46 ± 0.02
109	…	193.6734	2.1042	858	K	-2.02 ± 0.06	-0.63	cf	D	-15.9	-2.06	14.454 ± 0.002	13.873 ± 0.002	0.499	0.602	0.613	8.86 ± 0.15	1.941 ± 0.002	0.715 ± 0.001	1.53 ± 0.01
110	N4809	193.7131	2.6529	935	K	-0.97 ± 0.07	…	cf	D	-17.2	-0.09	13.868 ± 0.002	13.640 ± 0.001	0.250	0.213	0.276	8.37 ± 0.15	4.534 ± 0.003	2.086 ± 0.002	4.14 ± 0.01
111	N4810	193.7133	2.6407	899	K	-1.06 ± 0.07	…	cf	D	-16.9	-0.08	14.288 ± 0.003	14.023 ± 0.006	0.117	0.174	0.567	8.28 ± 0.15	2.344 ± 0.005	1.013 ± 0.004	2.78 ± 0.07
112	…	193.7407	1.9786	1081	A	-2.91 ± 0.09	-0.42	uf	S	-15.1	-1.79	16.753 ± 0.024	16.289 ± 0.060	0.349	0.597	0.385	7.70 ± 0.19	1.012 ± 0.012	1.524 ± 0.074	3.75 ± 0.36
113	N4808	193.9540	4.3042	758	A	-0.21 ± 0.07	0.49	cn	S	-15.2	-2.43	11.955 ± 0.001	11.513 ± 0.004	0.689	0.449	0.317	9.58 ± 0.15	7.162 ± 0.014	2.479 ± 0.008	5.55 ± 0.07
114	U8053	193.9556	4.0123	708	A	-1.24 ± 0.08	0.69	cf	D	-15.0	-1.91	14.239 ± 0.002	13.982 ± 0.003	0.358	0.258	0.205	8.28 ± 0.15	3.880 ± 0.006	2.048 ± 0.007	4.66 ± 0.03
115	U8055	194.0185	3.8128	616	A	-1.60 ± 0.07	0.95	cf	S	-14.6	-2.41	15.410 ± 0.041	15.243 ± 0.016	0.269	0.101	0.156	7.63 ± 0.17	2.059 ± 0.029	2.403 ± 0.044	5.33 ± 0.11
116	…	194.2377	4.0647	828	A	-1.75 ± 0.07	0.28	cn	D	-15.7	-2.11	14.778 ± 0.004	14.467 ± 0.004	0.292	0.280	0.361	8.18 ± 0.15	2.341 ± 0.004	1.058 ± 0.004	2.25 ± 0.03
117	…	194.3255	4.9912	883	A	-2.82 ± 0.09	1.20	uf	D	-16.6	-3.06	18.915 ± 0.014	18.817 ± 0.026	−0.062	0.066	0.268	6.09 ± 0.16	0.411 ± 0.002	0.281 ± 0.005	0.58 ± 0.04
118	U8074	194.4352	2.6918	925	A	-1.44 ± 0.07	0.71	cf	D	-18.3	-2.37	14.963 ± 0.003	14.679 ± 0.004	0.410	0.193	0.249	8.05 ± 0.15	2.462 ± 0.005	1.650 ± 0.005	3.58 ± 0.03
119	N4845	194.5050	1.5758	1072	A	-0.26 ± 0.08	-0.39	cn	S	-15.3	-2.48	11.524 ± 0.001	10.742 ± 0.001	1.060	0.749	0.684	10.45 ± 0.15	13.744 ± 0.027	4.959 ± 0.004	11.16 ± 0.03

Notes. Column (1): ID. Column (2): NGC/UGC/IC ID. Columns (3)–(4): R.A. and decl. in decimal degrees (J2000). Column (5): heliocentric radial velocity. Column (6): source of v_{hel}; FAST (F), ALFALFA (A), K&T17 (K), SDSS DR16 `SpecObj` table (S), and HIPASS Bright Galaxy Catalog (BGC; H). Column (7): star formation rate. Column (8): offset from SFMS. Column (9): note on SFR measurement; estimated solely from UV data (u), from W4-band data (w), and UV and W4 data combined (c); if UV data are used, FUV (f, preferred), and NUV (n, when FUV is unavailable). Column (10): source of optical images; SDSS (S), and DECaLS (D). Column (11): ram pressure estimated using projected parameters. Column (12): tidal strength parameter. Columns (13)–(14): total g- and r-bands AB magnitude using GC method. Columns (15)–(17): the $g-r$ color at the galaxy center, R_{50}, and $2R_{50}$. Column (18): stellar mass; the uncertainty from distance is not included. Column (19): the radius at which the g-band SB drops to 25 mag arcsec^{-2}, assuming a precise distance of 16.2 Mpc. Columns (20)–(21): the radii enclosing 50% and 90% of r-band fluxes.

[a] This H I-nondetected galaxy (#20) has a distinctly red color ($g-r=1.767$ mag), and we assigned it the 95th percentile of $g-r$ among our samples (0.744 mag) for stellar mass calculation instead. Since most of our discussion is focused on H I-detections, this color assignment does not change our major results.

(This table is available in its entirety in machine-readable form.)

Table 5
H I-related Properties and Measurements

ID	FAST	ALFALFA	HIPASS	WALLABY	$\log M_{\rm H\,I}$ ($M_\odot$)	References	$\Delta\log M_{\rm H\,I}$ (dex)	$\log S_{\rm RPS}$ (dex)	$\log f_{\rm RPS}$ (dex)	$\log f_{\rm tid}$ (dex)	$\log f_{\rm str}$ (dex)	Stripping Status
(1)	(2)	(3)	(4)	(5)	(6)	(7)	(8)	(9)	(10)	(11)	(12)	(13)
2	…	221639	…	…	9.14 ± 0.04	A	1.63	−1.55	−0.95	…	−0.95	R
3	…	224278	…	…	7.70 ± 0.05	A	−0.30	−3.86	…	…	…	N
4	…	7609	…	…	8.40 ± 0.04	A	−1.15	…	…	…	…	N
5	32	…	…	…	7.11 ± 0.05	F	−0.83	−0.84	…	−0.21	−0.21	T
6	24	225760	…	…	7.71 ± 0.04	F	−0.69	−1.31	−1.64	…	−1.64	R
8	27	221570	…	J123103+014032	8.23 ± 0.04	F	−0.05	−1.98	−1.37	…	−1.37	R
13	33	220761	…	…	7.78 ± 0.04	F	−0.40	−1.32	−1.39	…	−1.39	R
14	…	220762	…	J123257+043441	8.29 ± 0.04	A	0.27	−1.36	−1.02	…	−1.02	R
15	34	…	…	J123308-003203	8.21 ± 0.04	F	0.00	−2.11	−1.39	…	−1.39	R
16	30	220780	…	J123329+034732	7.85 ± 0.04	F	−0.58	−3.23	…	…	…	N
17	26	7715	…	J123355+033243	8.15 ± 0.04	F	−0.44	−1.16	−1.41	…	−1.41	R
18	…	223873	…	…	7.43 ± 0.05	A	−0.12	−1.86	−1.21	…	−1.21	R
19	…	222310	…	…	7.63 ± 0.06	A	−0.83	…	…	…	…	N
21	23	7756	…	…	8.30 ± 0.04	F	−0.79	0.37	−1.56	…	−1.56	R
23	…	7781	…	J123636+063715	9.00 ± 0.04	A	0.47	−2.34	−1.39	−0.58	−0.58	T
24	25	…	…	…	7.13 ± 0.04	F	−0.11	−1.88	−1.24	…	−1.24	R
26	35	222680	…	…	7.95 ± 0.04	F	−0.11	−0.03	−0.88	…	−0.88	R
29	…	7794	…	…	7.56 ± 0.06	A	−1.77	…	…	…	…	N
31	…	7804	…	J123827+041912	7.99 ± 0.05	A	−1.42	…	…	…	…	N
33	51_2	…	…	…	7.98 ± 0.04	F	0.28	−1.97	−1.20	…	−1.20	R
35	21	7824	…	J123949+014016	8.29 ± 0.04	F	−0.25	−0.31	−0.90	−1.91	−0.90	R
36	…	220903	…	J124009+065029	7.53 ± 0.05	A	−0.37	−1.50	…	…	…	N
45	…	220939	…	J124218+054425	8.12 ± 0.04	A	0.28	−3.04	−1.91	−1.06	−1.06	T
47	28	224293	…	J124228+010549	7.51 ± 0.04	F	−0.08	−2.76	−1.75	−0.76	−0.76	T
48	…	7871	…	J124231+035729	8.67 ± 0.04	A	−0.45	−0.98	−1.24	−1.16	−1.16	T
49	…	…	J1242-01	…	9.26 ± 0.07	H	0.66	−2.30	−1.26	−1.71	−1.26	R
56	18	7895	…	J124318+015754	7.89 ± 0.04	F	−1.76	…	…	…	…	N
57	29	220964	…	…	7.18 ± 0.04	F	−0.92	−1.01	…	−0.30	−0.30	T
58	31	…	…	…	7.06 ± 0.05	F	−0.37	−3.16	…	−0.57	−0.57	T
65	…	227896	…	…	7.85 ± 0.04	A	0.00	−1.06	−1.00	…	−1.00	R
67	22	7911	…	J124428+002815	9.01 ± 0.04	F	0.22	−1.20	−1.06	−1.94	−1.06	R
72	…	227970	…	J124601+042248	8.04 ± 0.04	A	0.59	−1.25	−0.89	−2.00	−0.89	R
75	…	7943	…	J124645+055723	8.85 ± 0.04	A	0.22	−2.38	−1.60	…	−1.60	R
77	…	222214	…	…	7.67 ± 0.05	A	−0.25	0.23	−0.76	−1.52	−0.76	R
78	…	7961	…	J124747+042017	9.29 ± 0.04	A	0.50	−2.54	−1.58	−0.29	−0.29	T
79	…	222216	…	J124800+042609	7.94 ± 0.04	W	−0.37	−1.60	−1.71	−0.08	−0.08	T
81	…	7975	…	…	9.47 ± 0.04	A	0.51	−1.61	−1.00	−0.37	−0.37	T
82	…	225197	…	…	7.67 ± 0.06	A	0.47	−2.11	−1.23	−0.32	−0.32	T
83	…	7983	…	…	8.62 ± 0.04	A	0.72	−1.63	−1.00	−0.45	−0.45	T
84	…	7982	…	…	8.66 ± 0.04	A	−0.35	0.83	−1.24	…	−1.24	R
85	…	224225	…	…	7.82 ± 0.05	A	0.26	−1.66	−1.09	−0.90	−0.90	T
86	…	7985	…	…	9.47 ± 0.04	A	0.50	−1.71	−1.05	−1.43	−1.05	R
87	…	224226	…	…	7.70 ± 0.05	A	−0.26	−1.74	−1.06	…	−1.06	R
90	…	227972	…	…	7.39 ± 0.06	A	0.14	−1.64	−1.07	−1.17	−1.07	R
91	…	7991	…	J125038+012749	8.32 ± 0.04	A	−0.49	1.02	−1.21	…	−1.21	R
92	…	227973	…	…	7.37 ± 0.05	A	0.44	−1.87	−1.11	−0.09	−0.09	T
96	…	226122	…	…	8.02 ± 0.04	A	0.65	−1.76	−1.11	−1.72	−1.11	R
99	…	8020	…	…	8.86 ± 0.04	A	−0.39	0.13	−1.51	…	−1.51	R
101	…	8021	…	…	8.95 ± 0.04	A	−0.54	−0.78	…	…	…	N
103	…	224229	…	…	7.46 ± 0.05	A	−0.40	−3.80	…	…	…	N
104	…	224230	…	…	7.62 ± 0.05	A	0.05	−2.27	−1.29	−0.62	−0.62	T
106	…	222350	…	…	7.64 ± 0.06	A	−0.53	−1.20	−1.21	…	−1.21	R
107	…	229204	…	…	7.92 ± 0.04	A	−0.29	−3.25	…	−0.34	−0.34	T
110	…	8034	…	…	9.04 ± 0.04[a]	A	…	…	…	…	…	M
111	…	8034	…	…	9.04 ± 0.04[a]	A	…	…	…	…	…	M
112	…	229185	…	…	7.53 ± 0.06	A	−0.41	−2.02	−1.53	−0.22	−0.22	T
113	…	8054	…	…	9.63 ± 0.04	A	0.52	−2.20	−1.31	−0.56	−0.56	T
114	…	8053	…	…	8.97 ± 0.04	A	0.63	−1.91	−1.17	−0.18	−0.18	T
115	…	8055	…	…	8.78 ± 0.04	A	0.89	−1.68	−1.05	−0.47	−0.47	T
116	…	222260	…	…	8.32 ± 0.04	A	0.05	−2.56	−1.65	−0.60	−0.60	T

Table 5
(Continued)

ID	FAST	ALFALFA	HIPASS	WALLABY	$\log M_{\rm H\,I}$ ($M_\odot$)	References	$\Delta\log M_{\rm H\,I}$ (dex)	$\log S_{\rm RPS}$ (dex)	$\log f_{\rm RPS}$ (dex)	$\log f_{\rm tid}$ (dex)	$\log f_{\rm str}$ (dex)	Stripping Status
(1)	(2)	(3)	(4)	(5)	(6)	(7)	(8)	(9)	(10)	(11)	(12)	(13)
117	…	227975	…	…	7.51 ± 0.05	A	0.78	−3.65	…	…	…	N
118	…	8074	…	…	8.59 ± 0.04	A	0.40	−5.31	…	−0.90	−0.90	T
119	…	8078	…	…	8.06 ± 0.05	A	−1.46	…	…	…	…	N

Notes. Column (1): ID. Column (2): ID in Zuo et al. (2022). Column (3): ALFALFA catalog number. Column (4): HIPASS BGC name. Column (5): WALLABY identifier. Column (6): H I mass; the uncertainties in H I flux and the calibration are considered here. Column (7): source of H I flux; FAST (F), ALFALFA (A), HIPASS BGC (H), and WALLABY Pilot Survey (W). Column (8): offset from the mean $M_{\rm H\,I}$ relation. Column (9): RPS strength parameter; galaxies with too little gas for the calculation of $S_{\rm RPS}$ are omitted. Columns (10)–(12): fraction of gas under RPS, TS, and total stripping; values smaller than 1% are omitted. Column (13): stripping status; RPS sample (R), TS sample (T), non-stripping galaxies (N), and merging pair (M).
[a] Galaxy #110 and #111 are merging, and their H I fluxes are inseparable. Their total $M_{\rm H\,I}$ is reported here and should be considered as the upper limit.

(This table is available in its entirety in machine-readable form.)

ORCID iDs

Xuchen Lin (林旭辰) https://orcid.org/0000-0002-4250-2709
Jing Wang (王菁) https://orcid.org/0000-0002-6593-8820
Virginia Kilborn https://orcid.org/0000-0003-3636-4474
Eric W. Peng https://orcid.org/0000-0002-2073-2781
Luca Cortese https://orcid.org/0000-0002-7422-9823
Alessandro Boselli https://orcid.org/0000-0002-9795-6433
Bumhyun Lee https://orcid.org/0000-0002-3810-1806
Barbara Catinella https://orcid.org/0000-0002-7625-562X
N. Deg https://orcid.org/0000-0003-3523-7633
H. Dénes https://orcid.org/0000-0002-9214-8613
P. Kamphuis https://orcid.org/0000-0002-5425-6074
B. S. Koribalski https://orcid.org/0000-0003-4351-993X
K. Lee-Waddell https://orcid.org/0000-0003-4844-8659
Jonghwan Rhee https://orcid.org/0000-0001-8496-4306
Li Shao (邵立) https://orcid.org/0000-0003-2015-777X
Kristine Spekkens https://orcid.org/0000-0002-0956-7949
Lister Staveley-Smith https://orcid.org/0000-0002-8057-0294
T. Westmeier https://orcid.org/0000-0002-5300-2486
O. Ivy Wong https://orcid.org/0000-0003-4264-3509
Kenji Bekki https://orcid.org/0000-0001-6163-4726
Albert Bosma https://orcid.org/0000-0002-1128-6089
Min Du (杜敏) https://orcid.org/0000-0001-9953-0359
Luis C. Ho https://orcid.org/0000-0001-6947-5846
Lourdes Verdes-Montenegro https://orcid.org/0000-0003-0156-6180
Huiyuan Wang (王慧元) https://orcid.org/0000-0002-4911-6990
Shun Wang (王舜) https://orcid.org/0000-0002-9663-3384

References

Abadi, M. G., Moore, B., & Bower, R. G. 1999, MNRAS, 308, 947
Ahumada, R., Allende Prieto, C., Almeida, A., et al. 2020, ApJS, 249, 3
Alam, S., Albareti, F. D., Allende Prieto, C., et al. 2015, ApJS, 219, 12
Astropy Collaboration, Price-Whelan, A. M., Lim, P. L., et al. 2022, ApJ, 935, 167
Ayromlou, M., Kauffmann, G., Yates, R. M., Nelson, D., & White, S. D. M. 2021, MNRAS, 505, 492
Bacchini, C., Fraternali, F., Pezzulli, G., & Marasco, A. 2020, A&A, 644, A125
Bertin, E., & Arnouts, S. 1996, A&AS, 117, 393
Bertin, E., Mellier, Y., Radovich, M., et al. 2002, in ASP Conf. Ser. 281, Astronomical Data Analysis Software and Systems XI, ed. D. A. Bohlender, D. Durand, & T. H. Handley (San Francisco, CA: ASP), 228
Blanton, M. R., & Moustakas, J. 2009, ARA&A, 47, 159
Blumenthal, K. A., & Barnes, J. E. 2018, MNRAS, 479, 3952
Bolatto, A. D., Leroy, A. K., Jameson, K., et al. 2011, ApJ, 741, 12
Boselli, A., Fossati, M., Consolandi, G., et al. 2018, A&A, 620, A164
Boselli, A., Fossati, M., & Sun, M. 2022, A&ARv, 30, 3
Boselli, A., & Gavazzi, G. 2006, PASP, 118, 517
Boselli, A., & Gavazzi, G. 2014, A&ARv, 22, 74
Boselli, A., Roehlly, Y., Fossati, M., et al. 2016, A&A, 596, A11
Boselli, A., Voyer, E., Boissier, S., et al. 2014, A&A, 570, A69
Bradley, L., Sipőcz, B., Robitaille, T., et al. 2021, astropy/photutils v1.2.0, Zenodo, doi:10.5281/zenodo.5525286
Brough, S., Forbes, D. A., Kilborn, V. A., Couch, W., & Colless, M. 2006, MNRAS, 369, 1351
Brown, T., Catinella, B., Cortese, L., et al. 2017, MNRAS, 466, 1275
Bustard, C., Pardy, S. A., D'Onghia, E., Zweibel, E. G., & Gallagher, J. S. I. 2018, ApJ, 863, 49
Calette, A. R., Avila-Reese, V., Rodríguez-Puebla, A., Hernández-Toledo, H., & Papastergis, E. 2018, RMxAA, 54, 443
Calzetti, D. 2013, in Secular Evolution of Galaxies, ed. J. Falcón-Barroso & J. H. Knapen (Cambridge: Cambridge Univ. Press), 419
Calzetti, D., Armus, L., Bohlin, R. C., et al. 2000, ApJ, 533, 682
Cardelli, J. A., Clayton, G. C., & Mathis, J. S. 1989, ApJ, 345, 245
Chabrier, G. 2003, PASP, 115, 763
Chung, A., van Gorkom, J. H., Kenney, J. D. P., Crowl, H., & Vollmer, B. 2009, AJ, 138, 1741
Chung, A., van Gorkom, J. H., Kenney, J. D. P., & Vollmer, B. 2007, ApJL, 659, L115
Cook, D. O., Dale, D. A., Johnson, B. D., et al. 2014, MNRAS, 445, 899
Cortese, L., Catinella, B., & Smith, R. 2021, PASA, 38, e035
Cowie, L. L., & McKee, C. F. 1977, ApJ, 211, 135
Cramer, W. J., Kenney, J. D. P., Cortes, J. R., et al. 2020, ApJ, 901, 95
Cramer, W. J., Kenney, J. D. P., Tonnesen, S., et al. 2021, ApJ, 921, 22
Dawson, K. S., Kneib, J.-P., Percival, W. J., et al. 2016, AJ, 151, 44
De Lucia, G., Weinmann, S., Poggianti, B. M., Aragón-Salamanca, A., & Zaritsky, D. 2012, MNRAS, 423, 1277
Dey, A., Schlegel, D. J., Lang, D., et al. 2019, AJ, 157, 168
Di Matteo, P., Combes, F., Melchior, A. L., & Semelin, B. 2007, A&A, 468, 61
Dressler, A. 1980, ApJ, 236, 351
Eckert, D., Molendi, S., & Paltani, S. 2011, A&A, 526, A79
Ellison, S. L., Catinella, B., & Cortese, L. 2018, MNRAS, 478, 3447
Elmegreen, B. G., Struck, C., & Hunter, D. A. 2014, ApJ, 796, 110
Elmegreen, D. M., Sundin, M., Elmegreen, B., & Sundelius, B. 1991, A&A, 244, 52
Evrard, A. E., Bialek, J., Busha, M., et al. 2008, ApJ, 672, 122
Ferragamo, A., De Petris, M., Yepes, G., et al. 2022, EPJWC, 257, 00018
Font, A. S., Bower, R. G., McCarthy, I. G., et al. 2008, MNRAS, 389, 1619
For, B. Q., Wang, J., Westmeier, T., et al. 2021, MNRAS, 507, 2300
Foreman-Mackey, D., Hogg, D. W., Lang, D., & Goodman, J. 2013, PASP, 125, 306
Fukazawa, Y., Makishima, K., & Ohashi, T. 2004, PASJ, 56, 965

Ginsburg, A., Sipőcz, B. M., Brasseur, C. E., et al. 2019, AJ, 157, 98
Giovanelli, R., Haynes, M. P., Kent, B. R., et al. 2005, AJ, 130, 2598
Gunn, J. E., & Gott, J. R. I. 1972, ApJ, 176, 1
Guo, H., Jones, M. G., Wang, J., & Lin, L. 2021, ApJ, 918, 53
Haines, C. P., Pereira, M. J., Smith, G. P., et al. 2015, ApJ, 806, 101
Harris, C. R., Millman, K. J., van der Walt, S. J., et al. 2020, Natur, 585, 357
Haynes, M. P., Giovanelli, R., Kent, B. R., et al. 2018, ApJ, 861, 49
Henriques, B. M. B., White, S. D. M., Thomas, P. A., et al. 2015, MNRAS, 451, 2663
Hess, K. M., & Wilcots, E. M. 2013, AJ, 146, 124
Huang, S., Haynes, M. P., Giovanelli, R., & Brinchmann, J. 2012, ApJ, 756, 113
Jáchym, P., Kenney, J. D. P., Ržuička, A., et al. 2013, A&A, 556, A99
Jaffé, Y. L., Poggianti, B. M., Moretti, A., et al. 2018, MNRAS, 476, 4753
Jaffé, Y. L., Smith, R., Candlish, G. N., et al. 2015, MNRAS, 448, 1715
Jeans, J. H. 1902, RSPTA, 199, 1
Johnson, R., Chakrabarty, D., O'Sullivan, E., & Raychaudhury, S. 2009, ApJ, 706, 980
Jones, M. G., Verdes-Montenegro, L., Damas-Segovia, A., et al. 2019, A&A, 632, A78
Jung, S. L., Choi, H., Wong, O. I., et al. 2018, ApJ, 865, 156
Kazantzidis, S., Mayer, L., Callegari, S., Dotti, M., & Moustakas, L. A. 2017, ApJL, 836, L13
Köppen, J., Jáchym, P., Taylor, R., & Palouš, J. 2018, MNRAS, 479, 4367
Koribalski, B. S., Staveley-Smith, L., Kilborn, V. A., et al. 2004, AJ, 128, 16
Koribalski, B. S., Staveley-Smith, L., Westmeier, T., et al. 2020, Ap&SS, 365, 118
Kourkchi, E., Courtois, H. M., Graziani, R., et al. 2020, AJ, 159, 67
Kourkchi, E., & Tully, R. B. 2017, ApJ, 843, 16
Lelli, F., McGaugh, S. S., Schombert, J. M., & Pawlowski, M. S. 2017, ApJ, 836, 152
Leroy, A. K., Walter, F., Brinks, E., et al. 2008, AJ, 136, 2782
Loni, A., Serra, P., Kleiner, D., et al. 2021, A&A, 648, A31
Marasco, A., Crain, R. A., Schaye, J., et al. 2016, MNRAS, 461, 2630
Marinacci, F., Vogelsberger, M., Pakmor, R., et al. 2018, MNRAS, 480, 5113
Martin, D. C., Fanson, J., Schiminovich, D., et al. 2005, ApJL, 619, L1
Matsushita, K., Makishima, K., Ikebe, Y., et al. 1998, ApJL, 499, L13
McGaugh, S. S., Schombert, J. M., Bothun, G. D., & de Blok, W. J. G. 2000, ApJL, 533, L99
McPartland, C., Ebeling, H., Roediger, E., & Blumenthal, K. 2016, MNRAS, 455, 2994
Merritt, D. 1984, ApJ, 276, 26
Mo, H. J., Mao, S., & White, S. D. M. 1998, MNRAS, 295, 319
Mok, A., Wilson, C. D., Knapen, J. H., et al. 2017, MNRAS, 467, 4282
Moon, J.-S., An, S.-H., & Yoon, S.-J. 2019, ApJ, 882, 14
Moretti, A., Paladino, R., Poggianti, B. M., et al. 2020, ApJL, 897, L30
Moretti, A., Radovich, M., Poggianti, B. M., et al. 2022, ApJ, 925, 4
Morokuma-Matsui, K., Bekki, K., Wang, J., et al. 2022, ApJS, 263, 40
Murugeshan, C., Kilborn, V. A., For, B. Q., et al. 2021, MNRAS, 507, 2949
Naiman, J. P., Pillepich, A., Springel, V., et al. 2018, MNRAS, 477, 1206
Navarro, J. F., Frenk, C. S., & White, S. D. M. 1996, ApJ, 462, 563
Nelson, D., Pillepich, A., Springel, V., et al. 2018, MNRAS, 475, 624
Oman, K. A., Bahé, Y. M., Healy, J., et al. 2021, MNRAS, 501, 5073
Oman, K. A., & Hudson, M. J. 2016, MNRAS, 463, 3083
Oman, K. A., Hudson, M. J., & Behroozi, P. S. 2013, MNRAS, 431, 2307
Ostriker, E. C., McKee, C. F., & Leroy, A. K. 2010, ApJ, 721, 975
Pan, H.-A., Lin, L., Hsieh, B.-C., et al. 2019, ApJ, 881, 119
Pillepich, A., Nelson, D., Hernquist, L., et al. 2018, MNRAS, 475, 648
Poggianti, B. M., Fasano, G., Omizzolo, A., et al. 2016, AJ, 151, 78
Poggianti, B. M., Moretti, A., Gullieuszik, M., et al. 2017, ApJ, 844, 48
Poggianti, B. M., Smail, I., Dressler, A., et al. 1999, ApJ, 518, 576
Quilis, V., Planelles, S., & Ricciardelli, E. 2017, MNRAS, 469, 80
Reiprich, T. H., & Böhringer, H. 2002, ApJ, 567, 716
Rhee, J., Smith, R., Choi, H., et al. 2020, ApJS, 247, 45
Rix, H.-W., Barden, M., Beckwith, S. V. W., et al. 2004, ApJS, 152, 163
Roberts, I. D., Lang, M., Trotsenko, D., et al. 2022, ApJ, 941, 77
Ruggiero, R., Machado, R. E. G., Roman-Oliveira, F. V., et al. 2019, MNRAS, 484, 906
Saintonge, A., & Catinella, B. 2022, ARA&A, 60, 319
Saintonge, A., Catinella, B., Cortese, L., et al. 2016, MNRAS, 462, 1749
Saintonge, A., Catinella, B., Tacconi, L. J., et al. 2017, ApJS, 233, 22
Schiminovich, D., Catinella, B., Kauffmann, G., et al. 2010, MNRAS, 408, 919
Schlegel, D. J., Finkbeiner, D. P., & Davis, M. 1998, ApJ, 500, 525
Sereno, M., Umetsu, K., Ettori, S., et al. 2020, MNRAS, 492, 4528
Shandarin, S. F., & Zeldovich, Y. B. 1989, RvMP, 61, 185
Shaya, E. J., Tully, R. B., Hoffman, Y., & Pomarède, D. 2017, ApJ, 850, 207
Smethurst, R. J., Lintott, C. J., Bamford, S. P., et al. 2017, MNRAS, 469, 3670
Somerville, R. S., & Davé, R. 2015, ARA&A, 53, 51
Sparre, M., Whittingham, J., Damle, M., et al. 2022, MNRAS, 509, 2720
Springel, V., Pakmor, R., Pillepich, A., et al. 2018, MNRAS, 475, 676
Stevens, A. R. H., & Brown, T. 2017, MNRAS, 471, 447
Stevens, A. R. H., Diemer, B., Lagos, C. d. P., et al. 2019, MNRAS, 483, 5334
Taffoni, G., Mayer, L., Colpi, M., & Governato, F. 2003, MNRAS, 341, 434
Thorp, M. D., Ellison, S. L., Simard, L., Sánchez, S. F., & Antonio, B. 2019, MNRAS, 482, L55
Tonnesen, S., & Bryan, G. L. 2012, MNRAS, 422, 1609
Tully, R. B. 2015, AJ, 149, 54
Tully, R. B., Courtois, H. M., & Sorce, J. G. 2016, AJ, 152, 50
Vallat, R. 2018, JOSS, 3, 1026
Veilleux, S., Cecil, G., & Bland-Hawthorn, J. 2005, ARA&A, 43, 769
Virtanen, P., Gommers, R., Oliphant, T. E., et al. 2020, NatMe, 17, 261
Vollmer, B. 2003, A&A, 398, 525
Vollmer, B., Wong, O. I., Braine, J., Chung, A., & Kenney, J. D. P. 2012, A&A, 543, A33
Vulcani, B., Poggianti, B. M., Gullieuszik, M., et al. 2018a, ApJL, 866, L25
Vulcani, B., Poggianti, B. M., Jaffé, Y. L., et al. 2018b, MNRAS, 480, 3152
Vulcani, B., Poggianti, B. M., Tonnesen, S., et al. 2020, ApJ, 899, 98
Wang, J., Catinella, B., Saintonge, A., et al. 2020a, ApJ, 890, 63
Wang, J., Koribalski, B. S., Jarrett, T. H., et al. 2017, MNRAS, 472, 3029
Wang, J., Koribalski, B. S., Serra, P., et al. 2016, MNRAS, 460, 2143
Wang, J., Staveley-Smith, L., Westmeier, T., et al. 2021, ApJ, 915, 70
Wang, J., Xu, W., Lee, B., et al. 2020b, ApJ, 903, 103
Wang, S., Wang, J., For, B.-Q., et al. 2022, ApJ, 927, 66
Westmeier, T., Deg, N., Spekkens, K., et al. 2022, PASA, 39, e058
Wetzel, A. R., Tinker, J. L., Conroy, C., & van den Bosch, F. C. 2013, MNRAS, 432, 336
Whitmore, B. C., Gilmore, D. M., & Jones, C. 1993, ApJ, 407, 489
Wong, T., & Blitz, L. 2002, ApJ, 569, 157
Wright, E. L., Eisenhardt, P. R. M., Mainzer, A. K., et al. 2010, AJ, 140, 1868
Wyder, T. K., Martin, D. C., Schiminovich, D., et al. 2007, ApJS, 173, 293
Xie, L., De Lucia, G., Hirschmann, M., & Fontanot, F. 2020, MNRAS, 498, 4327
Yoon, H., Chung, A., Smith, R., & Jaffé, Y. L. 2017, ApJ, 838, 81
York, D. G., Adelman, J., Anderson, J. E. J., et al. 2000, AJ, 120, 1579
Yu, Q., Fang, T., Feng, S., et al. 2022, ApJ, 934, 114
Zhang, H.-X., Hunter, D. A., Elmegreen, B. G., Gao, Y., & Schruba, A. 2012, AJ, 143, 47
Zibetti, S., Charlot, S., & Rix, H.-W. 2009, MNRAS, 400, 1181
Zuo, P., Yang, D., Wang, J., et al. 2022, RAA, 22, 095016